

Search for lepton flavor violating decays of the Higgs boson

A Dissertation

Submitted to the Graduate School
of the University of Notre Dame
in Partial Fulfillment of the Requirements
for the Degree of

Doctor of Philosophy

by

Fanbo Meng,

Colin Jessop, Director

Graduate Program in Physics

Notre Dame, Indiana

September 2018

© Copyright by

Fanbo Meng

2017

All Rights Reserved

Search for lepton flavor violating decays of the Higgs boson

Abstract

by

Fanbo Meng

A search for lepton flavour violation Higgs decay in the $H \rightarrow \mu\tau_h$ and $H \rightarrow e\tau_h$ in which tau leptons decay hadronically is presented. The search of tau lepton hadronic decay channels and the searches that are combined with tau lepton leptonic decays are presented. The $H \rightarrow e\tau_h$ search utilizes the 2012 proton-proton collision dataset at LHC with an integrated luminosity of 19.7 fb^{-1} at a center-of-mass energy of 8 TeV collected by CMS experiment. No significant excess was observed. The upper limits on branching fraction and the corresponding Yukawa coupling were set at 95% CL. For the $H \rightarrow \mu\tau_h$ search, the full 2016 proton-proton collision dataset with an integrated luminosity of 35.9 fb^{-1} at a center-of-mass energy of 13 TeV was used. No significant excess was observed and the upper limits on branching fraction $H \rightarrow \mu\tau$ and the corresponding Yukawa coupling were set.

To my family

CONTENTS

FIGURES	v
TABLES	viii
ACKNOWLEDGMENTS	x
CHAPTER 1: Introduction	1
CHAPTER 2: Theory	4
2.1 Standard model	4
2.1.1 Spontaneous symmetry breaking and Higgs mechanism	7
2.2 Lepton flavour violation in beyond stand model theories	12
2.2.1 Lepton flavour violation Higgs decay in effective field theory	12
2.2.2 LFV in two Higgs models	15
CHAPTER 3: LHC and CMS experiment	18
3.1 LHC accelerator	18
3.2 Compact Muon Solenoid	20
3.2.1 Tracker	23
3.2.2 Electromagnetic calorimeter	25
3.2.3 The hadron calorimeter	26
3.2.4 Muon detector	28
3.2.5 Trigger	29
CHAPTER 4: Datasets	32
4.1 Datasets used in LFV analysis	32
4.1.1 $H \rightarrow \mu\tau_h$	32
4.1.2 $H \rightarrow e\tau_h$	35
4.2 Event reconstruction	35
4.2.1 Particle flow algorithm	37
4.2.1.1 Tracking and Calorimeter algorithm	37

4.2.2	Muon reconstruction and selection criteria	41
4.2.3	Electron identification	43
4.2.4	Tau lepton reconstruction	48
4.2.5	Jet reconstruction	54
4.2.6	Missing transverse momentum	57
4.3	Event simulation	58
CHAPTER 5: LFV event selection		60
5.1	$H \rightarrow \mu\tau_h$	60
5.1.1	Loose selection	60
5.1.2	Cut-based analysis	62
5.1.3	Multivariate analysis	63
5.2	$H \rightarrow e\tau_h$	68
5.2.1	Loose selection	68
5.2.2	Cut-based analysis	70
CHAPTER 6: LFV analysis background estimation		73
6.1	Background estimates for $H \rightarrow \mu\tau_h$	73
6.1.1	Misidentified Leptons	73
6.1.2	Other backgrounds	78
6.2	Background estimates for $H \rightarrow e\tau_h$	79
6.2.1	Misidentified Leptons	79
6.2.2	$Z \rightarrow \tau\tau$	81
6.2.3	Other backgrounds	83
CHAPTER 7: Signal extraction and systematics		84
7.1	Boosted decision trees method	84
7.2	Statistical methods	87
7.3	Systematics	93
7.3.1	Systematics used in $H \rightarrow \mu\tau_h$	93
7.3.2	Systematic uncertainties in $H \rightarrow e\tau_h$	94
CHAPTER 8: LFV Higgs decay search results		101
8.0.1	Results in $H \rightarrow \mu\tau_h$ search	101
8.0.2	Results in $H \rightarrow e\tau_h$ search	107
CHAPTER 9: Conclusion		114
BIBLIOGRAPHY		116

FIGURES

2.1	Standard model particle group[8]	5
2.2	Production models in LHC	10
3.1	A sketch view LHC injection chain and main experiments associated [72].	21
3.2	A sketch view of CMS detector [29]	22
3.3	The structure of tracker in CMS [29]	24
3.4	ECAL geometrical configuration [47]	26
3.5	A longitudinal view of CMS HCAL sub-detector [29]	27
3.6	A overview of muon chamber configuration in CMS [30]	30
4.1	A sketch view of CMS detecter. Examples are given to show how the particles interact with different sub-detectors.	42
4.2	The electron BDT-based ID shows good discriminating power against background in both EB and EE [69]	46
4.3	The PF electron isolation shows better performance in both EB and EE with respect to detector based isolation variable [69]	47
5.1	Expected limits based on an Asimov dataset as a function of $M_T(\tau, MET)$ for the different categories.	64
5.2	Expected limits based on an Asimov dataset as a function of M_{jj} for the 2 jet categories.	66
5.3	Distributions of the input variables to the BDT for the $H \rightarrow \mu\tau_h$ channel.	67
5.4	Expected limits based on an Asimov dataset as a function of $M_T(\tau, MET)$ for the different categories.	68
5.5	Overtraining checking for the BDT training in the TMVA package.	69

5.6	With loose selection conditions, the comparison of the observed collinear mass distributions with background from prediction. The shaded grey bands indicate the total background uncertainty. The open histograms correspond to the expected signal distributions for $\mathcal{B}(H \rightarrow e\tau_h) = 100\%$ in the 0-jet, 1-jet and 2-jet categories, respectively.	71
6.1	f_τ ratio for the τ fake rate calculation shows in term of tau decay modes, p_T , ECAL barrel, ECAL endcap, and $ \eta $	76
6.2	f_τ ratio for the μ fake rate calculation shows in term of muon p_T and $ \eta $	77
6.3	The validation of the fully data driven method for the misidentified lepton background. The uncertainties in the distributions include both statistics and systematics uncertainties.	78
6.4	f_τ and f_τ ratio for the mididentification calculation shows in term of p_T and $ \eta $	82
6.5	Data driven method validation in Region II with e and τ leptons in same sign of charge	83
7.1	Tree structure example in BDT	86
7.2	Test statistics distribution of signal+background and background only PDFs and the observed valued shown in arrow.	90
7.3	Signal strength modifier μ at 95% CL_s distribution from the MC pseudo-data. The right plot is the cumulative distribution of $\mu^{95\%}$ with $\pm 1\sigma$ and $\pm 2\sigma$ bands.	91
8.1	M_{col} distribution after the selection. The signal and backgrounds in the plots have been normalized to the best fit values. The gray bands shows the total uncertainties in each bin and the signal is plotted with the branching ratio of 5% of the Higgs decay branching ratio for visualization purpose.	103
8.2	The BDT discriminator distribution after the selection. The signal and backgrounds in the plots has been normalized to the best fit values. The gray bands shows the total uncertainties in each bin and the signal is plotted with the branching ratio of 5% of the Higgs decay branching ratio for visualization purpose.	104
8.3	The expected and observed 95% CL limits on branching ratio of total $H \rightarrow \mu\tau$ which shows the results from both $H \rightarrow \mu\tau_h$ and $H \rightarrow \mu\tau_e$ in the M_{col} fit analysis and BDT fit analysis.	107

8.4	Upper limit of flavour violating Yukawa coupling $ Y_{\mu\tau} , Y_{\tau\mu} $ from the BDT fit analysis. The red solid line represents the expected limit and the black solid line is the observed limit. 68% and 95% range of containing the observed limit is shown in the green and yellow band. The result from $\tau \rightarrow 3\mu$ is shown in dark green [64, 65, 78] and the one from $\tau \rightarrow \mu\gamma$ is shown in lighter green [64, 78]. The theoretical naturalness limit $Y_{ij}Y_{ji} \leq m_i m_j / v^2$ is shown by purple diagonal line [64].	108
8.5	M_{col} distribution after the selection. The signal and backgrounds in the plots have been normalized to the best fit values. The gray bands shows the total uncertainties in each bin and the signal is plotted with the branching ratio of 0.69% of the Higgs decay branching ratio for visualization purpose.	110
8.6	95% CL upper limit on branching ratio on $H \rightarrow e\tau$ with both the results from $H \rightarrow e\tau_h$ and $H \rightarrow e\tau_\mu$ and the combined.	112
8.7	Upper limit of flavour violating Yukawa coupling $ Y_{e\tau} , Y_{\tau e} $ from the combined $H \rightarrow e\tau$ result. The red solid line represents the expected limit and the black solid line is the observed limit. 68% and 95% range of containing the observed limit is shown in the green and yellow band. The result from $\tau \rightarrow 3e$ is shown in gray, the one from $\tau \rightarrow e\gamma$ is shown in dark green and presented analysis is in light blue. The theoretical naturalness limit $Y_{ij}Y_{ji} \leq m_i m_j / v^2$ is shown by purple diagonal line [64]	113

TABLES

2.1	Mediators in standard model [62]	5
2.2	SM Higgs($m=125$ GeV) production cross sections at $\sqrt{s} = 8$ TeV and 13 TeV. The ttH production is at NLO QCD and NLO electro-weak accuracies while other production models listed here are at NNLO QCD and NLO electro-weak accuracies [1]	12
2.3	Four types of 2HDM models differs by the coupling to Higgs doublet fields	15
4.1	Monte Carlo samples used in the $H \rightarrow \mu\tau_h$ search, together with their respective cross sections.	33
4.2	Continue with MC samples used in the analysis.	34
4.3	Signal and background MC samples	36
4.4	Iterative tracking steps taken in CMS	39
4.5	Muon ID used in the analysis, for the LHC data 2016, running period BCDEF.	43
4.6	Muon ID used in the analysis, for the LHC data 2016, running period G and H, also the monte Carlo samples.	44
4.7	Dominant hadronic τ lepton decays branching fractions and the associated intermediate resonance. The h stands for both π and K. The table is symmetric under charge conjugation.	50
4.8	τ hadronic decay mode hypothesis signatures compatibility tests. The m_τ is required to be in the mass window	52
5.1	Selection criteria in each category with the optimization of the $H \rightarrow \mu\tau_h$ analysis	65
5.2	Selection criteria for each event category after cut optimization, for the $H \rightarrow e\tau_h$ channel	72
6.1	Definition of the samples used to estimate the misidentified lepton background.	74

6.2	Scale factor to the events in which a muon is misidentified as a tau	79
7.1	Part one of the systematic uncertainties considered in $H \rightarrow \mu\tau_h$ analysis. All of the uncertainties listed in the systematic tables are correlated between categories besides the ones after the sign \oplus . These are the uncertainties correlated within each category but independent between categories. The theoretical uncertainties related to the acceptance and migration of events are listed in a range. The negative or positive values indicate anticorrelated or correlated between categories	95
7.2	Part two of the systematic uncertainties considered in $H \rightarrow \mu\tau_h$ analysis	96
7.3	b tagging veto systematic uncertainty in each category	96
7.4	The normalization systematic uncertainties considered in $H \rightarrow e\tau_h$ analysis. The uncertainties are correlated between categories besides the ones after \oplus . These uncertainties are uncorrelated between categories.	98
7.5	The systematic uncertainties that affect the shape of M_{col} distribution.	99
7.6	Theoretical uncertainties that affects the Higgs boson production cross section. These uncertainties are correlated or anticorrelated (with minus sign superscript) between all of the categories.	100
8.1	M_{col} fit analysis expected and observed upper limits at 95% CL and the best fit branching fractions in each of the categories.	105
8.2	BDT fit analysis expected and observed upper limits at 95% CL and the best fit branching fractions in each of the categories.	106
8.3	Events yields of the signal and backgrounds are shown in the mass range $100 \text{ GeV} < M_{col} < 150 \text{ GeV}$. The branching ratio of $H \rightarrow e\tau_h$ is assumed to be 0.69% of the SM Higgs production cross section. The numbers in the table are normalized to the integrated luminosity of 19.7 fb^{-1}	109
8.4	M_{col} fit analysis expected and observed upper limits at 95% CL and the best fit branching fractions in each of the categories of both $H \rightarrow e\tau_h$ and $H \rightarrow e\tau_\mu$ analyses. The asymmetric one standard-deviation uncertainties around the expected limits are shown in parentheses.	111

ACKNOWLEDGMENTS

First I would like to thank my adviser Prof.Colin Jessop for the constant guidance, help and support in the past years in both research and everyday life. Thanks for Colin's advises step by step towards being a qualified researcher and great helps and understanding when I was in difficulties. I would also like to thank the help and accompanies from my friends at Notre Dame and CERN. Thanks for making my life colorful. Thanks for the high energy group providing me the opportunity of working at CERN. The CMS is a great collaboration with the best research environment, researchers and collaborators.

Finally I would like to thank the love and supports from my family.

CHAPTER 1

Introduction

The goal of elementary particle physics is to understand the fundamental particles and the interactions among them. Based in the microscopic world, particle physics attempts to construct theories that try to understand phenomena, make predictions and finally come to a consistent and unified theory.

The Standard Model(SM) provides the modern understanding of particle physics. It incorporates the knowledge from decades of research. Except for gravity, the SM describes interactions among elementary particles that includes three out of four fundamental forces. The last missing piece, predicted by the SM, the Higgs boson was discovered in the Large Hadron Collider by both of the general purpose detectors, the CMS and ATLAS detector in 2012. The Higgs boson is a unique and crucial component of the SM. The Higgs boson is incorporated in the SM through the Higgs mechanism, which provides masses to fermions while keeping the theory renormalizable under local gauge symmetry. If viewing the Higgs mechanism within a bigger picture, the spontaneous symmetry breaking of SU(2) group, it is also related to providing the masses to other gauge bosons that mediate the interactions. The discovery of the Higgs boson is a great achievement both theoretically and experimentally. Further studies about the properties of the newly discovered boson show good agreement with the predictions from the SM. Besides the great success of the SM, there are still a number of questions that

beyond the scope of the SM, for example, failing to include gravity and describing dark matter that shows its signature in the astronomy observations. New physics models are needed to understand these questions beyond the SM.

The newly discovered Higgs boson can be a great probe to the physics beyond the SM, which in turn can test and inspire new physics models. In the SM, each flavour of leptons in the three generations is assigned a unique lepton number that is conserved within each family. The violation of this conservation which is referred as lepton flavour violation(LFV) is forbidden in the SM but allowed in many new physics scenarios. Thus, any observation of LFV will be a clear signature of new physics. The discovery of the Higgs boson can open a new window towards this topic. Before LHC era, direct searches for LFV Higgs decay, for example $H \rightarrow \mu\tau$ instead of the SM process $H \rightarrow \tau\tau$ or $H \rightarrow \mu\mu$, was impossible. The upper limits on $B(H \rightarrow \mu\tau)$ and $B(H \rightarrow e\tau)$ of $O(10\%)$ [20, 63] from the indirect searches like $\tau \rightarrow \mu$ and $\tau \rightarrow e$ [28]. In these indirect searches, the LFV Higgs decays can only occur in the processes involving loop diagrams and the LFV Higgs decays to $\mu\tau$ and $e\tau$ from indirect searches leave plenty of room to further probe this topic. While for $H \rightarrow e\mu$, there is already a strong constrain from $\mu \rightarrow e\gamma$ at $B(H \rightarrow e\mu) < O(10^{-9})$ [18]. The CMS experiment published the first direct search on $H \rightarrow \mu\tau$ with integrated luminosity of 19.7 fb^{-1} at center-of-mass energy of 8 TeV. A 2.4σ excess was observed and the best fit branching ratio was found to be $B(H \rightarrow \mu\tau_h) = (0.84^{+0.39}_{-0.37})\%$ at 95% CL [5]. A following up search from ATLAS experiment showed the upper limits in $H \rightarrow \mu\tau$ channel as $B(H \rightarrow \mu\tau) = (1.24^{+0.50}_{-0.35})\%$ at 95% CL [9].

This dissertation focuses on the first direct search in $H \rightarrow e\tau_h$ with integrated luminosity of 19.7 fb^{-1} at 8 TeV and the search in $H \rightarrow \mu\tau_h$ with integrated

luminosity of $35.9\text{ }fb^{-1}$ at 13 TeV with the CMS detector. The dissertation is organized as following. A brief summary of the SM, specifically the electro-weak sector, the Higgs mechanism and LFV in beyond the SM theories are presented in Chapter 2. Following the theory chapter is the one that describes LHC and CMS experiment in general and sub-detectors in CMS. Chapter 4 includes the information about datasets used in the analyses, which incorporate the data collected from the experiment and Monte Carlo(MC) simulations, also the re-construction procedure of the basic objects used in the analysis, like muon, tau and jet. The selections used in $H \rightarrow \mu\tau_h$ and $H \rightarrow e\tau_h$ analysis are described in Chapter 5. In Chapter 6, a detailed description of the background processes considered in analyses is presented. In chapter 7, the event selection and signal extraction is described. In Chapter 8, the results from $H \rightarrow \mu\tau_h$ and $H \rightarrow e\tau_h$ analysis are summarized and presented. In chapter 9, the results are interpreted in terms of LFV Yukawa couplings.

CHAPTER 2

Theory

2.1 Standard model

The discovery of the Higgs boson in 2012 was the last missing piece in SM. The particles in the SM are shown in Figure. 2.1. Besides the Higgs boson, there are three generations of leptons and quarks and four gauge bosons. Leptons and quarks are fermions that compose the observable matter currently known in the universe, while gauge bosons serve as the mediators of the interactions.

The SM is a gauge theory, which describes three natural forces, the strong, electromagnetic and weak force by symmetry group $SU(3)_C \times SU(2)_L \times U(1)_Y$. The electroweak sector is described by the $SU(2)_L \times U(1)_Y$. The L in the subscript of $SU(2)_L$ stands for the left chiral signature of the weak interaction and the Y in $U(1)_Y$ stands for the weak hypercharge. The strong interaction is described by $SU(3)_C$, in which the C stands for the colors of quarks. Photons, gluons and W^\pm , Z bosons are the mediators of electromagnetic, strong and weak force respectively. The force of gravity is not included in the SM. Each particle in Figure. 2.1 has its anti-particle or the anti-particle is the particle itself. The characters of the forces and mediators are summarized in Table. 2.1

The fermion fields in SM can be further categorized. In weak interaction, left-handed fermions are isodoublets, while right-handed fermions are isosinglets.

Standard Model of Elementary Particles

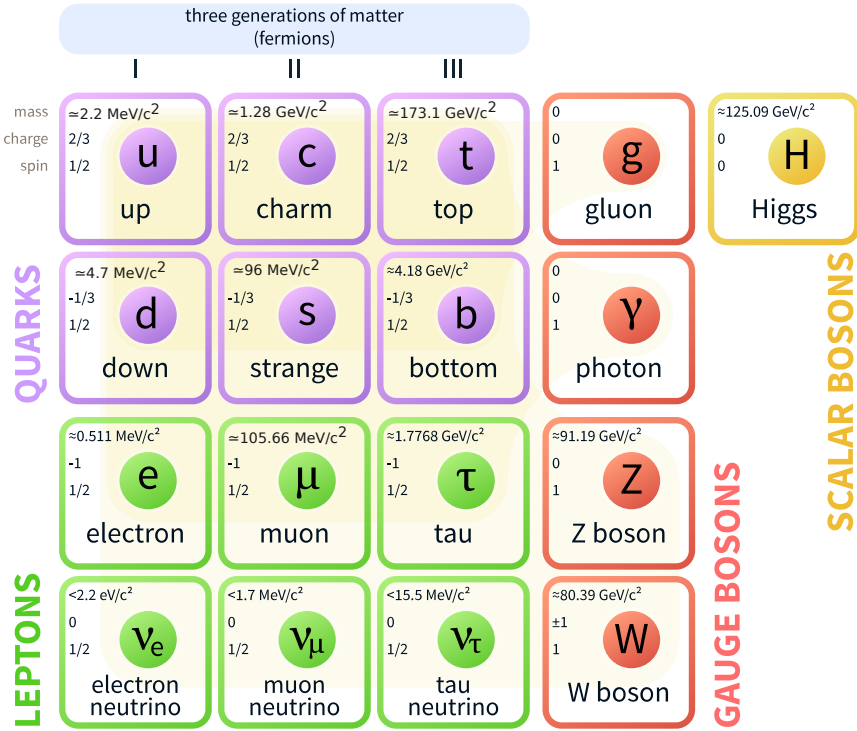


Figure 2.1. Standard model particle group[8]

TABLE 2.1

Mediators in standard model [62]

Force	Mediator	Charge	Mass(GeV)	Range(m)
Strong	g(8 gluons)	0	0	10^{-15}
Electromagnetic	γ (photon)	0	0	∞
Weak	W^\pm	± 1	80.379	10^{-18}
	Z	0	91.1876	10^{-18}

Only left-handed fermions or right-handed anti-fermions participate in the weak interaction. Weak hypercharge is a combined quantity, which is defined by the electric charge Q and the third component of the weak isospin I_f^3 , $Y = Q - I_f^3$. The weak interaction, together with Electromagnetic interaction is best described and understood by the electro-weak theory, which will be further discussed in the next section. Quarks are described by $SU(3)$, which are color triplets, while leptons are color singlets.

The mediators in the interaction are represented by the gauge boson fields. B_μ is associated with symmetry $U(1)_Y$ and the corresponding generator is Y . $W_\mu^{1,2,3}$ are associated to $SU(2)_L$ symmetry with the generators T^a ($a=1,2,3$). The T^a are the 2×2 Pauli matrices, while the $G_\mu^{1,\dots,8}$ are associated with the $SU(3)_c$ symmetry and the corresponding generators are the Gell-Mann matrices. The field strengths are expressed as

$$\begin{aligned} G_{\mu\nu}^a &= \partial_\mu G_v^a - \partial_v G_\mu^a + g_s f^{abc} G_\mu^b G_v^c \\ W_{\mu\nu}^a &= \partial_\mu W_v^a - \partial_v W_\mu^a + g_2 \epsilon^{abc} W_\mu^b W_v^c \\ B_{\mu\nu} &= \partial_\mu B_v - \partial_v B_\mu \end{aligned} \quad (2.1)$$

The g_s and g_2 are the coupling constant of $SU(3)_C$ and $SU(2)_L$ respectively. With the requirement of local gauge invariable, covariant derivatives are widely used. The covariant derivative in the Lagrangian is a substitution of normal derivative. It specifies the interaction between matter and gauge fields while keeps the Lagrangian invariant under local transformation. An example of a covariant derivative acting on left-handed quarks in Lagrangian is expressed as

$$D_\mu \psi = (\partial_\mu - ig_s T_a G_\mu^a - ig_2 T_a W_\mu^a - ig_1 \frac{Y_q}{2} B_\mu) \psi \quad (2.2)$$

The masses of gauge bosons are generated through spontaneous symmetry

breaking by applying the Higgs mechanism, which also enables one to introduce the fermion masses. If boson mass terms are directly added in the SM Lagrangian, the local symmetry $SU(2) \times U(1)$ will be destroyed [55]. Local symmetry here refers to the symmetry that smoothly depends on space and time. In SM, the interaction between fermion field and scalars field is through Yukawa interaction. The Lagrangian of SM in $SU(3)_C \times SU(2)_L \times U(1)_Y$ symmetry without the mass terms and Yukawa interactions is given by

$$L_{SM} = -\frac{1}{4}G_{\mu\nu}^a G_a^{\mu\nu} - \frac{1}{4}W_{\mu\nu}^a W_a^{\mu\nu} - \frac{1}{4}B_{\mu\nu} B^{\mu\nu} + \bar{L}_i iD_\mu \gamma^\mu L_i \\ + \bar{e}_{R_i} iD_\mu \gamma^\mu e_{R_i} + \bar{Q}_i iD_\mu \gamma^\mu Q_i + \bar{\mu}_{R_i} iD_\mu \gamma^\mu \mu_{R_i} + \bar{R}_i iD_\mu \gamma^\mu d_{R_i} \quad (2.3)$$

2.1.1 Spontaneous symmetry breaking and Higgs mechanism

In the SM, the electroweak sector follows the symmetry $SU(2)_L \times U(1)_Y$, which is spontaneously broken in the $SU(2)_L$ part. This mechanism plays an important role in giving masses to the mediator bosons in weak interaction and introducing the Higgs boson(Higgs). The interactions of the scalar doublet with fermion fields through the Yukawa interactions are responsible for generating the masses of the fermions in SM. A good example of showing the concept of spontaneous symmetry breaking is with the ϕ^4 theory which can be found in [79].

In the SM, spontaneous symmetry breaking is introduced through the scalar doublet:

$$\phi = \begin{pmatrix} \phi^+ \\ \phi^0 \end{pmatrix} = \frac{1}{\sqrt{2}} \begin{pmatrix} \phi_2 - i\phi_1 \\ \phi_4 - i\phi_3 \end{pmatrix}$$

The corresponding terms of the scalar doublet in the SM Lagrangian are expressed as

$$L_s = (D^\mu \phi)^\dagger (D_\mu \phi) - \mu^2 \phi^\dagger \phi - \lambda (\phi^\dagger \phi)^2 \quad (2.4)$$

If $\mu^2 < 0$ and $\lambda > 0$, the doublet field ϕ will have a none zero minimum value, which is called the vacuum expectation value(VEV). In SM, the VEV is shown in the following equation and measured to be 246 GeV.

$$\langle 0|\phi|0\rangle = \begin{pmatrix} 0 \\ \frac{v}{\sqrt{2}} \end{pmatrix} \quad \text{with} \quad v = \left(-\frac{\mu^2}{\lambda} \right)^{1/2} \quad (2.5)$$

When the SU(2) symmetry is spontaneously broken, the scalar doublet field ϕ can expand around the VEV at first order together with the Higgs field:

$$\phi = \begin{pmatrix} \theta_2 + i\theta_1 \\ \frac{1}{\sqrt{2}}(v + H) - i\theta_3 \end{pmatrix} = e^{i\theta_a(x)T^a(x)/v} \begin{pmatrix} 0 \\ \frac{1}{\sqrt{2}}(v + H) \end{pmatrix} \quad (2.6)$$

Taking the unitary gauge, the scalar field transforms as $\phi \rightarrow e^{-i\theta_a(x)T^a(x)/v}\phi$ and the term $(D^\mu\phi)^\dagger(D_\mu\phi)$ can be expended as:

$$\begin{aligned} (D^\mu\phi)^\dagger(D_\mu\phi) &= |(\partial_\mu - ig_2 \frac{T_a}{2} W_\mu^a - \frac{i}{2}g_1 B_\mu)\phi|^2 \\ &= \frac{1}{2}(\partial_\mu H)^2 + \frac{1}{8}g_2^2(v + H)^2|W_\mu^1 + iW_\mu^2|^2 \\ &\quad + \frac{1}{8}(v + H)^2|g_2 W_\mu^3 - g_1 B_\mu|^2 \end{aligned} \quad (2.7)$$

W^\pm and Z can be expressed as following by re-grouping the terms in the above equation:

$$W^\pm = \frac{1}{\sqrt{2}}(W_1 \mp iW_2), Z_\mu = \frac{g_2 W_\mu^3 - g_1 B_\mu}{\sqrt{g_2^2 + g_1^2}}, A_\mu = \frac{g_2 W_\mu^3 + g_1 B_\mu}{\sqrt{g_2^2 + g_1^2}}, \quad (2.8)$$

From the terms in Equation 2.7 that involving the mass of W^\pm and Z boson, these

vector bosons acquire the mass as

$$M_W = \frac{1}{2}vg_2 \quad \text{and} \quad M_Z = \frac{1}{2}v\sqrt{g_2^2 + g_1^2} \quad (2.9)$$

while photon A_μ remains massless. The mixing of electromagnetic and weak interaction is often expressed in terms of Weinberg angle or weak mixing angle. The angle θ_W is defined as following:

$$\begin{pmatrix} \gamma \\ Z^0 \end{pmatrix} = \begin{pmatrix} \cos\theta_W & \sin\theta_W \\ -\sin\theta_W & \cos\theta_W \end{pmatrix} \begin{pmatrix} B \\ W_3 \end{pmatrix}$$

$$M_Z = \frac{M_W}{\cos\theta_W} \quad \text{and} \quad \cos\theta_W = \frac{g_2}{\sqrt{g_2^2 + g_1^2}} \quad (2.10)$$

The mass of the fermion can also be generated with the interaction between the scalar doublet ϕ and fermion fields. Taking the muon as an example, the interaction term and the term that gives mass to muon in the Lagrangian is shown as following:

$$L_\mu = -\lambda_\mu(\bar{v}_\mu, \bar{\mu}_L)\phi\mu_R = -\frac{1}{\sqrt{2}}\lambda_\mu(v + H)\bar{\mu}_L\mu_R + \dots \quad (2.11)$$

The mass of muon can be expressed as $M_\mu = \frac{\lambda_\mu v}{\sqrt{2}}$. Other fermions acquire masses in the same way. The coupling of Higgs and fermions can also be derived from Equation. 2.11 [55].

The production modes of the Higgs boson at LHC are the gluon-gluon fusion(ggH), the vector boson fusion(VBF), the associated production with a vector boson(VH) and the production in association with a pair of top quarks($t\bar{t}H$). The Feynman diagrams for these production modes are shown in Figure. 2.2. In LHC,

proton proton collision, the real collisions are among quarks and gluons. ggH holds the biggest Higgs production cross section, while the VBF follows. The other two are relatively small compared with ggH and VBF. VBF and ggH are the signal production modes considered in the analyses that are presented in the later chapters.

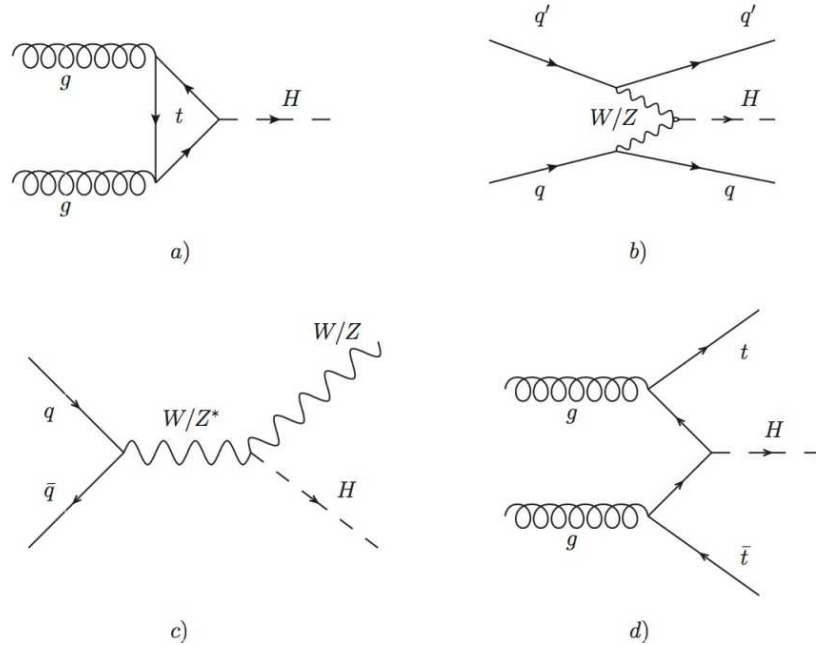


Figure 2.2. Production models in LHC

The cross section of the Higgs boson production modes in LHC have been calculated accurately. Besides the tree level diagrams that are illustrated in the Figure 2.2, high order processes are needed. The inclusive cross sections of the Higgs boson production modes that are used in the 8 TeV and 13 TeV analysis are shown

in Table. 2.2. These cross sections are calculated at NNLO at QCD and NLO electroweak accuracies for all of the production modes, besides ggH at 13 TeV, which is calculated at N3LO QCD and NLO electroweak accuracies. The accuracies here refers to the correction in high order terms, especially the QCD radiative corrections and electroweak correction [53]. The high order correction in ggH and VBF production modes are discussed in the following. In the ggH production mode, the Higgs boson couples to gluons through quark loops and the dominant contributions are from heavy quarks. The corrections in this mode includes vertex corrections, real gluon radiations, initial state rescattering and etc. Dealing with these corrections, the technique like large- m_t limits and full consideration of top and bottom quark mass dependence have been used in the NLO corrections [56]. In the same manner, NNLO correction has been calculated and further improved by resumming the soft-gluon contributions [27]. In 13 TeV, N3LO correction in the ggH inclusive production mode has been computed in the effective theory in which the top-quark is integrated out [48]. The next important correction in the ggH production mode is the electroweak correction with two loop diagrams and the mixed QCD-EW effects have been computed [15]. A most update evaluation of the EW correction can be found in [48]. The uncertainties in the ggH cross section computation has two primary origins, the missing terms in the cross section calculation and the limited knowledge of PDF. In the VBF production mode, the NNLO QCD correction is computed by the structure function approach, which view the process as a double deep-inelastic scattering process and the two vector boson are emitted and merged into Higgs boson [21], while the EW correction is with the Monte Carlo programs [54].

TABLE 2.2

SM Higgs($m=125$ GeV) production cross sections at $\sqrt{s} = 8$ TeV and 13 TeV. The ttH production is at NLO QCD and NLO electro-weak accuracies while other production models listed here are at NNLO QCD and NLO electro-weak accuracies [1]

	ggH(pb)	VBF(pb)	WH(pb)	ZH(pb)	ttH(pb)
8 TeV	1.947E+01	1.601E+00	7.026E-01	4.208E-01	1.330E-01
13 TeV	4.414E+01	3.783E+00	1.373E+00	8.839E-01	5.071E-01

2.2 Lepton flavour violation in beyond stand model theories

Lepton flavour violating Higgs decays are forbidden in SM. The relevant terms of LFV in SM Lagrangian will not be compatible with renormalization under local gauge symmetry. But beyond Standard Model, lepton flavour conservation does not necessarily hold. In the following, two methods that can introduce LFV are presented, the model independent effective field approach and the two Higgs doublet model. In both cases, the focus is how the LFV Higgs decay shows up in the new theories.

2.2.1 Lepton flavour violation Higgs decay in effective field theory

The Effective Lagrangian approach is widely used to explore the new physics with higher dimensional operators in a model independent way. The effective

Lagrangian in the theory can be written as up to dimension six operators:

$$L_{eff} = L_{SM} + \sum_{n,i,j} \frac{a_n^{ij}}{\Lambda^2} O_n^{ij} \quad (2.12)$$

where a_n^{ij} is the coefficients, $i, j, (= 1, 2, 3)$ are flavour indices, n holds the number of the operators and Λ is the new physics scale.

Various effective field operators can introduce processes that violate lepton flavour conservation [52]. As an example, the Yukawa-type operators that generate LFV Higgs decays will be discussed. The Yukawa-type operators hold the following terms:

$$O_{L\phi}^{ij} = (\Phi^\dagger \Phi)(\bar{L}_{L_i} l_{R_j} \Phi) \quad (2.13)$$

While, inside the Lagrangian, the change to SM Lagrangian takes the form:

$$\Delta L_Y = -\frac{\lambda'_{ij}}{\Lambda^2} (\Phi^\dagger \Phi)(\bar{L}_L^i l_R^j \Phi) + h.c... \quad (2.14)$$

Taking in the scalar doublet expansion around the VEV as shown in Equation. 2.6, the $O(6)$ Yukawa-type operators have the following form:

$$\begin{aligned} \Delta L_Y &= -\frac{\lambda'_{ij}}{\Lambda^2} (\Phi^\dagger \Phi)(\bar{L}_L^i l_R^j \Phi) + h.c... \\ &= -\frac{\lambda'_{ij}}{2\sqrt{2}\Lambda^2} l_L^i l_R^j (v + H)^3 + h.c... \\ &= -\frac{\lambda'_{ij} v^3}{2\sqrt{2}\Lambda^2} l_L^i l_R^j - \frac{\lambda'_{ij} 3v^2}{2\sqrt{2}\Lambda^2} l_L^i l_R^j + h.c... \end{aligned} \quad (2.15)$$

The SM Higgs and lepton coupling components in Equation. 2.11 is obtained through the diagonalization of mass matrices [64]. The total Lagrangian in the effective field theory is a combination of SM Lagrangian L_{SM} and the effective

field Lagrangian ΔL_Y . Thus the combined fermion mass and Yukawa interaction terms are following:

$$\sqrt{2}m = V_L \left[\lambda + \frac{v^2}{2\Lambda^2} \lambda' \right] V_R^\dagger, \quad \sqrt{2}Y = V_L \left[\lambda + 3 \frac{v^2}{2\Lambda^2} \lambda' \right] V_R^\dagger \quad (2.16)$$

The Yukawa couplings of Higgs and leptons mixed in the contributions from dimension six operators and have the following form, in which $\hat{\lambda} = V_L \lambda' V_R$

$$Y_{ij} = \frac{m_i}{v} \delta_{ij} + \frac{v^2}{\sqrt{2}\Lambda^2} \hat{\lambda}_{ij} \quad (2.17)$$

In the limit $\Lambda \rightarrow \infty$, the SM results can be recovered, but in general case, like in the electro-weak scale and a arbitrary non-diagonal matrix $\hat{\lambda}$, LFV Higgs decays can be introduced into the theory through effective fields.

In the search of LFV Higgs decays, for example the $H \rightarrow \mu\tau$ channel, the constrains on Yukawa couplings, $|Y_{\mu\tau}|, |Y_{\tau\mu}|$, can be derived from the limits on branching fraction $\mathcal{B}(H \rightarrow \mu\tau)$. In $H \rightarrow \mu\tau$ decays, the Yukawa interactions is related to the decay width $\Gamma(H \rightarrow \ell^\alpha \ell^\beta)$, ℓ^α, ℓ^β can be μ or τ and $\ell^\alpha \neq \ell^\beta$. Γ in terms of the Yukawa couplings is given by:

$$\Gamma(H \rightarrow \ell^\alpha \ell^\beta) = \frac{m_H}{8\pi} (|Y_{\ell^\beta \ell^\alpha}|^2 + |Y_{\ell^\alpha \ell^\beta}|^2), \quad (2.18)$$

and the branching fraction by:

$$\mathcal{B}(H \rightarrow \ell^\alpha \ell^\beta) = \frac{\Gamma(H \rightarrow \ell^\alpha \ell^\beta)}{\Gamma(H \rightarrow \ell^\alpha \ell^\beta) + \Gamma_{\text{SM}}}. \quad (2.19)$$

2.2.2 LFV in two Higgs models

In the model with two Higgs doublets(2HDM) Φ_1 and Φ_2 , similar to the SM, the Yukawa interaction can be written as:

$$L = y_1 \bar{L} \Phi_1 E + y_2 \bar{L} \Phi_2 E + h.c, \quad (2.20)$$

Here, y_1 and y_2 are Yukawa couplings. If there is not a parity symmetry to distinguish the two Higgs doublets, there can be a coupling of the two doublets to the leptons in the tree level. In general it is impossible to diagonalize y_1 and y_2 simultaneously thus the LFV Higgs decay can be presented in the renormalizable Lagrangian [50].

In 2HDM, there are in general four sub-type of models, the main difference comes from the coupling of Higgs doublets to the quarks and leptons as shown in Table. 2.3.

TABLE 2.3

Four types of 2HDM models differs by the coupling to Higgs doublet fields

Model	u_R^i	d_R^i	e_R^i
Type I	Φ_2	Φ_2	Φ_2
Type II	Φ_2	Φ_1	Φ_1
Type III (lepton specific)	Φ_2	Φ_2	Φ_1
Type IV (Flipped)	Φ_2	Φ_1	Φ_2

The type III 2HDM is more relevant to this dissertation which can have the tree level LFV Higgs decay. The Higgs doublets can have the general form:

$$\Phi_j = \begin{pmatrix} \phi_j^+ \\ (v_j + \phi_j + i\eta_j/\sqrt{2}) \end{pmatrix} \quad (2.21)$$

Under the common assumption of CP conservation in the Higgs sector and not spontaneously broken, the quartic odd terms are eliminated in the potential, then the scalar potential can be expressed as

$$V = m_{11}^2 \Phi_1^\dagger \Phi_1 + m_{22}^2 \Phi_2^\dagger \Phi_2 - m_{12}^2 (\Phi_1^\dagger \Phi_2 + \Phi_2^\dagger \Phi_1) + \frac{\lambda_1}{2} (\Phi_1^\dagger \Phi_1)^2 + \frac{\lambda_2}{2} (\Phi_2^\dagger \Phi_2)^2 + \lambda_3 \Phi_1^\dagger \Phi_1 \Phi_2^\dagger \Phi_2 + \lambda_4 \Phi_1^\dagger \Phi_2 \Phi_2^\dagger \Phi_1 + \frac{\lambda_5}{2} [(\Phi_1^\dagger \Phi_2)^2 + (\Phi_2^\dagger \Phi_1)^2] \quad (2.22)$$

The scalar doublets fields Φ_1 and Φ_2 are not physical observables but the mass eigenstates are. So any combination of the scalar doublet fields, as long as it preserves CP and gauge symmetry in SM, produces the same physics results [23].

The following basis is referred to as Higgs basis for the Higgs doublets:

$$H_1 = \begin{pmatrix} G^+ \\ \frac{1}{\sqrt{(2)}}(v + \phi_1^0 + iG^0) \end{pmatrix}, \quad H_2 = \begin{pmatrix} H^+ \\ \frac{1}{\sqrt{(2)}}(\phi_2^0 + iA) \end{pmatrix} \quad (2.23)$$

The relationship between scalar field ϕ_1^0 and ϕ_2^0 and neutral Higgs mass eigenstates h and H is the following:

$$\begin{aligned} h &= \sin(\alpha - \beta)\phi_1^0 + \cos(\alpha - \beta)\phi_2^0 \\ H &= \cos(\alpha - \beta)\phi_1^0 - \sin(\alpha - \beta)\phi_2^0 \end{aligned} \quad (2.24)$$

The angle $\alpha - \beta$ is the mixing angle between these two groups of scalars. The in-

teractions of Higgs and fermions are through Yukawa coupling. In the Higgs base, the Yukawa interaction terms in the Lagrangian of the 2HDM can be expressed as:

$$\begin{aligned} -L_Y = & \sqrt{2} \left(\bar{q}_{L_j} \tilde{H}_1 \frac{K_{ij}^* m_i^U}{v} u_{R_i} + \bar{q}_{L_i} H_1 \frac{m_i^D}{v} d_{R_i} + \bar{l}_{L_i} H_1 \frac{m_i^E}{v} e_{R_i} \right) \\ & + \bar{q}_{L_i} \tilde{H}_2 \rho_{ij}^U u_{R_j} + \bar{q}_{L_i} H_2 \rho_{ij}^D d_{R_j} + \bar{l}_{L_i} H_2 \rho_{ij}^E e_{R_j} + h.c.. \end{aligned} \quad (2.25)$$

Inside the Lagrangian, the terms denote as following, $\tilde{H}_i = i\sigma_2 H^{*i}$, K_{ij} as the CKM matrix and $\rho^{U,D,E}$ are complex matrices in flavor space. Taking in Equation. 2.23 and 2.24, the lepton Yukawa interaction terms are collected as:

$$\begin{aligned} -L_Y = & \bar{e}_i \left(\frac{m_i^E}{v} \delta_{ij} s_{\beta-\alpha} + \frac{1}{\sqrt{2}} \rho_{ij}^E c_{\beta-\alpha} \right) e_j h \\ & + \bar{e}_i \left(\frac{m_i^E}{v} \delta_{ij} c_{\beta-\alpha} - \frac{1}{\sqrt{2}} \rho_{ij}^E S_{\beta-\alpha} \right) e_j H + ... \end{aligned} \quad (2.26)$$

Term $s_{\beta-\alpha}$ and $c_{\beta-\alpha}$ stand for $\sin(\beta-\alpha)$ and $\cos(\beta-\alpha)$ respectively. The coupling of leptons and Higgs in the 2HDM model typeIII are expressed as

$$\begin{aligned} g_{hff'} &= \frac{m_f}{v} s_{\beta-\alpha} \delta_{ff'} + \frac{\rho_{ff'}}{\sqrt{2}} c_{\beta-\alpha} \\ g_{Hff'} &= \frac{m_f}{v} s_{\beta-\alpha} \delta_{ff'} - \frac{\rho_{ff'}}{\sqrt{2}} c_{\beta-\alpha} \end{aligned} \quad (2.27)$$

So this shows the possibility of LFV Higgs decay at tree level [16].

CHAPTER 3

LHC and CMS experiment

The Large Hadron Collider [58] is the most powerful hadron collider ever built. The circumference of this circle superconducting collider is 26.7 km and the designed full operation energy is 14 TeV. In 2012, the LHC operated on 8 TeV and in 2016, it boosted up to 13 TeV. There are four collision locations on the LHC ring which hold four particle detectors, ALICE, ATLAS, CMS and LHCb. The ATLAS and CMS are general purpose detectors, aiming for the high luminosity operation. The LHCb focuses on the b physics study, while ALICE studies the lead-lead collision.

3.1 LHC accelerator

A sketch view of the proton accelerating process is shown in Figure. 3.1. The LHC is the most powerful accelerator in the accelerating chain. Before the beams are injected into LHC, a series of steps are taken. In the proton-proton(p-p) collision, protons are from the source Duoplasmatron, which uses electric field to break down hydrogen gas into protons and electrons, then the protons are accelerated by a 90 kV supply. Leaving the source, the protons are focused and accelerated to 750 keV by the radio frequency quadrupole. Then the protons are further accelerated by the linear accelerator Linac2 to 50 MeV. The proton

synchrotron booster further accelerates the protons from 50 MeV to 1.4 GeV and injects the protons into the proton synchrotron(PS). The PS accelerates the protons to 25 GeV followed by the super proton synchrotron which boosts the protons to 450 GeV. The LHC is the last ring in the whole accelerating process and accelerates the protons to its current final energy 6.5 GeV. In a normal fill of protons in LHC, the ring holds 2808 bunches with an approximation of 10^{11} protons.

There are thousands of superconducting magnets along the LHC ring to bend and focus the beam. Among the magnets, there are 1232 main dipoles which are used to bend the beam with a magnetic field above 8 T. Other types of magnets, for example, the quadrupole magnet can tight the beam either vertically or horizontally, while the sextupole, octupole and decapole can help fine tuning the magnetic field. The radiofrequency cavities(RF) in the LHC are used to accelerate the protons from 450 GeV to 6.5 GeV, keep the bunches in the beam pipe compact and restore the energy loss from synchrotron radiation. Eight RFs per beam, provide 16 MV longitudinal oscillating voltage with the 400 MHz superconducting cavity system.

The machine luminosity is an important parameter of the collider. For a process under study, the number of events created per-second N_{event} is shown in Equation. 3.1, in which L is the machine luminosity and σ_{event} is the cross section of that process.

$$N_{\text{event}} = L\sigma_{\text{event}} \quad (3.1)$$

The machine luminosity is determined by a number of factors as shown in

Equation. 3.2.

$$L = \frac{N_b^2 n_b f_{rev} \gamma_\gamma}{4\pi\epsilon\beta*} F \quad (3.2)$$

The n_b and N_b are the number of bunches per-beam and the number of protons per-bunch respectively. The f_{rev} and γ_γ are the revolution frequency and relativistic gamma factor respectively. The $\beta*$ is the amplitude function of the beam at the collision point while the function F describes the reduction of luminosity because of the crossing angle. This machine luminosity is also called instantaneous luminosity which is the luminosity at a unit time. The integrated luminosity which later is referred as luminosity is the instantaneous luminosity that integrates over time.

3.2 Compact Muon Solenoid

The compact muon solenoid(CMS) is a general purpose detector. It is a high performance detector that is designed to observe any new physics produced by LHC. It covers a broad range of physic studies like the standard model physics and the search for supersymmetry and dark matter candidates. The CMS detector is designed to have good muon momentum and position resolution over a large range of energy and angles, good charged particle momentum resolution and high identification efficiency within inner tracker, good electromagnetic energy and position resolution, high photon and lepton isolation efficiency in the high luminosity condition and good missing transverse momentum and jet energy resolution.

A general view of the CMS detector is shown in Figure. 3.2. The detector is composed of a set of sub-detectors from the inside and out in a ring structure. The main sub-detectors are the followings:

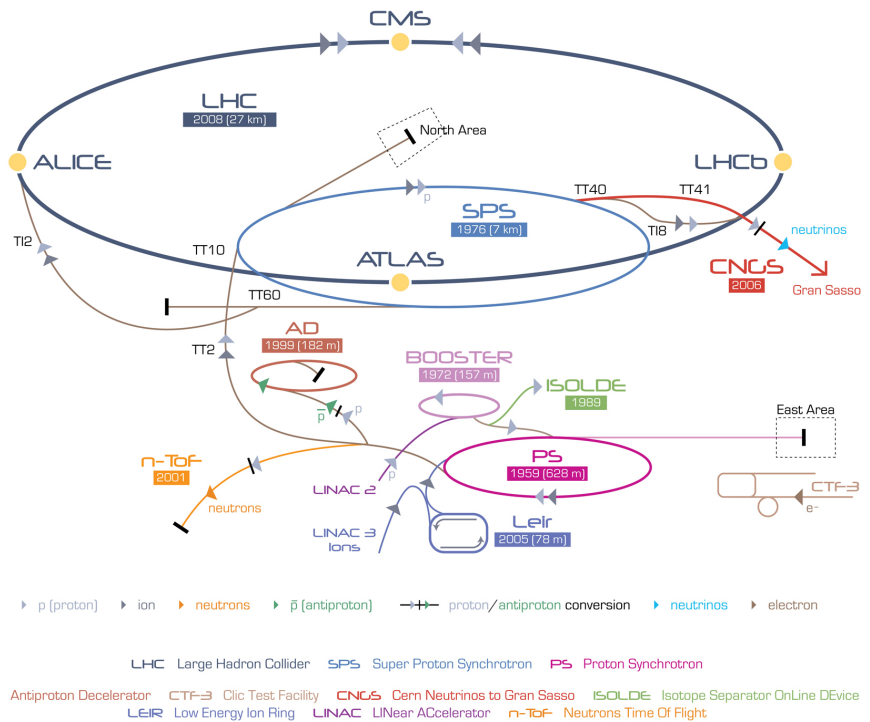


Figure 3.1. A sketch view LHC injection chain and main experiments associated [72].

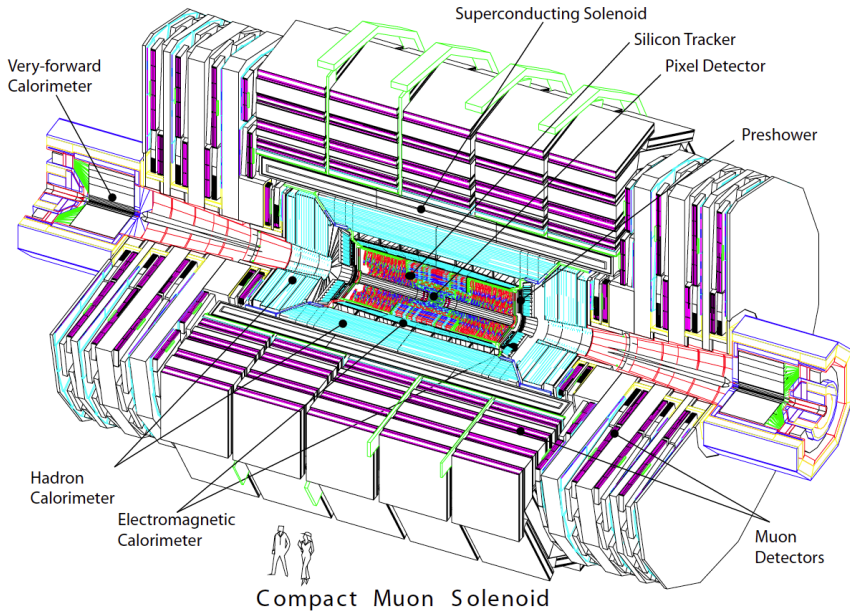


Figure 3.2. A sketch view of CMS detector [29]

- The inner tracker consists of two parts, the pixel detector and silicon strip tracker which are used measure the momentum and tracks of the charged particles.
- The electromagnetic calorimeter mainly measures the energy and the position of electrons and photons. Other particles will leave some percentage of energy inside while passing through.
- The hadron calorimeter measures the energy of hadrons.
- The muon detector measures the tracks and momentum of the muons.

Another outstanding feature of CMS is the superconducting magnet system, which provides a 3.8 T magnetic field. The configuration of the magnet system drives the design and layout of the detector. Besides the sub-detectors listed

above, the trigger system is also crucial for the success of the whole program. The trigger system consists of two parts, the hardware based level-1 trigger and the software based high level trigger. The trigger system does the initial selection of events from a huge flux of events per-collision, which makes it possible for data-acquisition and recording. The details of the sub-detectors and other systems mentioned will be further discussed later.

In general, the CMS detector is 21.6 m long, 14.6 m in diameter and weighs 12500 tonnes in total. The coordinate system adopted by CMS sets the center at the collision point. The x-axis points towards the center of LHC ring and the z-axis points along the beam direction. The azimuthal angle ϕ measures from the x-axis in the x-y plane, polar angle θ measures from the zenith direction and the r is the radial coordinate. Another variable called the pseudorapidity η , defined as $\eta = -\ln[\tan(\theta/2)]$ is also frequently used in the measurement. In the case, a particle with $E \gg m$, pseudorapidity can be approximated as $\eta = -\ln\left(\frac{E+p_z}{E-p_z}\right)$, where the p_z is the longitudinal component of momentum [29].

3.2.1 Tracker

The inner tracking system of CMS is designed to measure the trajectories of charged particles. The efficient and precise measurement is crucial for the reconstruction and identification of particles. The LHC operates with the instantaneous luminosity in the order of $10^{34} cm^{-2}s^{-1}$, in average producing more than 20 p-p interactions and 1000 particles per-bunch crossing collision. High granularity and fast response are the primary features of the tracker system. To measure the trajectories precisely, low interactions of tracker materials with incoming particles, like multi-scattering, photon conversion and nuclear interaction are also important.

tant. In the long operation period, radiation hardness of the tracker material is needed. All of these factors drive the design of CMS tracker system.

The tracker system of CMS surrounds the collision point and has the dimension of 5.8 m in length and 2.5 m in diameter, with a coverage up to pseudorapidity $|\eta| < 2.5$. An overview of the tracker system layout is shown in Figure. 3.3. Three layers of silicon pixel detector modules surround the interaction point and two additional disks of pixel modules on each side, in all 66 million pixels of the size $100 \times 150 \mu\text{m}$ each. Following the pixel detector is the silicon strip tracker. There are four components of the strip tracker, tracker inner barrel(TIB), tracker inner discs(TID), tracker outer barrel(TOB) and tracker end caps(TEC). The arrangement of the strip tracker components is shown in Figure. 3.3 which consist of 10 layers and about 10 million strips.

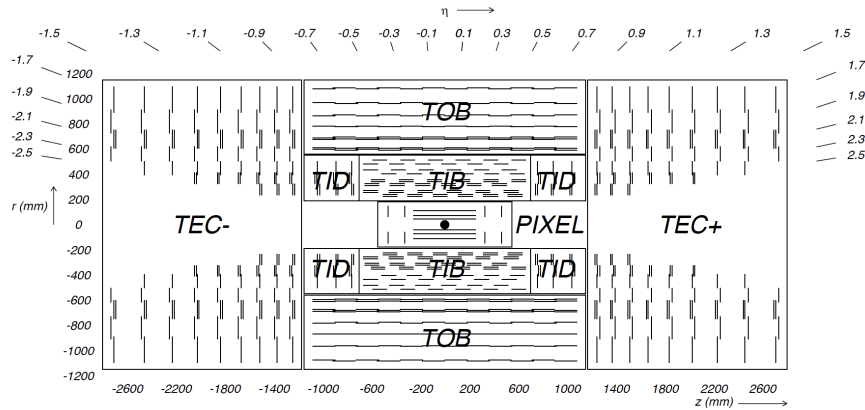


Figure 3.3. The structure of tracker in CMS [29]

3.2.2 Electromagnetic calorimeter

The electromagnetic calorimeter(ECAL) in CMS is a hermetic homogeneous lead tungstate(PbWO_4) detector. The whole sub-detector is composed of two parts, the central barrel(EB) covering the pseudorapidity range $|\eta| < 1.479$ and the endcap disks(EE) covering the range $1.479 < |\eta| < 3.0$. The EB is made up of 61200 PbWO_4 crystals with $22 \times 22 \text{ mm}^2$ in the front face, 23 cm in length(25.8 in radiation lengths). The EE is made up of 7324 crystals per disk with front face $29 \times 29 \text{ mm}^2$ and 22 in length(24.7 in radiation lengths). The geometrical configuration of ECAL is shown in Figure. 3.4.

The PbWO_4 crystals used in ECAL have high density(8.28 g/cm^3), short radiation length(0.89 cm) and small Molière radius(2.2 cm), together with the specific geometrical parameters used, rendering ECAL good energy resolution, fast response, fine granularity and high radiation resistant. Photodetectors are placed at the end of the crystals. In EB, avalanche photodiodes(APDs) are used, while vacuum phototriodes(VPTs) are used in EE. Both types of the photodiode show good performance in the environment with hard radiation and 4 T magnetic field. The preshower detector(ES) [47] is in front of the EE in the pseudorapidity range $1.653 < |\eta| < 2.6$. The ES is a sampling detector with silicon strip sensors placed behind the lead radiator to measure the energy and position of the incoming particles.

Each half of the EB is composed of 18 supermodules that each supermodule contains 1700 crystals. The relative energy resolution of PbWO_4 crystal refers to the resolution that is measured with ECAL supermdules directly exposed to electron beam. The relative energy resolution as a function of electron energy can

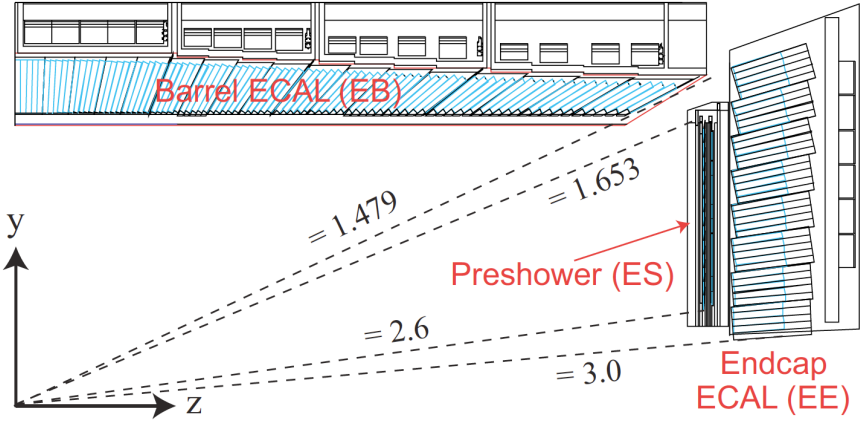


Figure 3.4. ECAL geometrical configuration [47]

be expressed as

$$\frac{\sigma}{E} = \frac{2.8\%}{\sqrt{E/\text{GeV}}} \oplus \frac{12\%}{E/\text{GeV}} \oplus 0.3\%$$

The first term stands for the contribution from stochastic factors, like the number fluctuation in production of the secondary particles. The second term is the noise contribution coming from the electronics and digitization, while the last is a constant term that covers the other contribution factors [13].

3.2.3 The hadron calorimeter

The CMS hadron calorimeter(HCAL) is a hermetic sampling detector, which is important for the measurement of the energy and momentum of hadrons, also the missing energy that caused by the non-interacting particles. The HCAL is composed of three parts, the HCAL barrel(HB), HCAL endcaps(HE) and forward calorimeter(HF). The mechanical structure of HCAL is shown in Figure. 3.5.

The HB is composed of several layer of brass absorber plates, between which

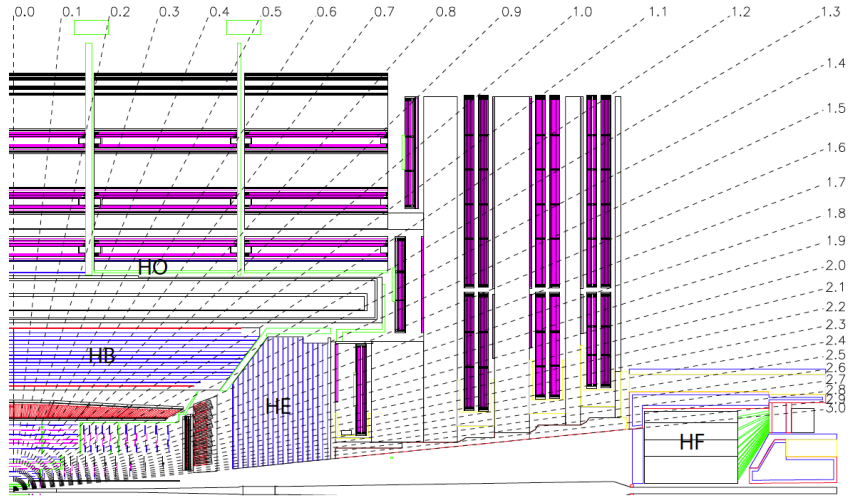


Figure 3.5. A longitudinal view of CMS HCAL sub-detector [29]

are the plastic scintillator tiles. The innermost and outermost layer plates are made of stainless steel to gain structural strength. When hadrons hit the absorber, secondary particles are produced in showers. As the showers develop, the alternating layers of scintillators are activated and emit blue-violet light. The lights are collected as signals. The HB covers the central pseudorapidity range $|\eta| < 1.3$ with an individual read out unit $\Delta\eta \times \Delta\phi = 0.087 \times 0.087$. Because of the limited spaces between ECAL and muon detector, to have enough sampling depth in HCAL central region, an extra outer calorimeter(HO) is installed. The HO utilizes the outside solenoid coil as additional absorber to insert plastic scintillators. Similar to HB, the HE is also made of brass absorber and plastic scintillator tiles layers, which covers the range $1.3 < |\eta| < 3.0$. The read out units have the geometry $\Delta\eta \times \Delta\phi = 0.17 \times 0.17$ in the HE [29]. A combined ECAL and HCAL energy resolution [86] measured in test beam with pions is

$$\frac{\sigma}{E} = \frac{110\%}{\sqrt{E/\text{GeV}}} \oplus 0.9\%$$

The HF situates ± 11 m from the interaction point to complement the large pseudorapidity measurement of HE in the range $3.0 < |\eta| < 5.0$. The HF is made of grooved steel plates with quartz fibers. Charged shower particles generate Cherenkov light, which is collected by the quartz fibers as signals. Radiation hardness is critical for the operation of HF.

3.2.4 Muon detector

The CMS muon detector is designed to measure the momentum and charge of muon. Three types of gas detectors are used in CMS, the barrel drift tube(DT) chambers, the cathode strip chambers(CSC) in the endcaps and the resistive plate chambers(RPC) in both barrel and endcap regions.

In the muon detector barrel(MB), DT chambers and RPCs are used which cover the pseudorapidity region $|\eta| < 1.2$. The MB is composed of 250 chambers. The chambers are located in 4 stations inside the magnet return yoke. The yoke is further divided into 5 wheels, each of which is composed of 12 sectors. As shown in Figure. 3.6, the stations are named from MB1 to MB4, which are composed of one DT chamber and varied number of RPCs that depending on the exact location. DT chambers measure the position of the incoming muons which knock off the electrons in the gas atoms of the chambers and are collected by a large numbers of charged wires inside.

In muon detector endcaps(ME), 468 CSCs which covers the range $0.9 < |\eta| < 2.4$ are used. The MEs are also composed of 4 stations of chambers in each of the

discs. The CSCs are in a wedge shape and composed of 6 gas gaps. Each gap is filled with a cathodes strip and anode wires which run perpendicularly to the strip. The incoming muons knock off the electrons and create avalanches which are received by the positive charged wires.

Both DT chambers and CSCs measure the position and trigger on the p_T of muons. To better deal with the high luminosity and improve the p_T resolution of the triggered muon, a dedicated trigger system, the RPCs are added to both MB and ME. The RPCs are double-gap bakelite chambers which operate with the avalanches that are caused by the muons. The RPCs can provide additional fast triggering and sharp p_T triggering thresholds. Four RPCs layers are used in the MB first two stations(two each) and another two layers(one each) are used in the last two stations. In the ME, one RPC layer in each of the first three stations.

3.2.5 Trigger

The LHC is a high luminosity collider in the order of $10^{34} \text{cm}^2\text{s}^{-1}$. In the p-p collision, the bunch crossing time is 25 ns and the corresponding frequency is 40 MHz. In each of the 25 ns, there are approximately 20 collisions. This high rate makes it impossible to transmit and record all of the events, also it is not necessary, since most of the events are not of current physics research interests. The CMS uses a two level trigger system to select events and reduces the event recording rate, the Level-1(L1) trigger and High-level trigger(HLT) system.

The L1 trigger system is based on custom designed and programmable electronics which are situated inside the detector. It utilizes the information from calorimeters and muon system, performing simplified but effective reconstructions, corrections and selections. The L1 reduces the incoming event rate from 40 MHz

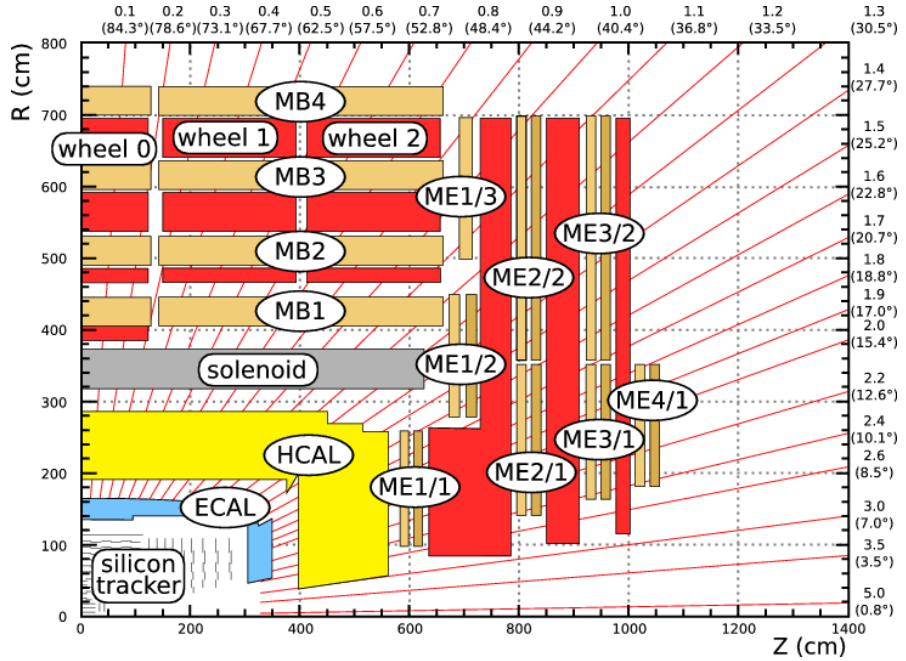


Figure 3.6. A overview of muon chamber configuration in CMS [30]

to 100 kHz. In LHC Run II, the L1 trigger system has been upgraded to deal with the increasing luminosity and improves the performance. The L1 calorimeter trigger accesses the information from the whole ECAL and HCAL in the granularity of trigger tower level, which approximately corresponds to a region 0.087×0.087 in η and ϕ . The L1 trigger reconstructs the e/γ , jets, τ and the sum energy of the candidates with the algorithms implemented in the time multiplexed trigger architecture [17]. The algorithms are implemented at hardware trigger level, with dynamic clustering of trigger towers, pile-up migration and innovated tau and jet reconstruction with various look-up tables for the calibrations and corrections [88]. The L1 muon trigger system fully utilizes three muon detectors in the track reconstruction. In general, based on the geometry, the track reconstruction of muons are divided into three regions, the barrel, the overlap and the endcap. Through

dedicated construction algorithms, tracks are built and various muon qualities are calculated. These informations are used in the triggering processes [81].

The HLT system in CMS further reduces the event rate from 100 kHz(after L1 trigger selection) down to 1 kHz. The HLT is software based trigger system and utilizes the streamlined version of the CMS soft-ware for the event reconstruction on large computer farm [10]. Maximizing the trigger efficiency and keeping acceptable CPU-time is crucial for the HLT system. The HLT accesses to the full granularity and sub-detectors of CMS, including the tracker system. The dedicated algorithms used in the HLT is the very closed to the ones used in the off-line reconstruction, besides some of the parameter configurations [61].

CHAPTER 4

Datasets

4.1 Datasets used in LFV analysis

4.1.1 $H \rightarrow \mu\tau_h$

The dataset analyzed in the $H \rightarrow \mu\tau_h$ decay channel is collected by CMS detector during LHC 2016 operation. The total integrated luminosity of the analyzed dataset is 35.9 fb^{-1} at a center-of-mass energy of $\sqrt{s} = 13 \text{ TeV}$. The dataset in which each event has at least one muon is used. It is selected by the trigger system. The ggH [60] and VBF [26] production are the main Higgs production channels considered in the analysis. For the background samples, besides the misidentified background which is discussed more in detail in Chapter 6, the other background samples are all generated with the Monte Carlo(MC) simulation. The POWHEG [77] and MadGraph [14] generator are used for the generation and all of the MC samples, including the signal samples, the parton showering, fragmentation, and decays are performed by Pythia8 [85]. The pileup effect is taking into account by generating minimum bias events. The average number of pileup interaction per bunch crossing is 27 in 2016. The CMS detector environment is simulated by GEANT4 [45]. The details of the MC samples used in the analysis are summarized in Table. 4.1 and Table. 4.2.

TABLE 4.1

Monte Carlo samples used in the $H \rightarrow \mu\tau_h$ search, together with their respective cross sections.

Processes	Generator	Cross section [pb]
DYJets $\rightarrow \ell\ell$, $m_{\ell\ell} > 50$ GeV	MadGraph+pythia8	4954.0
DY1Jets $\rightarrow \ell\ell$, $m_{\ell\ell} > 50$ GeV	MadGraph+pythia8	1012.5
DY2Jets $\rightarrow \ell\ell$, $m_{\ell\ell} > 50$ GeV	MadGraph+pythia8	332.8
DY3Jets $\rightarrow \ell\ell$, $m_{\ell\ell} > 50$ GeV	MadGraph+pythia8	101.8
DY4Jets $\rightarrow \ell\ell$, $m_{\ell\ell} > 50$ GeV	MadGraph+pythia8	54.8
DYJets $\rightarrow \ell\ell$, $m_{\ell\ell} < 50$ GeV	MadGraph+pythia8	1861.0
$t\bar{t}$	powheg+PYTHIA	831.76
$t\backslash\bar{t} \rightarrow tw$	powheg+PYTHIA8	35.85
$WZ \rightarrow \ell 3v$	MadGraph+PYTHIA8	3.05
$WZ \rightarrow \ell v 2q$	MadGraph+PYTHIA8	10.71
$WZ \rightarrow 2\ell 2q$	MadGraph+PYTHIA8	5.595
$t \rightarrow 4f$	POWHEG+PYTHIA8	136.02
$\bar{t} \rightarrow 4f$	POWHEG+PYTHIA8	80.95
$WW \rightarrow \ell v 2q$	MadGraph+PYTHIA8	1.212
$ZZ \rightarrow 2\ell 2q$	MadGraph+PYTHIA8	3.22
$VV \rightarrow 2\ell 2q$	MadGraph+PYTHIA8	11.95

TABLE 4.2

Continue with MC samples used in the analysis.

MC simulations	Generator	Cross section [pb]
$VV \rightarrow 2\ell 2q$	MadGraph+PYTHIA8	11.95
$ggH \rightarrow \tau\tau$	POWHEG+PYTHIA8	3.046
$VBFH \rightarrow \tau\tau$	POWHEG+PYTHIA8	0.237
$ggH \rightarrow WW \rightarrow 2\ell 2v$	POWHEG+PYTHIA8	1.103
$VBFH \rightarrow WW \rightarrow 2\ell 2v$	POWHEG+PYTHIA8	0.086
$ZH \rightarrow \tau\tau$	POWHEG+PYTHIA8	0.055
$W^- \backslash W^+ H \rightarrow \tau\tau$	POWHEG+PYTHIA8	0.086
$t\bar{t}H Jet \rightarrow \tau\tau$	MadGraph+PYTHIA8	0.32

4.1.2 $H \rightarrow e\tau_h$

The search for lepton flavour violation Higgs decay $H \rightarrow e\tau_h$ is performed with CMS 2012 RunI dataset at a center-of-mass energy $\sqrt{s} = 8$ TeV with an integrated luminosity of 19.7 fb^{-1} . In each of the events in the dataset, at least one electron is required, which is selected by the single electron trigger. More details about the this trigger is discussed in details in the Chapter 5. A detail list of simulation samples used in the analysis is in Table. 4.3. For the signal samples, the ggH and VBF Higgs production channels are the channels considered. For the background samples, besides the $Z \rightarrow \tau\tau$ which is produced with the embedding technique and the misidentified background which is estimated with the data-driven method are produced with Monte Carlo simulation. Various simulation packages are used. Signal samples are produced with PYTHIA8, which uses sophisticated τ -lepton decay machinery. The Tauola [76] package is also used for the simulation of τ lepton decay in some of samples. The CMS detector environment is simulated by GEANT4.

4.2 Event reconstruction

In this section, a general presentation of the event reconstruction algorithm used in CMS, the particle-flow(PF) reconstruction is shown. The focus is the particles and objects that are directly related the physics searches in the dissertation. More detail information of the reconstruction of tracks and the objects used in the physics analyses in CMS can be found in [82].

TABLE 4.3
Signal and background MC samples

Processes	Generator	Cross section [pb]
$ggH \rightarrow e\tau$	PYTHIA8	19.27
$VBH \rightarrow e\tau$	PYTHIA8	1.58
$ggH \rightarrow \tau\tau$	POWHEG+PYTHIA6	19.27
$VBF \rightarrow \tau\tau$	POWHEG+PYTHIA6	1.58
$t\bar{t} + \text{jets full leptonic}$	MadGraph+Tauola	26.20
$t\bar{t} + \text{jets Semi leptonic}$	MadGraph+Tauola	109.28
$t \rightarrow tw$	POWHEG+Tauola	56.4
$\bar{t} \rightarrow tw$	POWHEG+Tauola	30.7
$t, \bar{t}(\text{T channel})$	POWHEG+Tauola	11.1 (11.1)
$WW \rightarrow 2l2\nu + \text{jets}$	PYTHIA6+Tauola	5.824
$ZZ \rightarrow 4l$	MadGraph+Tauola	0.18
$ZZ \rightarrow 2l2Q$	MadGraph+Tauola	2.502
$ZZ \rightarrow 2l2\nu$	MadGraph+Tauola	0.716
$WZ \rightarrow 2l2Q$	MadGraph+Tauola	2.21
$WZ \rightarrow 3l\nu$	MadGraph+Tauola	1.06

4.2.1 Particle flow algorithm

The particle flow event reconstruction algorithm is the main algorithm used in CMS. The PF performs a global event reconstruction, which aims to utilize the information from the whole detector to identify individual particles in each of the events.

4.2.1.1 Tracking and Calorimeter algorithm

In the PF algorithm, the reconstruction of charged particles in the inner tracker is crucial. In this section, the reconstruction of the trajectories of charged particles, especially the electron and muon reconstruction are discussed.

The inner tracker aims at measuring the tracks of energetic charged particles. The track finder is based on the Kalman Filtering(KF) algorithm [12] which performs the reconstruction in several steps. First an initial seed is generated from a couple hits that compatible with a track in the tracker, then a trajectory is builded with the seed and other hits inside the tracker along this track. At last a fit is perform on the track to determine the properties of this particle candidate, like the momentum and the electric charge. Several qualities can affect the performance of the reconstruction, for example, the number of hits in the pixel detector, the total number of hits in the tracker, the distance from the cylinder and the energy of this charged particle.

The performance of the track reconstruction is measured in reconstruction efficiency and misreconstruction rate. The reconstruction efficiency is defined as the ratio between the tracks reconstructed with more than 50% of the simulated hits from the MC sample and the total simulated tracks. The misreconstruction rate is defined as the fraction of the tracks that can not be associated with simulated

tracks within the MC sample. If a charged hadron is not identified by the tracking algorithm, then the hadron is take as a neutral hadron and measured by the calorimeters. This will affect the jet energy and position resolution. Improving the track reconstruction efficiency while keeping the misreconstructed rate low is critical for the PF reconstruction.

In CMS, an iterative tracking is performed, in which the reconstruction of tracks is done in a couple of steps. Each step aims for a moderate efficiency but with a high purity. After one step, the hits that are used to form tracks are masked and a next step is performed. This iterative tracking is done in ten steps if necessary and the detailed information is shown in Table. 4.4 and more can be found in [82]. In the table, the name column points out the processes that this iteration step aims at. The seeding column shows the requirement on the seeding, while the targeted track column shows the characters of the tracks.

Electrons are one of the main particles under study in $H \rightarrow e\tau_h$ search. In CMS, the reconstruction of electron track is taken as a merge of the ECAL based and tracker based strategy. The tracker based seeding strategy is as described above, then a preselection based on the number of hits and χ^2 of the fit is set with the Gaussian-sum filter [11]. The ECAL based electron seeding strategy builds the superclusters(SC) to gather the bremsstrahlung photons. The energy of the SC is taken as the energy sum of the cell crystals inside and the position is evaluated with the weight that is related to the energy distribution. The electron trajectory in the first layer of the tracker is estimated and the seed from the track is selected. This works in the case when there is not much bremsstrahlung photons and most of the energy is deposited in ECAL. In the case when soft photons are radiated mostly, the ECAL based seeding performs better. But when the electrons are in

TABLE 4.4
Iterative tracking steps taken in CMS

Iteration	Name	Seeding	Targeted Tracks
1	InitialStep	pixel triplets	prompt, high p_t
2	DetachedTriplet	pixel triplets	from b hadron decays, $R \lesssim 5$ cm
3	LowPtTriplet	pixel triplets	prompt, low p_t
4	PixelPair	pixel pairs	recover high p_t
5	MixedTriplet	pixel+strip triplets	displaced, $R \lesssim 7$ cm
6	PixelLess	strip triplets / pairs	very displaced, $R \lesssim 25$ cm
7	TobTec	strip triplets / pairs	very displaced, $R \lesssim 60$ cm
8	JetCoreRegional	pixel+strip pairs	inside high p_t jets
9	MuonSeededInOut	muon-tagged tracks	muons
10	MuonSeededOutIn	muon detectors	muons

the jets or of low energy, either electron contributions are overlapping with other particles or the radiation and the bending is too much, it is hard to recover these electrons with ECAL based algorithm only. The ECAL based and tracker based electron seeding is merged into one collection, which significantly improves the reconstruction efficiency.

Calorimeters are crucial components for the PF algorithm in CMS. The clustering algorithms in the calorimeters are used to identify neutral stable particles like photon and neutral hadron. Together with the tracker, calorimeters are used

in the identification of charged particles, reconstructing the energy of electrons and the possible associated bremsstrahlung photons and measuring the energy of charge particles that are missed by the tracker.

The clustering algorithm is perform separately in each sub-detector system besides the HF in which each cell directly raise a cluster. The algorithm starts by finding a cluster seed. Then a topological walk around the neighbouring cells is performed. Both seed cells and neighbouring cells are required to pass certain thresholds to construct high quality candidates and suppress the contribution from the noise. In ECAL endcaps, there are additional requirements on E_T because of the high noise level. In each of the topological clusters, the energy for the neighbouring cells are assumed from the same particle candidate. A Gaussian-mixture model is used in the construction of the topological clusters to evaluate the contribution of each cells. The finally parameters of the model are obtained by analytical fitting to the Gaussian model.

To accurately measure the energy of the particles like photons and neutral hadrons, the calibration of calorimeters is indispensable. The calibration of calorimeters also affects the identification efficiency and the misidentification rate of the particles measured by the calorimeters. The calibration of ECAL is done with a couple sources, like the test beam, the radioactive source and the cosmic ray measurements and is refined with the collision data. There are thresholds used in the formation of topological clusters, which makes the energy measured smaller than the incoming particle energy. A residual energy calibration is applied to all of the ECAL clusters to account for these affects. The correction is applied as a function of cluster energy and position, $f(E, \eta) = g(E)h(\eta)$. In the endcaps, the energy of the measured particle is taken as a liner combination of the ECAL and

preshower energy. The parameters in the combination are optimized by the χ^2 method. Hadrons generally leave energy in both ECAL and HCAL. The calibration of ECAL mentioned above is for the photon and electron calibration. The behavior of hadron is different and a consequent calibration involving both ECAL and HCAL is needed. Simulated single neutral hadrons are used. The relationship involves both the energy measured by ECAL and HCAL and the calibrated energy E_{calib} is expressed as

$$E_{calib} = a + b(E)f(\eta)E_{ECAL} + c(E)g(\eta)E_{HCAL}$$

In the equation above, the coefficient "a" is independent of E and accounts for the effects of thresholds in the clustering algorithm. The other coefficients are determined by the χ^2 optimization with the E_{calib} and true energy E from simulation.

4.2.2 Muon reconstruction and selection criteria

The PF muon is used in the $H \rightarrow \mu\tau_h$ analysis. In CMS, the event reconstruction starts from building the tracks in tracker(tracker track) and muon system(standalone-muon track) separately. The global muon reconstruction and tracker muon reconstruction are based on these tracks [34]. The global muon reconstruction starts from the standalone-muon tracks and requires at least two muon stations in the muon system. For each of the standalone-muon track, a propagation is done to find the matching tracker track on the common surface. The Kalman-filter technique [59] is used in the fitting to combine the hits in standalone-muon track and tracker track. The tracker muon starts from the

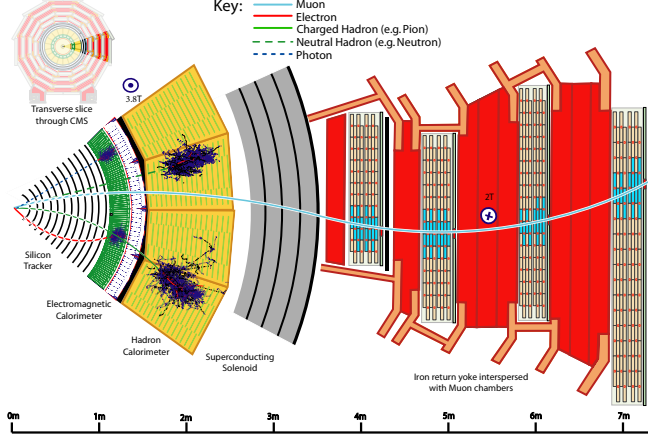


Figure 4.1. A sketch view of CMS detector. Examples are given to show how the particles interact with different sub-detectors.

tracks with $p_T > 0.5$ GeV and total momentum $p > 2.5$ GeV. The tracks are then extrapolated to match the tracks in the muon system with at least one muon segment. Within the geometry acceptance of muon system, the muon reconstruction efficiency is high, especially high momentum muons, constructed as either global muon or tracker muon or both have the efficiency about 99%. The muon PF algorithm applies a series of selections to the global muon and tracker muon to select out the PF muon. The selection is optimized to identify the muons in the jets with high efficiency and low misidentify rate. The details of the selection is in [2].

Taking the PF muon as the input, muons used in the analysis are further categorized into different identification(ID), isolation(Iso) categories. The loose muon ID refers to the muons selected by the PF algorithm. The medium Muon ID is suggested to use in CMS Run II data analysis. For the LHC 2016 running era, two muon medium IDs, with slight differences are applied according to different

TABLE 4.5

Muon ID used in the analysis, for the LHC data 2016, running period BCDEF.

ICHEP mediumID description	Technical description
Loose muon ID	PFLoose Muon
Fraction of valid tracker hits	> 0.49
	Global muon
	Normalized global-track $\chi^2 < 3$
1. Good Global muon	Tracker-Standalone position match < 12
	kick finder < 20
	Segment compatibility > 0.303
2. Tight segment compatibility	Segment compatibility > 0.451

data taking period within 2016, the ICHEP medium muon ID(Table 4.5) to the running period G and H and the Monte Carlo samples, while the standard medium muon ID(Table 4.6) to the remaining datasets. The muon isolation used in the analysis is calculated the same way as the electron isolation which is shown in the following electron section.

4.2.3 Electron identification

Electrons in CMS is constructed with the information from tracker and calorimeters. One of the main difficulties in the reconstruction is the bremsstrahlung en-

TABLE 4.6

Muon ID used in the analysis, for the LHC data 2016, running period G
and H, also the monte Carlo samples.

Standard mediumID description	Technical description
Loose muon ID	PFLoose Muon
Fraction of valid tracker hits	> 0.8
	Global muon
	Normalized global-track $\chi^2 < 3$
1. Good Global muon	Tracker-Standalone position match < 12
	kick finder < 20
	Segment compatibility > 0.303
2. Tight segment compatibility	Segment compatibility > 0.451

ergy emitted by the electron. The conversion of photons from the bremsstrahlung affects the reconstruction of tracks in the tracker and these photons also cause significance energy loose in the electron reconstruction. The reconstruction of electrons is covered in section 4.2.1.1, which discusses the general tracker and calorimeters reconstruction. More details can be found in [69].

The electron ID is constructed to separate prompt isolated electron(signal) from the electrons presented in the background processes. The background can be the electrons from photon conversion, from quark semi-leptonic decay or from misidentification of other particles or jets. The variables used in the identification are related to tracker and ECAL. There are mainly three types of variables. One type is the variables related only to calorimeters, for example, the cluster shape of real electron in ECAL is usually narrower than the shape from hardonic shower and electrons leave most of the energy in ECAL and the energy ratio between ECAL and HCAL is large. The variables related to the matching of measured energy and geometry between tracker and ECAL. The variables related to tracker fitting to explore the differences between electrons and hadrons. These related variables can be used to construct cut-based selection sequence to selection electron. To achieve better performance, the MVA based ID with boosted decision tree is also used. Comparing with the cut-based selection, more variables in the three categories mentioned above are used in the MVA training [69]. An example of the BDT electron ID is shown in Figure 4.2. The discussion of the BDT method is presented in Chapter 7.

The electron isolation is used to reject background events in addition to the ID variables, also inverting the requirement on the isolation can be used to setup enriched background control regions. A large numbers of background events that

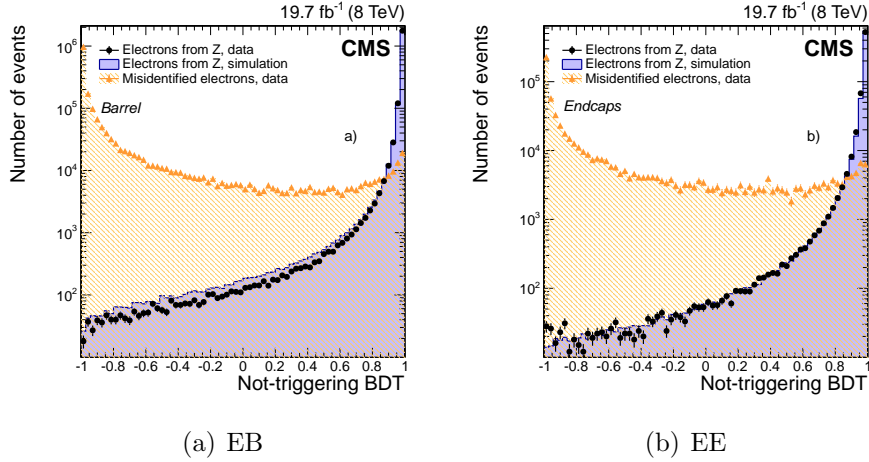


Figure 4.2. The electron BDT-based ID shows good discriminating power against background in both EB and EE [69]

possibly pass the signal selection are misidentified jets or the jets in which there are real electrons, for example the jets from b quark semi-leptonic decay. For these background events, one key different character with respect to signal events is more energy flowing around the electron(or misidentified electron) trajectories. The isolation requirement used in HLT level is summing over the energy depositions either in ECAL or HCAL in a certain core, for example $\Delta R = 0.3, 0.4$, $\Delta R = \sqrt{\Delta\phi^2 + \Delta\eta^2}$. The contribution from the particle candidate is removed. In the offline algorithm, particles can better identified with the PF algorithm. The PF isolation summing over the p_T of the particles in the direction of the reconstructed candidate trajectory momentum. The PF algorithm utilizes the whole detector information and the isolation is calculated as

$$\text{Iso}_{\text{PF}} = \sum p_T^{\text{charged}} + \max \left[0, \sum p_T^{\text{neutral had}} + \sum p_T^\gamma - \frac{1}{2} \sum p_T^{\text{charged,PU}} \right] \quad (4.1)$$

The isolation variable sums over the contribution from charged PF candidates, neutral particles and photons in the selected certain ΔR region around the signal candidate. The contribution from pileup is estimated with the $\Delta\beta$ correction in the last term of Equation. 4.1. The factor 0.5 comes from the naive measurement of neutral to charged particles in jets [25]. The energy of PF objects are better calibrated and the possibly double counting is taken cared of. The PF isolation variable performs better than the isolation variable used in HLT. The performance comparison is shown in Figure. 4.3

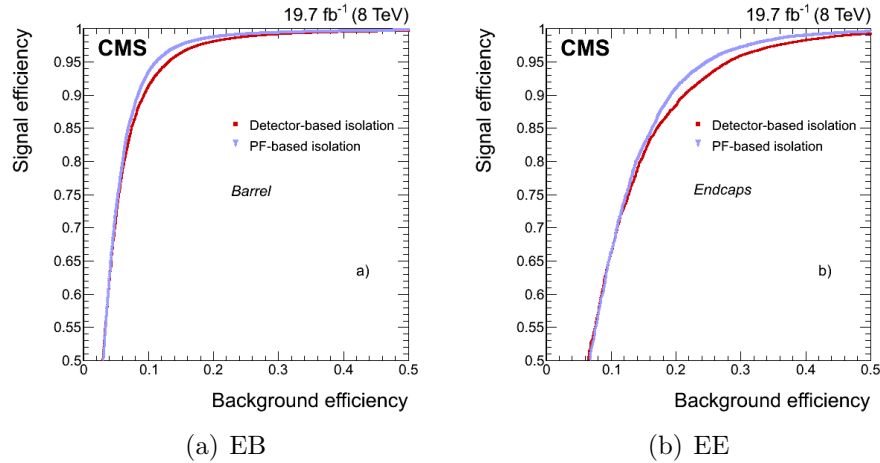


Figure 4.3. The PF electron isolation shows better performance in both EB and EE with respect to detector based isolation variable [69]

4.2.4 Tau lepton reconstruction

In CMS Run I period, tau leptons are constructed with hadrons plus strips(HPS) algorithm. In general, the HPS starts with PF jets which are reconstructed with $Anti - k_T$ algorithm [24], as the initial seeds. The π_0 components from the τ hadronic decays are first constructed and combined with the charge hadrons parts, to identify different τ decay modes and calculate τ four-momentum and other quantities [38]. The τ decay modes is discussed in the later part of this section.

Photon conversions and the bremsstrahlung of electron/positron when travel inside the CMS detector are well treated by the HPS algorithm. These phenomena broaden the signature of the tau decay. Taking PF jets as input, the algorithm constructs strips out of electromagnetic particles and starts by taking the strip(0.05 in η and 0.2 in ϕ) in which contains the most energetic electromagnetic particle as the center one. Within this strip window, if other charged particles are found, they are associated with this strip. The position of the strip is taken and four momentum of the strip is calculated. This procedure is repeated, until no strips can be constructed. The selected strips are required to have $P_T^{strip} > 1$ GeV. The following decay topologies are taking into account by the HPS:

- one charged particle without any strip, h^\pm and the case when π^0 is not energetic enough to form a strip
- one charged particle plus one strip
- one charged particle plus two strips
- three charged partibles.

All of the charged hadrons and strips are required to be contained in the $\Delta R = 2.8/P_T^{\tau_h}$ core, where the $P_T^{\tau_h}$ is the reconstructed τ_h transverse momentum and ΔR is defined as $\Delta R = \sqrt{(\Delta\phi^2 + \Delta\eta^2)}$. The τ_h candidate is also required to match the direction of the seed PF jet within $\Delta R = 0.1$. Assuming all of the charged hadrons to be pions and taking in the associated strips, the HPS algorithm requires that different decay topologies meet the intermediate meson mass requirements as listed in Table. 4.7.

The cut based τ_h isolation discriminant requires that the PF charged particles and photons to be considered in the isolation variable have $p_T > 0.5$ GeV and within the isolation cone $\Delta R = 0.5$ in τ_h direction. The particles that constitute τ_h are excluded from the summation. The effect of charged particles from the pileup is eliminated by considering the charged particle oriented from the τ_h production vertex with in $D_z = 0.2$ cm and $\Delta r = 0.03$ cm. The effect of pileup on the isolation of the photons on the strips is estimated by summing the charged particles that are not oriented from τ_h decay primary vertex, within $\Delta R = 0.8$ in the direction of τ_h and have the impact parameter $D_z > 0.2$ cm. Then a factor $\Delta\beta$ is multiplied to the p_T sum. The isolation variable is calculated as in Equation. 4.2.

$$I_\tau = \sum p_T^{\text{charged}}(d_z < 0.2 \text{ cm}) + \max(0, \sum p_T^\gamma - \Delta\beta \sum p_T^{\text{charged}}(d_z > 0.2 \text{ cm})) \quad (4.2)$$

The tight, medium and loose working points(WP) are the tau isolation discriminants. The exact energy selection in the isolation discriminants is suggested by the study of QCD dijet events, by requiring the I_τ in Equation. 4.2 to have different values. The loose cut brings in approximate 1% of fake τ from jets [38].

TABLE 4.7

Dominant hadronic τ lepton decays branching fractions and the associated intermediate resonance. The h stands for both π and K. The table is symmetric under charge conjugation.

Decay mode	Resonance	Mass (MeV/c^2)	Branching fraction(%)
$\tau^- \rightarrow h^- v_\tau$			11.6%
$\tau^- \rightarrow h^- \pi^0 v_\tau$	ρ^-	770	26.0%
$\tau^- \rightarrow h^- \pi^0 \pi^0 v_\tau$	α_1^-	1200	9.5%
$\tau^- \rightarrow h^- h^+ h^- v_\tau$	α_1^-	1200	9.8%
$\tau^- \rightarrow h^- h^+ h^- \pi^0 v_\tau$			4.8%

In CMS Run II, the tau reconstruction algorithm HPS has been improved [40]. The major improvement lies in dynamic strip instead of fix size strip. Tau decay products can also affect the isolation. The charged pions in tau decay products experience nuclear interaction with tracker materials, which can result in low P_T secondary particles. The photons from the neutral pion decays can also go through pair production into $e^+ e^-$, which further spread because of the bremsstrahlung and the magnetic field. Broadening the strip is need in these cases in order to better cover the tau decay production. On the other hand, if the tau is boosted, high P_T decay products tend to be more concentrated and the smaller strip size is better. Similar to RunI tau reconstruction, the algorithm starts with highest p_T charged particle as seeds for the strip. Starting from the seed strip, a window

in η and ϕ direction is set.

$$\begin{aligned}\delta\eta &= f(P_T^\gamma) + f(P_T^{strip}) & f(P_T) &= 0.2 \cdot P_T^{-0.66} \\ \delta\phi &= g(P_T^\gamma) + g(P_T^{strip}) & g(P_T) &= 0.35 \cdot P_T^{-0.71}\end{aligned}$$

The window is determined from single τ gun MC simulation. 95% of the decay products will be covered in that range. The upward and downward limit for η is 0.15 and 0.05. In the ϕ direction, the range is 0.3 and 0.05. The position of strip is set as p_T weighted average against all of the objects.

$$\begin{aligned}\eta_{strip} &= \frac{1}{P_T^{strip}} \cdot \sum P_T^\gamma \cdot \eta_\gamma \\ \phi_{strip} &= \frac{1}{P_T^{strip}} \cdot \sum P_T^\gamma \cdot \phi_\gamma\end{aligned}$$

The construction of the strips continues until no seed strip can be constructed. After the construction of the τ lepton, for different decay mode, the m_τ is required to lie in different mass windows [41]. The conditions of different hadronic decay mode mass windows are listed in the Table. 4.8. Comparing to RunI conditions, the difference in the mass window is δm , which originates from dynamic clustering. The δm is calculated as:

$$\delta m = \sqrt{\left(\frac{\partial m_\tau}{\partial \eta_{\text{strip}}} \cdot f(p_T^{\text{strip}})\right)^2 + \left(\frac{\partial m_\tau}{\partial \phi_{\text{strip}}} \cdot g(p_T^{\text{strip}})\right)^2}$$

with:

$$\begin{aligned}\frac{\partial m_\tau}{\partial \eta_{\text{strip}}} &= \frac{P_z^{\text{strip}} \cdot E_\tau - E_{\text{strip}} \cdot P_z^\tau}{m_\tau} \\ \frac{\partial m_\tau}{\partial \phi_{\text{strip}}} &= \frac{-(P_y^\tau - P_y^{\text{strip}}) \cdot P_x^{\text{strip}} + (P_x^\tau - P_x^{\text{strip}}) \cdot P_y^{\text{strip}}}{m_\tau}\end{aligned}$$

TABLE 4.8

τ hadronic decay mode hypothesis signatures compatibility tests. The m_τ is required to be in the mass window

Decay mode	Mass window
$\tau^- \rightarrow h^- \pi^0 v_\tau$	$0.3 - \delta m_\tau < m_\tau < 1.3 \cdot \sqrt{p_T/100} + \delta m_\tau$
$\tau^- \rightarrow h^- \pi^0 \pi^0 v_\tau$	$0.4 - \delta m_\tau < m_\tau < 1.2 \cdot \sqrt{p_T/100} + \delta m_\tau$
$\tau^- \rightarrow h^- h^+ h^- v_\tau$	$0.8 - \delta m_\tau < m_\tau < 1.5 + \delta m_\tau$

In current algorithm, $\tau^- \rightarrow h^- h^+ h^- v_\tau$ is not included because of the jet con-

tamination. This hadronic τ decay mode composed of 4.8% of total branching fraction. The $h^-\pi^0$ and $h^-\pi^0\pi^0$ are analyzed together, which is referred as $h^-\pi^0$.

In the analysis with 2016 datasets, the multivariate(MVA) regression technique based τ isolation variable is used, which keeps high identification efficiency while maintains relatively low fake rate compared with cut based discriminator. A Boosted Decision Tree(BDT) has been used in the training of the isolation variable. In the BDT method, the isolation variable shows a good distinguishing power against jets. Various variables have been used as BDT inputs. The variables are isolation variable(I_τ), impact parameters from the highest p_T track of τ_h candidate, τ_h decay mode information, shape variables like ΔR , $\Delta\eta$, τ lifetime information and photon electron multiplicity. More details about the exact variables that are used are discussed in [40, 41]. The BDT method uses these variables to distinguishing τ_h dacay from jets, which can be the decay products from quarks or gluons.

The BDT method is also used in the tau discriminating again electron training. The algorithm utilizes the variables that are sensitive to the energy deposit in ECAL and HCAL, the electron bremsstrahlung, overall particle multiplicity and the difference in electromagnetic and hadronic showers. A detail list of these variables can be find in [40, 41].

Tau leptons from signal events can be misidentified by muons, especially in τ_h decay mode h^\pm . The tau against muon discriminant is set by checking if there are signals in the muon system within $\Delta R = 0.3$ of the τ_h direction or if the energy sum from ECAL and HCAL is less than 20% of the total τ energy. If less than two hits are found in the muon system, then it passes the loose working point. If no hits are found in the muon system, then this is the tight working point.

4.2.5 Jet reconstruction

Jets are produced in the hadronic processes involving quarks or gluons. In the p-p collision, jet involves in most of the processes. Constructing jet properly is crucial and difficult.

The Anti- k_t jet clustering algorithm is used in CMS for the jet reconstruction. The algorithm starts by introducing the distance parameters d_{ij} and d_{iB} as following,

$$d_{ij} = \min(k_{ti}^{2p}, k_{tj}^{2p}) \frac{\Delta_{ij}^2}{R^2}$$

$$d_{iB} = k_{ti}^{2p}$$

The d_{ij} is the distance between the particle and the pseudojet. The Δ_{ij} is the difference of rapidity and azimuth between entry i and entry j, $\Delta_{ij}^2 = (\eta_i - \eta_j)^2 + (\phi_i - \phi_j)^2$. The R is a radius parameter. The k_{ti} and k_{tj} stand for the momentum of the entries respectively. The p is a parameter used to specify jet construction algorithms. For Anti- k_t , the parameter p is set as p=-1. The d_{iB} is the distance between entry i and the beam. If the parameter p is set for other values, for example p=1 or 0, then the algorithm is the k_t [57] or Cambridge/Aachen jet reconstruction algorithm [87]. In the Anti- k_t algorithm, assuming in one event, there are a couple of hard particles with high momentum, k_{t1} , k_{t2} and so on, also large numbers of soft ones around. Starting from k_{t1} as an example, if d_{1j} is smaller, then entry j combined with entry 1, if d_{1B} is smaller, then entry 1 is set as a jet and removed from the list. The soft entries tend to cluster around the high momentum entries in the range $\Delta_{ij} = R$, if there is no other hard entry around.

If two hard entries are within the distance R , then the two entries are clustered into a single entry. In this case, if $k_1 \gg k_2$, then the center is more closed to jet 1. If $k_1 \sim k_2$, the boundary between two jets is defined by $\Delta R_{1b}/k_{t1} = \Delta_{2b}/k_{t2}$. The jet clustering continues until all of the jets are clustered in the events.

The jet energy is corrected to have the correct energy scale. The correction goes through a couple of steps [71]. The major corrections are derived from simulated samples and the residual corrections for the different responses between MC and data samples are from data-driven methods.

Pileup events can increase the measured jet energy, especially in LHC Run II, the number of pileup per event doubled. Two types of pileup affect the performance the most, the in-time pileup(IT PU) and the out-of time pileup(OOT PU). The IT PU refers to the additional events produced by the proton-proton collision within the same bunch-crossing besides the primary hard collisions. The OOT PU refers to the events that produced in previous bunch crossing or subsequent ones that affect current bunch. The OOT PU can be mitigated by exploring the timing window and the pulse shape of the calorimeter. Charged hadrons from IT PU in CMS are removed with charged-hadron subtraction(CHS) algorithm in CMS. Tracks with the vertexes that are identified from PU with charged particles are removed. The CHS removes around 50% of the IT PU within the tracker coverage region. There are also soft jets from pileup interaction. These jets are usually in low energy range and affect the JES by overlapping with the hard jets. The multivariate analysis(MVA) with inputs from jet shape and jet constitution information can remove more than 90% of pileup jets. This MVA ID is referred as PUJetID [4]. After rejecting the charged particle jets and soft jets from pileup, a jet area method [25] is used to further eliminate the effects from PU. In this

method, an estimated energy density brought in by the PU and the effective area of jet are used to calculate the offset energy. After the PU correction, simulated response corrections are performed with QCD multijet sample. A matching between particle-level jet and reconstructed jet is performed. The correction is performed with the anti- k_T jets with the distance parameter R=0.5 in p_T and η distribution and checked with jets corresponding to R in range 0.3 to 1.0. Following the simulated response corrections, the remaining residual corrections are small which are derived with data-based methods and applied to data samples.

The B jet is a main component in $t\bar{t}$ process. The identification of b jet is important to the analysis involves $t\bar{t}$. In CMS, a combined secondary vertex method(CSV) is used in the identification of b jet. The CSV method utilizes multivariable techniques to identify b jet [84]. B jets are from the hadronization of b quarks. B hadrons are relatively heavy, around 5-6 GeV, with high decay multiplicity, relatively high momentum decay products and relatively wide decay core compared with hadrons from light quarks. B hadrons have long lifetime($ct \approx 450$ um) which give a traveling distance ≈ 5 mm at the energy of 70 GeV. Exploring the property of the secondary vertex is used in the identification algorithm. In each of the jets, at least two tracks presenting in an angular distance $\Delta R < 0.3$ is required. The jet with a combined mass of two tracks compatible with k_s^0 is rejected to reduce the contamination. A number of variables are used as MVA inputs in the identification. Details can be referred in [84]. The MVA method combines the input variables into one discriminant variable to identify b jet.

4.2.6 Missing transverse momentum

The missing transverse momentum(MET) is defined as the sum p_T of undetected process in an event. In CMS, the particle flow MET is widely used and the MET can be expressed as $\vec{E}_T = -\sum \vec{p}_T$, in which the sum is over the observed PF particles. The magnitude of MET can be affected by various resources, for example, the inefficiency of tracker, the thresholds on calorimeter and the asymmetry in detector response. The propagation of JEC to MET can reduce the bias. The corrected MET can be expressed as

$$\vec{E}_T^{corr} = \vec{E}_T - \sum_{jets} (\vec{p}_{T,jet}^{corr} - \vec{p}_{T,jet})$$

The sum is over the jets with electromagnetic fraction below 0.9 and corrected $p_T > 10$ GeV. Further correction on effect of PU on MET is derived with charged particles associated with PU vertexes, $\vec{v} = \sum_{charged} \vec{p}_T$. The correction is $f(\vec{v})\vec{v}$, in which factor $f(\vec{v}) = c_1(1.0 + \text{erf}(-c_2|\vec{v}|^{c_3}))$. The coefficients in $f(\vec{v})$ are estimated from fitting the MC minimum bias events. The PU effect corrected MET can be expressed as

$$\vec{E}_T^{corr} = \vec{E}_T - \sum_{PU} f(\vec{v})\vec{v}$$

The observed \vec{E}_T asymmetry in ϕ shows approximately linear relationship with the number of reconstructed vertices. The correction is performed with N_{vtx} separately in x and y axis.

The collinear-mass(M_{col}) is the most important variable in LFV Higgs decay analysis, which is closely related to the MET. The Higgs boson is massive com-

pared with the leptons(e, μ, τ), thus the decay products are boosted. In $H \rightarrow \mu\tau_h$ and $H \rightarrow e\tau_h$ analysis, τ decays hadronically. The neutrinos in τ decay products are highly Lorentz boosted and are considered collinear with τ . The direction of τ and the projection of MET amplitude on $\vec{\tau}$ direction are used to approximate the direction and energy of the neutrinos. With this approximation and the visible mass which is the mass formed with $e-\tau$ or $\mu-\tau$ without any approximation, the M_{col} can be derived as

$$M_{col} = M_{vis} / \sqrt{x_\tau^{vis}}$$

$$x_\tau^{vis} = p_T^{\vec{\tau}^{vis}} / (p_T^{\vec{\tau}^{vis}} + p_T^{\nu,est})$$

4.3 Event simulation

The Monte Carlo simulation is used widely from the detector related processes, event reconstruction to physics analysis. The generation of MC sample in the generator involves the following steps.

In LHC, p-p collision, QCD processes can involve large momentum transferring, multiply final states and complex surrounding environment. MC generators start by calculating the related QCD cross section. This including the calculating the matrix-element, choosing parton distribution functions(PDFs) and possibly performing high order correction, followed by the parton showers. In a hard process, parton showers use the basic building blocks like $q \rightarrow qg$, $q \rightarrow gq$, $g \rightarrow gg$ and $g \rightarrow q\bar{q}$, iteratively showering from high energy to low energy, typically, for quarks and gluons in the order of 1 GeV, when they can not be treated as free particles anymore. In addition to the hard subprocesses and the associated parton

showers, a real event consists more contributions. Typically more than one pair of partons interact in one collision. These multiple interactions are dealt with different models and affect the total scattering energy, the number of the particles in the hadronization stage, etc. Because of the color confinement, quarks and gluons form hadrons after completing the parton shower, this is referred as hadronization. Similarly to the QCD processes, electromagnetic radiation is also taken into account the evolution according to the electric charge instead of the color. After the generation of events through the MC generators, the events are put into GEANT4 [45] to complete the detector simulation.

CHAPTER 5

LFV event selection

In both 8 TeV $H \rightarrow e\tau_h$ and 13 TeV $H \rightarrow \mu\tau_h$ analyses, events are selected in several steps. A loose selection selects on the different IDs, energy, geometry parameters of the analysis related objects. In the M_{col} fit analysis this is followed by a tighter set of selection criteria in which selection requirements are placed on the kinematics variables and fits on variable M_{col} in both $H \rightarrow e\tau_h$ and $H \rightarrow \mu\tau_h$ analysis. This selection sequence is referred as M_{col} fit analysis. In $H \rightarrow \mu\tau_h$, there is an alternate selection sequence that follows the loose selection. A multivariate analysis with a Boosted decision tree (BDT) is defined and fits on the BDT discriminator. This is referred as the BDT fit analysis and provides more sensitive results in $H \rightarrow \mu\tau_h$ analysis.

5.1 $H \rightarrow \mu\tau_h$

5.1.1 Loose selection

Tau leptons from signal events decay hadronically. A SM Higgs boson is much heavier than its decay products μ and τ . The μ and τ leptons are expected to have high P_T . As the decay products from signal events are boosted, therefore a cut on $\Delta R = \sqrt{(\Delta phi)^2 + (\Delta eta)^2}$, $\Delta R > 0.3$ is applied. The μ and τ candidates are required to have opposite sign of charge as the Higgs boson is neutral. Further,

events with additional μ and τ that pass the loose selection and events with jets that are identified by the combined secondary vertex b-tagging algorithm [42] as a b quark jets are vetoed. The high level trigger used in the analysis selects isolated muons that have energy higher than 24 GeV at HLT level. A further P_T cut on the reconstructed μ , $P_T > 26$ GeV and $|\eta| < 2.4$ are required. Muons are required to pass the recommended Medium muon ID and tight cut based isolation $I_{rel}^\mu < 0.15$, which refers to the PF muon isolation variable and is computed as shown in Equation. 4.1.

Hadronic taus are required to have $P_T > 30$ GeV, $|\eta| < 2.3$, passing old tau decay mode finding, the MVA based tight tau isolation ID and tau discriminators against electrons and muons.

Events in the analysis are divided into four categories based on the number of jets. In 2-jets category, it is furthered divided into 2 categories, 2-jet gluon gluon fusion higgs production(ggH) category and 2-jet vector boson fusion(VBF) category based on the value of 2 jets invariant mass(M_{jj}). The ggH and VBF Higgs production models are considered in the analysis. This choice of categorization enhanced one of the production models in each of the categories and improves the sensitivity. The 0-jet category enhances ggH production mode. In 1-jet category, the dominant signal production mode is also ggH, but with a boosted jet associated with the production and VBF higgs production also contributes this category. In the 2-jet ggH category, signal events mainly come from ggH, while in 2-jet VBF, VBF higgs is the dominant production channel. The following is a more detailed list of the selection condition in each categories.

0-jet: No events have jets pass the loose PF ID and with jet $P_T > 30$ GeV, $|\eta| < 4.7$.

1-jet: Events with one jet passes losse PF ID and jet $P_T > 30$ GeV, $|\eta| < 4.7$.

2-jets ggH: Events have two jets passing loose PF ID, $P_T > 30$ GeV, $|\eta| < 4.7$ and a requirement on the invariant mass of the two jets, $M_{jj} < 550$ GeV.

2 jets VBF: Events with two jets pass loose PF ID. Jets $P_T > 30$ GeV, $|\eta| < 4.7$ and $M_{jj} > 550$ GeV are required.

The threshold on M_{jj} has been optimized to give the best expected exclusion limits.

5.1.2 Cut-based analysis

After the loose selection and the categorization, a further cut-based selection is applied. Variables that can help distinguish signal from background are P_T^μ , P_T^τ and $M_T(\tau_h)$. The lepton P_T variables are very powerful background discriminant variables, but will also cause the problem that signal peaks under backgrounds. As leptons from signal process tend to have higher P_T values, cutting tighter on the lepton P_T , removes more background events. However this will also reshape some of the backgrounds, making them peak closer under the signal so that signal processes will be affected more by the background statistics fluctuation. In the $H \rightarrow e\tau_h$ analysis, the effect of cutting tighter on lepton P_T will be shown. In $H \rightarrow \mu\tau_h$ search, lepton P_T variables are kept at loose values and optimized on other variables to achieve tighter expected limits.

The optimization procedure uses only Monte Carlo samples so as not to double use data. In $H \rightarrow \mu\tau_h$ channel, the variables tuned are M_{jj} and $M_T(\tau_h)$. The selection criteria has been optimized to have the most stringent expected limits with the Asimov dataset(background only). The name Asimov dataset is inspired by the short story Franchise, by Isaac Asimov. If looser values of the cuts give the same expected limits as the tighter ones, then the looser cut values are

chosen to have more statistics. Examples of optimization by checking the limits are shown in Figure. 5.1 and 5.2, in which the optimization of $M_T(\tau_h)$ and M_{jj} are shown. A full summary of the cuts optimized for $H \rightarrow \mu\tau_h$ is shown in Table. 5.1

5.1.3 Multivariate analysis

A boosted decision trees(BDT) method is used as the multivariate analysis method in the $H \rightarrow \mu\tau_h$ search which is more sensitive than the M_{col} fit analysis. The BDT algorithm used in this search is implemented in the TMVA package [66]. BDT takes in signal and background datasets with a selected set of input variables. Input variables are the ones that show distinguishing power between signal and backgrounds. The training output is a weight file, which contains a list of weights to indicate how likely an event is signal-like with a give set of input variables. A more detail description of the BDT method is available in section 7.1. In this analysis, signal and background events are required to pass the loose selection criteria. All of the categories are combined. The signal events from the ggH and VBF Higgs production mode are mixed by weighting with respect to their production cross section. The background sample used in the training is the misidentified lepton background from the like sign region(Region II as in Table. 6.1). The list of BDT input variables is in the following list and the distribution of the variables are shown in Fig. 5.3.

- Transverse mass between the τ_h and E_T^{miss} , $M_T(\tau_h)$.
- Missing transverse energy, E_T^{miss} .
- Pseudorapidity difference between the μ and the τ_h candidate, $\Delta\eta(\mu, \tau_h)$.
- Azimutal angle between the μ and the τ_h , $\Delta\phi(\mu, \tau_h)$.

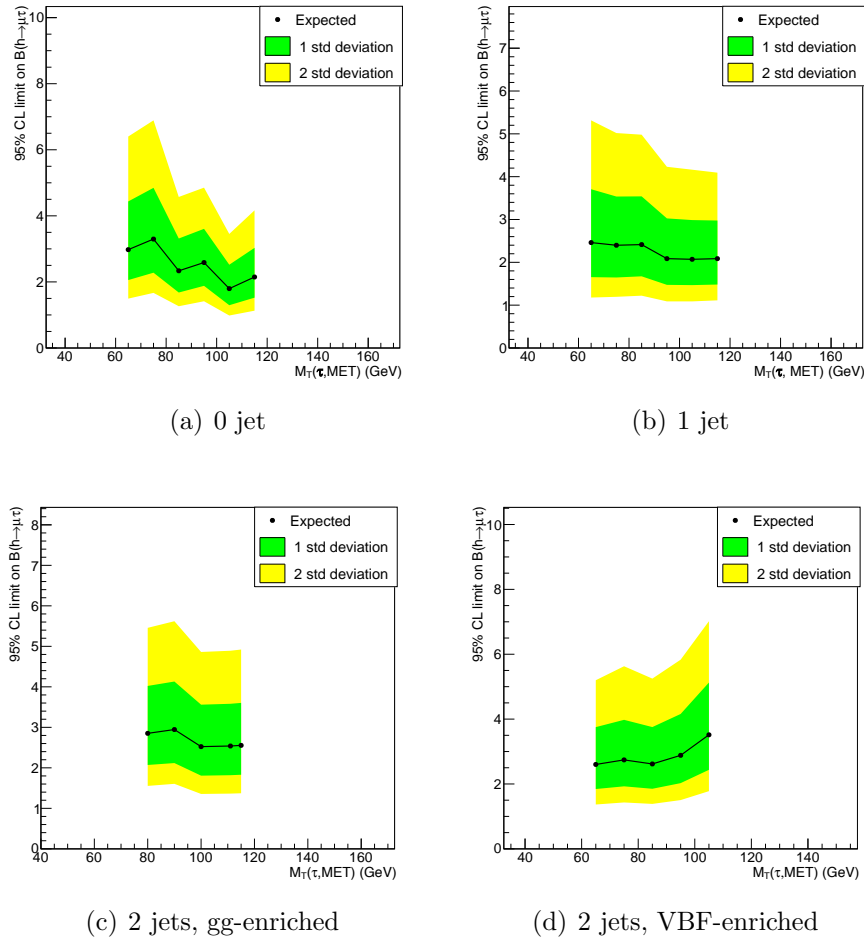


Figure 5.1. Expected limits based on an Asimov dataset as a function of $M_T(\tau, \text{MET})$ for the different categories.

TABLE 5.1

Selection criteria in each category with the optimization of the $H \rightarrow \mu\tau_h$ analysis

0-jet category
<ul style="list-style-type: none"> • $p_T^\mu > 26$ GeV, $p_T^\tau > 30$ GeV • $M_T(\tau) < 105$ GeV • No jets with $p_T^{jet} > 30$ GeV, $\eta < 4.7$, LooseID
1-jet category
<ul style="list-style-type: none"> • $p_T^\mu > 26$ GeV, $p_T^\tau > 30$ GeV • $M_T(\tau) < 105$ GeV • One jet with $p_T^{jet} > 30$ GeV, $\eta < 4.7$, LooseID
2-jet, gg-enriched category
<ul style="list-style-type: none"> • $p_T^\mu > 26$ GeV, $p_T^\tau > 30$ GeV • $M_T(\tau) < 105$ GeV • $p_T^{jet1} > 30$ GeV, $p_T^{jet2} > 30$ GeV $\eta_{jet1} < 4.7, \eta_{jet2} < 4.7$, LooseID • $M_{jj} < 550$ GeV • Two jets with $p_T^{jet} > 30$ GeV, $\eta < 4.7$, LooseID
2-jet, VBF-enriched category
<ul style="list-style-type: none"> • $p_T^\mu > 26$ GeV, $p_T^\tau > 30$ GeV • $M_T(\tau) < 85$ GeV • $p_T^{jet1} > 30$ GeV, $p_T^{jet2} > 30$ GeV $\eta_{jet1} < 4.7, \eta_{jet2} < 4.7$, LooseID • $M_{jj} > 550$ GeV • Two jets with $p_T^{jet} > 30$ GeV, $\eta < 4.7$, LooseID

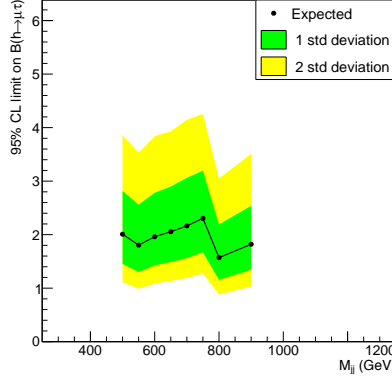


Figure 5.2. Expected limits based on an Asimov dataset as a function of M_{jj} for the 2 jet categories.

- Azimuthal angle between the τ_h and the E_T^{miss} , $\Delta\phi(\tau_h, E_T^{miss})$.
- Collinear mass, M_{col} .
- Muon p_T .
- $\tau_h p_T$.

The chosen input variables show low correlation in both samples as shown in Figure. 5.4. In the training process, overtraining needs to be carefully treated. The overtraining problem refers to the case that the classifier between signal and background samples are specific to the particular training sample used. The training recognizes the specific features that only occurs in the training samples. Most of the time, these features are caused by the limited number of training events or with the same number of events, too many variables with weak distinguishing power are used. The overtraining checks is performed by checking with the testing samples to see if similar distinguishing power can be achieved with the

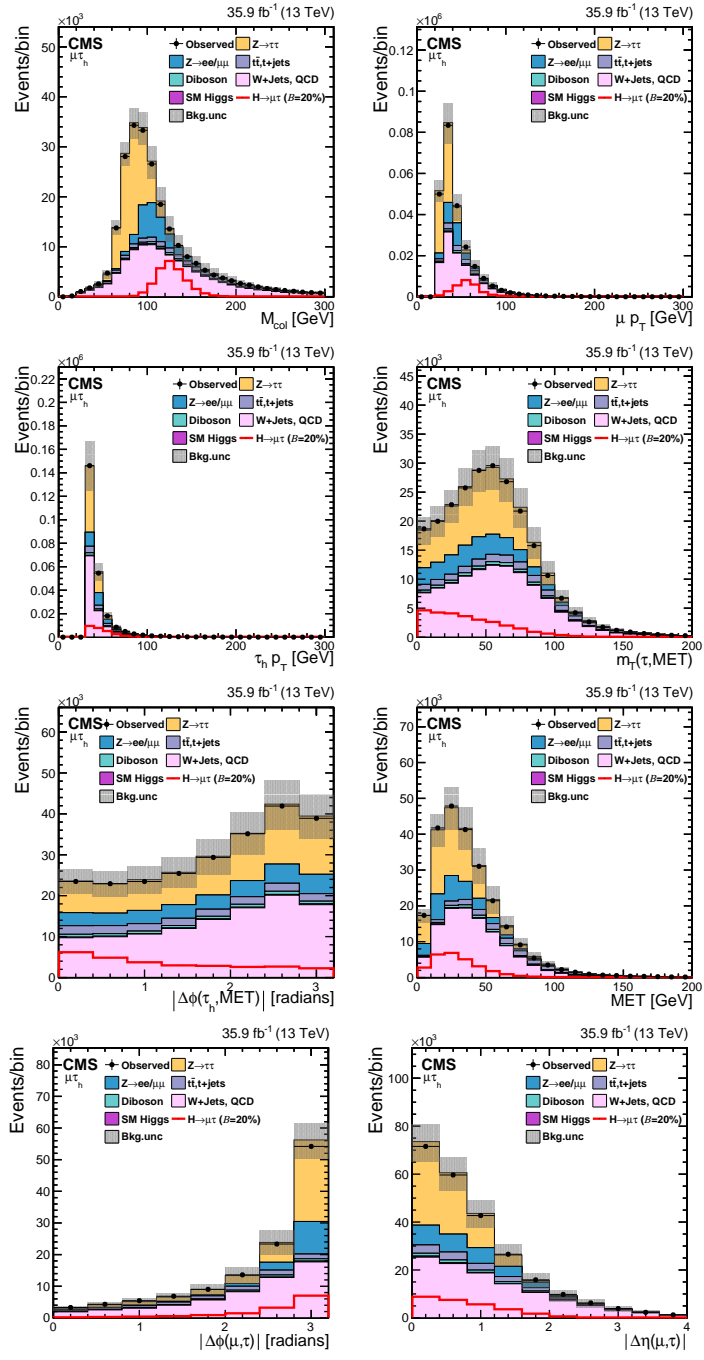
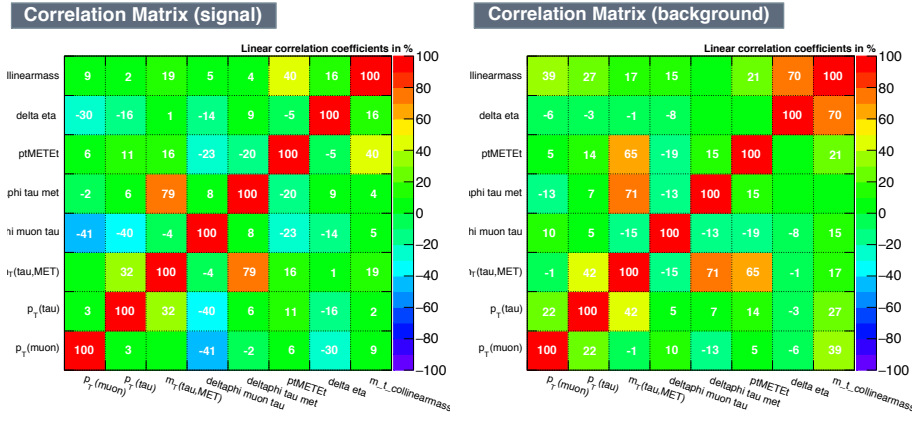


Figure 5.3. Distributions of the input variables to the BDT for the $H \rightarrow \mu\tau_h$ channel.



(a) Signal sample variables correlation (b) Background sample variable correlation

Figure 5.4. Expected limits based on an Asimov dataset as a function of $M_T(\tau, MET)$ for the different categories.

output weight file from the training samples. Training and testing samples show good agreement and the training process exempts from overtraining as indicated in Figure. 5.5.

5.2 $H \rightarrow e\tau_h$

5.2.1 Loose selection

In $H \rightarrow e\tau_h$ channel, the high level trigger that is used applies an electron p_T cut at 27 GeV at HLT level. A further cut on electron $P_T > 30$ GeV is applied. Electrons are also required to have $|\eta_e| < 2.3$ and $D_z < 0.2cm$. D_z is the longitudinal impact parameter that shows the displacement between primary vertex and track path. Electrons are required to pass the MVA based tight ID and cut based PF tight isolation $I_{rel}^e < 0.1$. Tau candidates are required to have $P_T > 30$ GeV, pseudorapidity $|\eta^\tau| < 2.3$ and the longitudinal impact parameter $D_z < 0.2$

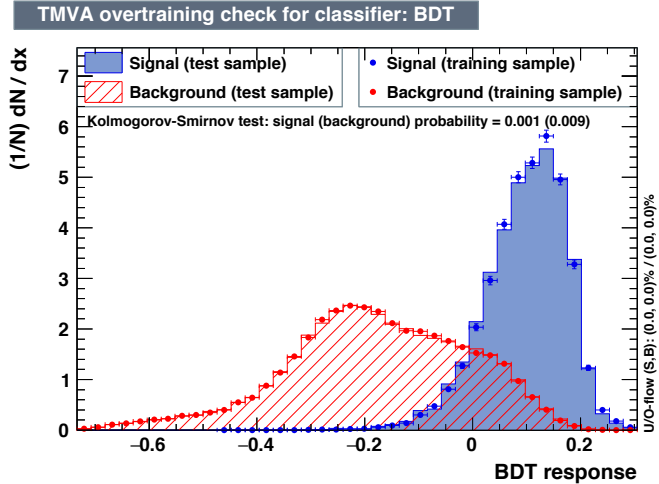


Figure 5.5. Overtraining checking for the BDT training in the TMVA package.

cm. Tau isolation used is the cut based tight tau isolation. In addition, tau candidates are required to pass the tau Decay mode finding and tau discriminator against electrons and muons. The analysis also requires no extra isolated electrons with $p_T > 10$ GeV and extra taus with $p_T > 20$ GeV. Tau and electron candidates are required to have opposite sign of charges and separate with $\Delta R > 0.4$ from any jets in the events with $p_T > 30$ GeV. All of the requirements contribute to the selections of good qualities candidates. The datasets are binned into three categories according to the number of jets in the events:

0-jet: No events have jets pass the loose PF ID and with jet $P_T > 30$ GeV, $|\eta| < 4.7$.

This category enhances the gluon-gluon fusion contribution.

1-jet: Events with one jet passes loose PF ID and jet $P_T > 30$ GeV , $|\eta| < 4.7$.

This category enhances the gluon-gluon fusion production with initial state radiation.

2 jets: Events with two jets pass loose PF ID and with jet $P_T > 30$ GeV and $|\eta| < 4.7$, This category contains both Higgs production mode and with an enhancement in VBF production mode.

With the preselection and binning of the jets numbers, the M_{col} distribution of $H \rightarrow e\tau_h$ in different categories are shown in Figure. 5.6

5.2.2 Cut-based analysis

A set of kinematics variables are used to further select signal events. In $H \rightarrow e\tau_h$ channel, similar to the $H \rightarrow \mu\tau_h$, muon and tau leptons from the signal events are highly boosted so as p_T variables play an important role in distinguishing from background events and the separation in ϕ direction is bigger between μ and τ of signal events. The variable $M_T(\tau_h)$ which is the transverse mass form by the reconstructed τ and MET is also used in the selection. In the two jets category, the invariant mass of two jets M_{jj} is used as a cut variable. The cuts have been optimized to have the most stringent expected limits with the Asimov dataset. The detailed cuts used for $H \rightarrow e\tau_h$ is shown in table. 5.2.

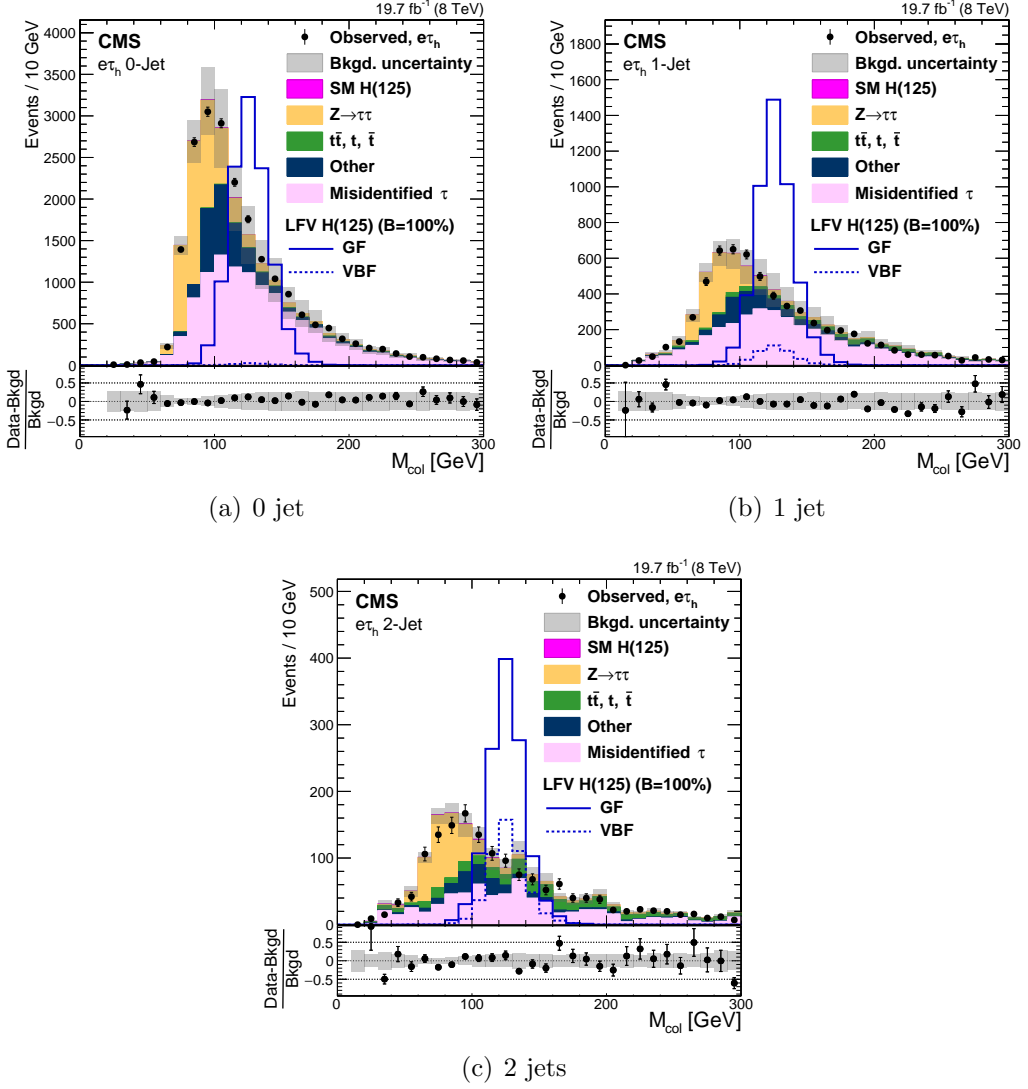


Figure 5.6. With loose selection conditions, the comparison of the observed collinear mass distributions with background from prediction. The shaded grey bands indicate the total background uncertainty. The open histograms correspond to the expected signal distributions for $\mathcal{B}(H \rightarrow e\tau_h) = 100\%$ in the 0-jet, 1-jet and 2-jet categories, respectively.

TABLE 5.2

Selection criteria for each event category after cut optimization, for the
 $H \rightarrow e\tau_h$ channel

0-jet category
<ul style="list-style-type: none"> • $p_T^e > 45$ GeV, $p_T^\tau > 30$ GeV, $\Delta\phi_{e\tau} > 2.3$ • $M_T(\tau) < 70$ GeV • No jets with $p_T^{jet} > 30$ GeV, $\eta < 4.7$, LooseID
1-jet category
<ul style="list-style-type: none"> • $p_T^e > 35$ GeV, $p_T^\tau > 40$ GeV • One jet with $p_T^{jet} > 30$ GeV, $\eta < 4.7$, LooseID
2-jet category
<ul style="list-style-type: none"> • $p_T^e > 35$ GeV, $p_T^\tau > 30$ GeV • $M_T(\tau) < 50$ GeV • $p_T^{jet1} > 30$ GeV, $p_T^{jet2} > 30$ GeV, $\eta_{jet1} < 4.7, \eta_{jet2} < 4.7$, LooseID • $\Delta\eta(jet1, jet2) > 2.3$ • $M_{jj} > 400$ GeV • Two jets with $p_T^{jet} > 30$ GeV, $\eta < 4.7$, LooseID

CHAPTER 6

LFV analysis background estimation

6.1 Background estimates for $H \rightarrow \mu\tau_h$

6.1.1 Misidentified Leptons

The misidentified lepton backgrounds are estimated with a fully data driven method using collision data. In $H \rightarrow \mu\tau_h$ channel, the misidentification τ and μ lepton rate is obtained from an independent $Z + \text{jets}$ data sets and then applied to a control region that is orthogonal to the signal region to estimate the misidentified lepton backgrounds. The control regions for the estimation and validation of the misidentified lepton background are shown in Table. 6.1. Region I is the signal region with full selection applied. Region III is the background enriched region, in which one or two leptons have loose isolation but not tight isolation. Region II is the same to Region I except that the μ and τ lepton pairs have the same electric charge. Similarly as Region IV to Region III. Region III is used to estimate the misidentified background in Region I. Region II and IV are used in the validation of the method.

$Z \rightarrow \mu\mu$ is used in $Z + \text{jets}$ collision dataset to estimate both misidentified τ and μ lepton rates. Z bosons are selected in the invariant mass window $70 < M_{ll} < 110$ GeV and the trigger that require isolated muons have $p_T > 24$ GeV

TABLE 6.1

Definition of the samples used to estimate the misidentified lepton background.

Region I	Region II
ℓ_1^\pm (isolated)	ℓ_1^\pm (isolated)
ℓ_2^\mp (isolated)	ℓ_2^\pm (isolated)
Region III	Region IV
ℓ_1^\pm (isolated)	ℓ_1^\pm (isolated)
ℓ_2^\mp (not-isolated)	ℓ_2^\pm (not-isolated)

is used in the selection. Two muons that are composed of Z bosons are required to have $p_T > 26$ GeV, $|\eta| < 2.4$, cut based tight muon isolation($I_{rel}^\mu < 0.15$) and passing the muon medium ID. In the Z+jets samples, with the selected Z boson in an event, the remaining jets are checked if they pass τ or μ selection.

To estimate the misidentified τ lepton rate, The jets in the sample Z + jets are checked if they pass the τ isolation ID. The ratio f_τ of tight isolated τ to very loose isolated τ is extracted first. Then the misidentified τ leptons rate ratio $\tau(f_\tau)$ is calculated as in Equation . 6.2, in which ℓ stands for e, μ or τ and N_ℓ stands for the number of leptons. The misidentified leptons in the signal region are estimated with $\tau(f_\tau)$ applied to the events in Region III which is defined in Table. 6.1, specifically, Region III is defined in the same selection condition as the signal region Region I , but τ leptons are required to pass the very loose MVA isolation and not pass the tight MVA isolation.

$$f_\ell = \frac{N_\ell(Z + \text{jets } \ell \text{ tight Iso})}{N_\tau(Z + \text{jets } \ell \text{ loose Iso})} \quad (6.1)$$

$$\ell(f_\ell) = \frac{f_\ell}{1 - f_\ell} \quad (6.2)$$

$$(6.3)$$

The expected contribution from WW, WZ, ZZ samples are subtracted with simulation, in which the third lepton is genuine lepton. The misidentified τ lepton rate $\tau(f_\tau)$ shows dependence on tau p_T , tau decay mode and spacial geometry η . Thus $\tau(f_\tau)$ is applied in term of tau p_T , tau decay modes and ECAL barrel and endcap seperately. The distribution of f_τ is shown in Fig. 6.1, which shows a comparison of the estimated f_τ between data and simulated Z+jets samples. The distribution of f_τ on η is also shown, which show less dependency.

The estimation of the μ misidentified rate the is same as the τ misidentified rate, but checks if the jets in Z + jets samples pass the muon isolation. As in Equation. 6.2, f_μ is defined as the ratio between tight cut based muon isolation($I_{rel}^\mu < 0.15$) and loose cut based muon isolation($I_{rel}^\mu < 0.25$). The misidentified μ lepton rate $\mu(f_\mu)$ is calculated by Equation. 6.1. $\mu(f_\mu)$ is a weight to apply to Region III. In the case of estimating the misidentified μ , Region III is defined as Regin I but with μ passing the loose cut based muon isolation and not passing tight cut based muon isolation. The ratio f_μ is shown in Figure. 6.2 in term of muon p_T and $|\eta|$ distribution.

There is double-counting between the estimated misidentified muon and tau lepton when both of the leptons are fake ones. The double-counting events are estimated as in Equation. 6.5. In the equation, the N(Region III) stands for the events in Region III. In this case, Region III is defined as muon leptons passing the lose isolation, but not passing the tight isolation, while tau leptons pass the very loose isolation but not pass the tight isolation. The final misidentified lepton

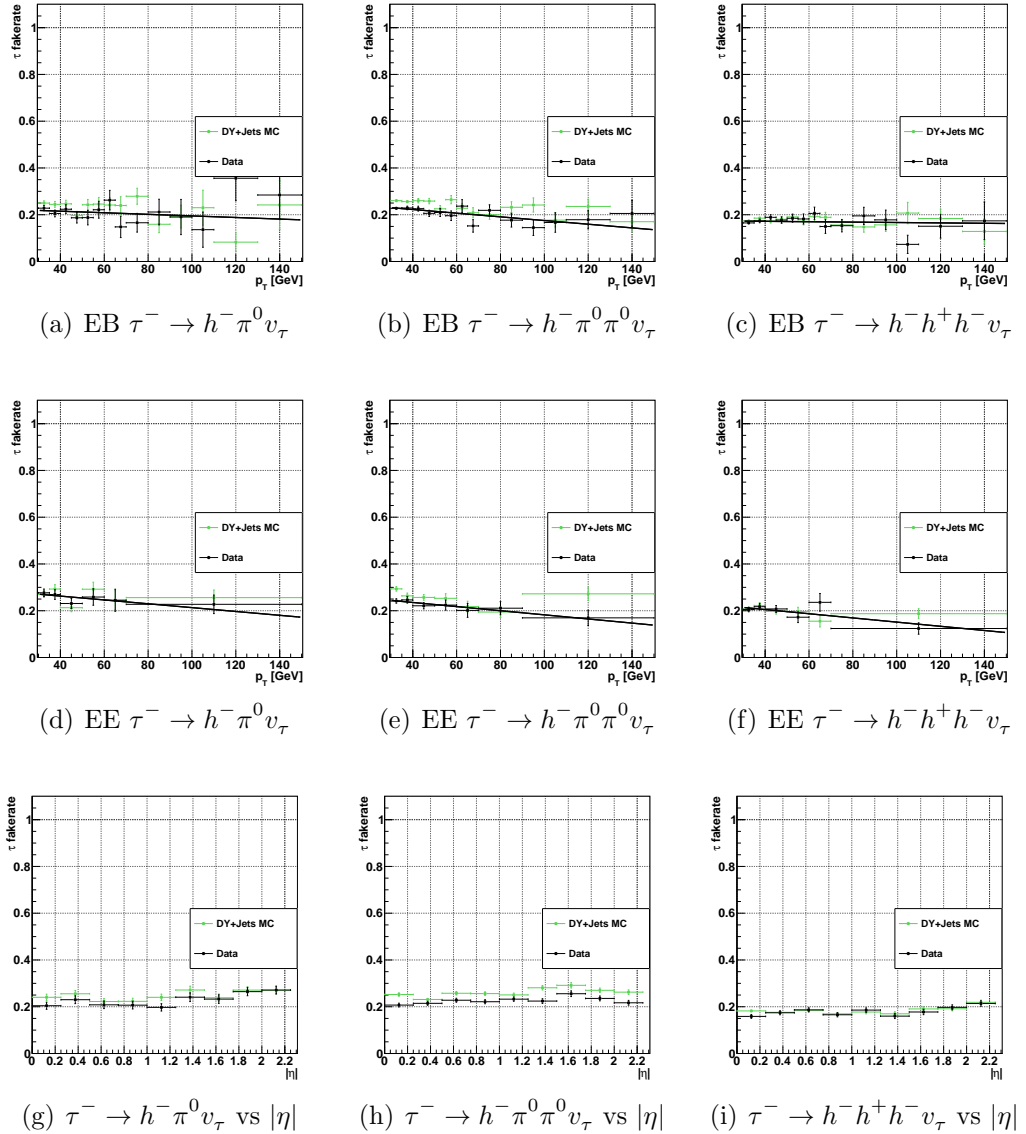


Figure 6.1. f_τ ratio for the τ fake rate calculation shows in term of tau decay modes, p_T , ECAL barrel, ECAL endcap, and $|\eta|$

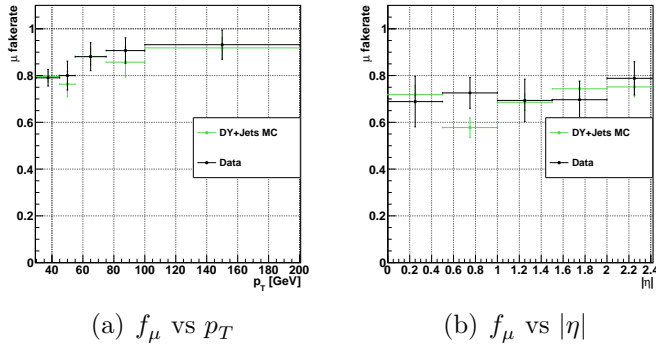


Figure 6.2. f_τ ratio for the μ fake rate calculation shows in term of muon p_T and $|\eta|$.

background obtained by adding the misidentified muon and tau background and deducts the double-counting events between these two.

$$N(\text{double-counting}) = \frac{f_\tau \cdot f_\mu}{(1 - f_\tau) \cdot (1 - f_\mu)} \cdot N(\text{Region III}) \quad (6.4)$$

In $H \rightarrow \mu\tau_h$ channel, the validation of the misidentified lepton background with a fully data driven method is performed in a like-sign sample and also a W+jets enriched control region. The like-sign sample validation requires the events pass the loose selection, the same as the signal region, but with inverted charge. The misidentified background is enriched by the requirement of inverting charge. In the W+jets enriched control region, events that pass the loose selection are further selected with $M_T(\tau) > 60$ GeV and $M_T(\mu) > 80$ GeV. In both of the control regions, the misidentified background is the dominant one, as shown in Fig. 6.3.

Applying the $\tau(f_\tau)$ as weight, the like-sign and W+jets control regions show good data and MC agreement with the fully data driven method, .

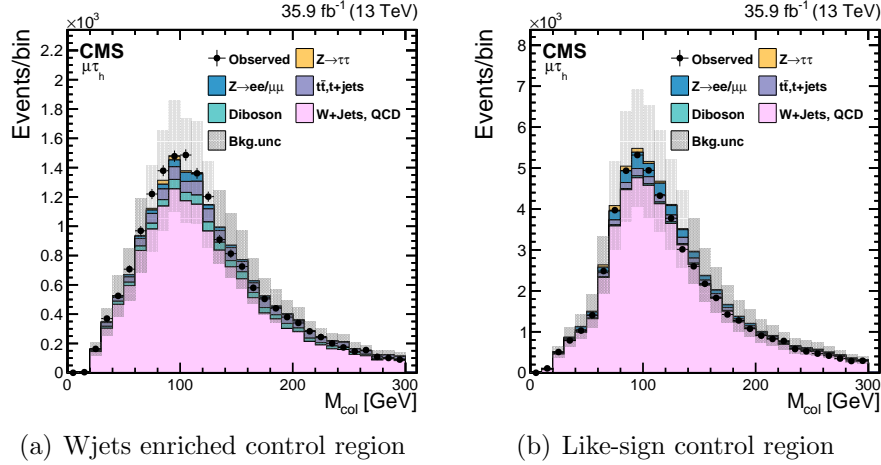


Figure 6.3. The validation of the fully data driven method for the misidentified lepton background. The uncertainties in the distributions include both statistics and systematics uncertainties.

6.1.2 Other backgrounds

The decays of $Z \rightarrow \tau\tau$ and $Z \rightarrow \mu\mu$ are also major backgrounds in this channel. In $Z \rightarrow \tau\tau$, the muons arise from a tau lepton decay, while in $Z \rightarrow \mu\mu$, one of the muon can be misidentified as a tau. In other smaller backgrounds, the $\mu\tau$ pairs can be produced from the weak decays of quarks and vector bosons. These smaller backgrounds include standard model Higgs production($H \rightarrow \tau\tau, WW, t\bar{t}$), single top quark, di-boson(WW,WZ,ZZ). A full list of background used is in the

Table. ???. These backgrounds are all estimated with Monte Carlo simulation and normalized to the cross-section of collision dataset.

In the $Z \rightarrow \mu\mu$ background, an additional scale factor is applied to the tau leptons that do not come from real taus. This is checked in the Monte Carlo generator level. The scale factor is applied in term of $|\eta|$ as shown in Table. 6.2.

TABLE 6.2

Scale factor to the events in which a muon is misidentified as a tau

$ \eta $ ranges	Correction values
0-0.4	1.263
0.4-0.8	1.364
0.8-1.2	0.854
1.2-1.7	1.712
1.7-2.3	2.324

6.2 Background estimates for $H \rightarrow e\tau_h$

6.2.1 Misidentified Leptons

The misidentified lepton background is significant in the $H \rightarrow e\tau_h$ channel. This background arises mainly from W+jets and QCD multijets. The events may

have one or both leptons are misidentified. The $H \rightarrow e\tau_h$ channel in the analysis performed on the 8 TeV dataset, both misidentified electron and tau leptons are estimated.

Similar to $H \rightarrow \mu\tau_h$ channel, the misidentified background in $H \rightarrow e\tau_h$ is estimated with a fully data driven method, with independent collision dataset of Z+jets, in which the Z boson decays into two electrons. Data sets are divided into four control regions for this estimation as in Table. 6.1. Region II is used to extract the misidentified background in signal region, Region I, while Region II and Region IV are used for the validation of the fake rate. In the Z+jets data set selection, a trigger that selects electron with $p_T > 27$ GeV(HLT_Ele27_WP80) is used. The two electrons in Z+jets are required to have $p_T > 30$ GeV, $|\eta| < 2.3$, tight electron MVA ID and cut based tight PF isolation($I_{rel}^e < 0.1$). The invariant mass formed by the two electrons are required to be in the Z boson mass window(70 GeV $< M_{ee} < 110$ GeV). Then the jets in the events are checked if they pass τ or e selection. Tau leptons should have $p_T > 30$ GeV, $|\eta| < 2.3$, passing the tau decay mode finder and discriminator against electrons and muons. Electrons pass the same conditions as the elections used in forming the Z boson mass peak, but with different isolation requirements. Tau leptons use the cut based tight or loose isolation, while loose or tight MVA based electron isolation have the value $I_{rel}^e < 0.1$ and $I_{rel}^e < 0.2$ respectively. After the selection, the fake ratio f_τ is defined as the number of tau leptons passing the tight isolation divided the number of tau leptons passing the loose isolation. Similarly the fake ratio f_e is defined as the number of elections passing the loose isolation divided by the number of electron passing the tight isolation as shown in Equation. 6.1. With the fake ratio f_τ and f_e , the electron and tau fake rate $\tau(f_\tau)$ and $e(f_e)$ are estimated

according to Equation. 6.2. The fake ratio for tau leptons and electrons are shown in Figure. 6.4.

The tau and electron fake ratio is applied as a function of η . The background of three prompt leptons from WW, WZ, ZZ processes are deducted with Monte Carlo simulations. The tau and electron misidentified backgrounds are estimated separately, the double-counting events in which both leptons are misidentified objects are estimated with Equation. 6.5. In the equation, $N(\text{Region III})$ in $H \rightarrow e\tau_h$ channel satisfies the condition that both leptons are loose isolated but not tight isolated. The validation of the fully data driven method is done with Region II and Region IV. The distribution of the M_{col} is checked in the same sign region of the two leptons, shown in Figure. 6.5. The observed data agrees well with the events from MC and misidentified background from data driven method.

6.2.2 $Z \rightarrow \tau\tau$

$Z \rightarrow \tau\tau$ is another significant background in the $H \rightarrow e\tau_h$ channel. In the case one of the tau leptons decay to a electron and the other hadronically decay. The background is estimated with an embedding technique[37], which starts by selecting the $Z \rightarrow \mu\mu$ events from collision data. The muons pass loose muon selection and then are replaced by simulated τ leptons and reconstructed with PF algorithm. The key advantage of this technique is that the major topologies like missing energy, jet multiplicity, underlying events are directly modelled from data. Compared with the MC prediction, the visible mass peak from the modeling of the embedding sample shifts 2%. This is due to the difference in the final-state radiation of photons from the muon and tau. Identification and isolation correction for this shift to embedded sample are obtained by comparing with Monte Carlo

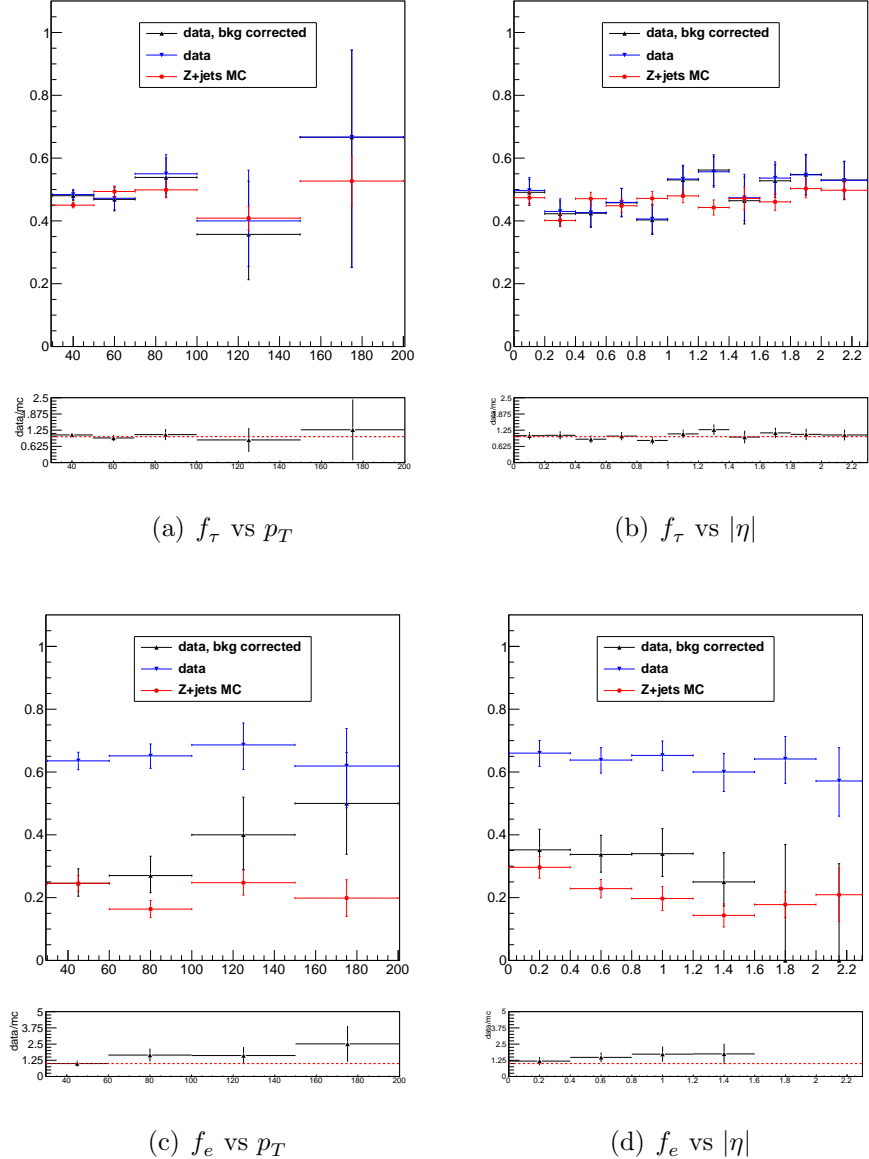


Figure 6.4. f_τ and f_e ratio for the mididentification calculation shows in term of p_T and $|\eta|$

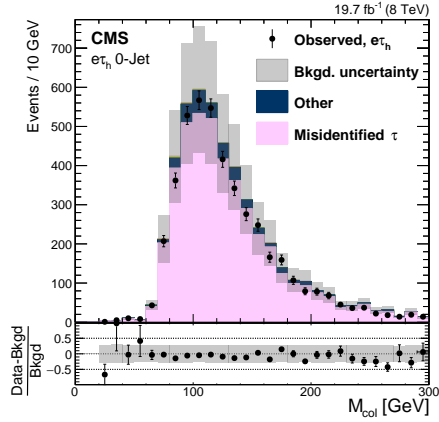


Figure 6.5. Data driven method validation in Region II with e and τ leptons in same sign of charge

simulations.

6.2.3 Other backgrounds

The production of $t\bar{t}$ pairs is also a background. The leptonic decay W bosons can produce opposite sign lepton pair and missing energy. The shape of this background is obtained from simulation samples and normalized to $t\bar{t}$ control region sample. The control region is defined as the 2-jet selections in this channel but with additional requirement that at least one of the jets is b-tagged. The events in $t\bar{t}$ control samples are required to pass the 2-jet base selection in $H \rightarrow e\tau_h$ channel and at lease one the jets is identified as a b jet.

The other backgrounds presented in the samples are Z+jets in which one of the electrons is misidentified as a τ lepton. Di-boson(WW,WZ,ZZ) events, single Top, SM Higgs boson production($H \rightarrow \tau\tau$) and $W\gamma^{(*)}$. These backgrounds are all estimated from Monte Carlo simulation.

CHAPTER 7

Signal extraction and systematics

7.1 Boosted decision trees method

The boosted decision trees(BDT) [66, 80] is used in the $H \rightarrow \mu\tau_h$ analysis. The $H \rightarrow \mu\tau_h$ result which is referred as BDT fit analysis, with this MVA method, improves a factor of two with respect to the M_{col} fit analysis. The BDT algorithm is composed of two parts, the boosting algorithm and the decision tree. The AdaBoost(adaptive boost) is the boosting algorithm used in the $H \rightarrow \mu\tau_h$ analysis.

The decision tree is a simple two dimensional tree structure. The BDT takes in one signal and one background dataset, which are further divided into training and test samples. A set of selected variables are used the training. At the initial node of the tree structure, events are ordered by the value of variables. The node is split into two branches by a binary selection of the variable that gives the best separation between signal and background in each of the branch. The splitting continues until the training reaches the specified limit set for the number of layers or the number of events in the branch, then the last notes are called leaves. Depending on the main population inside each leaf, the leafs are categorized as signal leaves or background leaves. An example of the tree structure is shown in Figure. 7.1. Criteria are needed for the selection of variables at the node or branch. Purity is defined as in Equation. 7.1, in which the superscript s stands

for signal events, b for background events and W for the event weight.

$$P = \frac{\sum_s W_s}{\sum_s W_s + \sum_b W_b} \quad (7.1)$$

Through the definition of purity, a couple of criteria can be configured. Here the one called Gini, defined in Equation. 7.2, is selected also it is the default one for the BDT in TMVA package.

$$Gini = \left(\sum_{i=1}^n W_i \right) P(1 - P) \quad (7.2)$$

In each splitting, the variable value that maximize the criterion in Equation. 7.3 is selected.

$$Criterion = Gini_{n-1} - Gini_{n \ left} - Gini_{n \ right} \quad (7.3)$$

The decision tree method is powerful, but the performance can suffer from fluctuations. The selection of two variables with similar selection quality may be affected by a small change in the training sample. One of the solution is introducing the boosting algorithm. The boosting algorithm not only helps stabilize the decision tree training with respect to the small fluctuations, but also enhances the classification. The AdaBoost is one of the boosting algorithms. In AdaBoost, after the first decision tree training, the misclassified events get higher even weights and are taken as inputs into the second tree. Typically the AdaBoost training 1000 to 2000 trees. The misclassified event weights depend on the training error

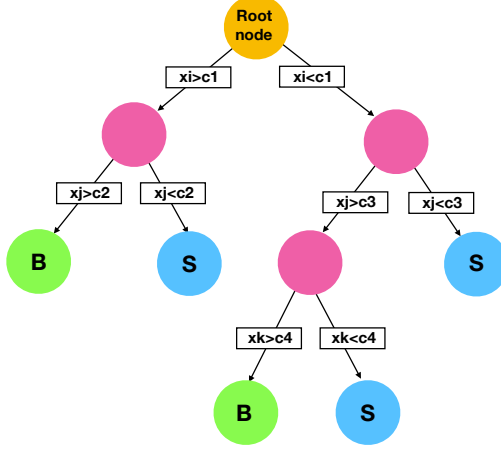


Figure 7.1. Tree structure example in BDT

of each decision tree. The training error is calculated as in Equation. 7.4,

$$\text{error}_m = \frac{\sum_{i=1}^N w_i I(y_i \neq T_m(x_i))}{\sum_{i=1}^N w_i} \quad (7.4)$$

in which the superscript m is the tree label and w is the event weight. The y_i indicates the i-th event type, 1 for signal and -1 for background. $T_m(x_i)$ indicates the type of the leaf event i with variable x land on, 1 for signal leaf and -1 for background leaf. The variable $I(y_i \neq T_m(x_i))$ constructs on the variables y_i and T_m equal 1 if $y_i \neq T_m(x_i)$ or 0 if $y_i = T_m(x_i)$. As shown in Equation. 7.5, with the intermediate quantity α_m for the tree m, the weight for event i is updated to its new value.

$$\alpha_m = \beta \times \ln((1 - \text{error}_m) / \text{error}_m) \quad (7.5)$$

$$w_i \rightarrow w_i \times e^{\alpha I(y_i \neq T_m(x_i))} \quad (7.6)$$

While error_m is required to be less than 0.5 so as the event weights are updated to the right direction. The learning rate parameter β can be used to adjust the step size of each re-weighting. The default value of β is 1. Event weights in each tree is renormalized to keep the summed weights constant. The final score of each event after the boosting and training processes is obtained with Equation. 7.7. High score indicates a signal like event while low score indicates a background like event.

$$T(x) = \sum_{m=1}^{N_{tree}} \alpha_m T_m(x) \quad (7.7)$$

7.2 Statistical methods

Physics results are extracted with statistical methods. The limit of branching ratio with confident level(CL) method, significance and best fit branching fraction are mentioned in the analysis.

The probability density function(PDF) and likelihood function are the basic functions used. The PDF of a continuous variable x can be interpreted as the likelihood of x at its different values. The PDF holds the property that it is normalized to unity.

$$\int f(x)dx = 1$$

Usually the PDF of a variable is accompanied with a set of parameters, thus the PDF is usually written in the form $f(\text{data}|\alpha)$, which means the probability density function of the variables in data given the parameter set α . These parameters can come from various sources, for example, from theory estimation, detector response and

Monte Carlo simulation. All of the parameters in a model or a system, besides the parameters of interests, the other parameters that have an impact on the results are referred as nuisance parameters.

Likelihood function of the same model $L(data|\alpha)$ is a function of parameter set α given data under study. In particle physics, the likelihood function is more often in the form of $L(data|\mu, \theta)$, in which the μ stands for signal strength modifier and the θ stands for a full suite of nuisance parameters. The data in a Likelihood function can be experimental data or pseudo-data which is produced to generate sample distribution. Taking the counting experiment as an example, the PDFs and likelihood function in a binned sample can be estimated with poisson distribution.

The PDF is in the form as

$$f(data|u, \theta) = \prod_i \frac{(\mu s_i + b_i)^{n_i}}{n_i!} e^{-\mu s_i - b_i}$$

The s_i and b_i stand for the expected number signal and background events respectively and both of them are a function of nuisance parameter θ as $s_i(\theta)$ and $b_i(\theta)$. The n_i represents the number of events observed in bin i. The likelihood function in the numerical form is similar to the PDF but implement the systematic error PDFs $\rho(\theta|\tilde{\theta})$ if there are systematics considered in the model [3]. The form of the likelihood function can be expressed as

$$\mathcal{L} = \prod_i \frac{(\mu s_i + b_i)^{n_i}}{n_i!} e^{-\mu s_i - b_i} \cdot \rho(\tilde{\theta}|\theta)$$

Both of the PDF and the likelihood function rely on the knowledge of nuisance parameters. Auxiliary measurements or control regions are often used for the scale estimation of systematic uncertainties. Through the observations in different

auxiliary measurements, a PDF $p(\tilde{\theta}|\theta)$ which is referred as the posteriors can be measured. Together with $\pi(\theta)$ which is referred as a prior, the systematic error PDFs can be constructed under the Bayes' theorem as

$$\rho(\theta|\tilde{\theta}) \sim p(\tilde{\theta}|\theta) \cdot \pi_\theta(\theta)$$

The systematic error PDFs can be improved and less affected by the choice of prior $\pi(\theta)$ [73] by the auxiliary measurements.

In the search of lepton flavour violaton Higgs decay, the discovery will be the observation of the Higgs events either decay into $\mu\tau$ pairs in 13 TeV search or $e\tau$ pairs in 8 TeV search. The LFV is forbidden in Standard Model(SM), thus, if taking the SM as a background only model, roughly speaking, a discovery can be claimed if the observation is not compatible with the background only model [46]. To test the compatibility of the observed data with respect to the background only model and further calculate limits on the signal strength modifier of the signal+background hypothesis, the quantity test statistics and the PDFs of the two model under tested are needed.

The test statistics is a function which can map a set of data into a number. According to the Neyman-Pearson lemma, the likelihood ratios of two models under test give the most powerful test, which is expressed as

$$\tilde{q}_\mu = -2\ln \frac{\mathcal{L}(data|\mu, \tilde{\theta}_\mu)}{\mathcal{L}(data|\hat{\mu}, \hat{\theta})}$$

The μ is the given signal strength modifier and $0 < \hat{\mu} < \mu$. The $\tilde{\theta}$ is referred as conditional maximum likelihood estimator, given the signal strength modifier μ , while in the denominator, $\hat{\mu}$ and $\hat{\theta}$ are allowed to flow freely to max-

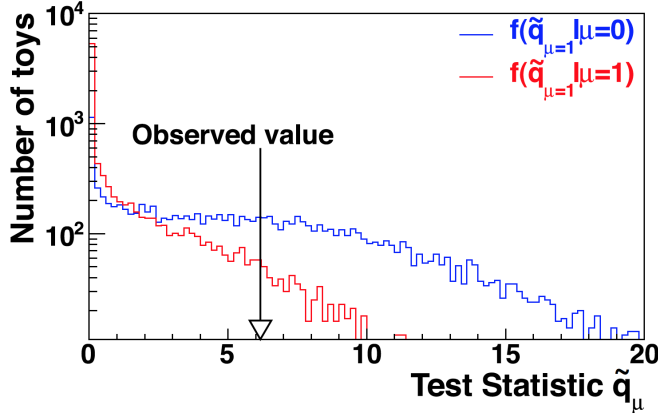


Figure 7.2. Test statistics distribution of signal+background and background only PDFs and the observed valued shown in arrow.

imize the likelihood. The PDFs of signal+background model and background only model can be calculated in the following way. The observed θ_μ^{obs} and θ_0^{obs} for signal+background and background only model are obtained by maximizing the likelihood function respectively, also the observed \tilde{q}_μ^{obs} is calculated give a μ . The PDFs of signal+background model $f(\tilde{q}_\mu|\mu, \theta_\mu^{obs})$ and background only model $f(\tilde{q}_\mu|0, \theta_0^{obs})$ are constructed with the MC pseudo-data as shown in Figure. 7.2.

The confident Level(CLs) is defined with two values p_μ and $1-p_b$. In signal+background model, p_μ is defined as

$$p_\mu = P(\tilde{q}_\mu \geq \tilde{q}_\mu^{obs} | \text{signal+background}) = \int_{\tilde{q}_\mu^{obs}}^{\infty} f(\tilde{q}_\mu|\mu, \hat{\theta}_\mu^{obs}) d\tilde{q}_\mu$$

In background only model $1-p_b$ is defined as

$$1 - p_b = P(\tilde{q} \geq \tilde{q}_\mu^{obs} | \text{background only}) = \int_{\tilde{q}_0^{obs}}^{\infty} f(\tilde{q}_\mu|0, \hat{\theta}_0^{obs}) d\tilde{q}_\mu$$

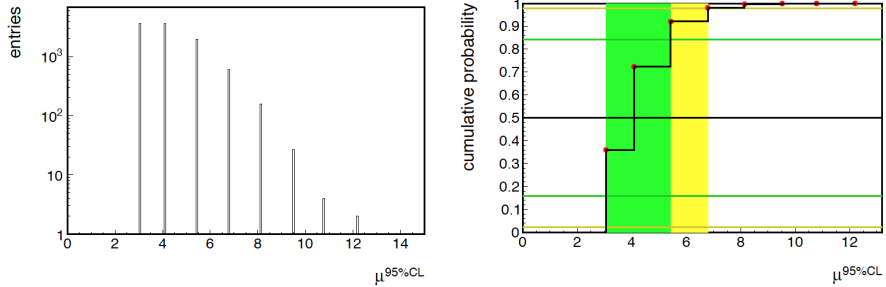


Figure 7.3. Signal strength modifier μ at 95% CL_s distribution from the MC pseudo-data. The right plot is the cumulative distribution of $\mu^{95\%}$ with $\pm 1\sigma$ and $\pm 2\sigma$ bands.

The CL_s then is expressed as

$$CL_s = \frac{p_\mu}{1 - p_b}$$

For a given value of signal strength modifier μ , $CL_s \leq \alpha$, then the signal+background is said excluded with $(1 - \alpha) CL_s$. Usually α is picked as 95%.

The expected limit shown in lepton flavour violation Higgs decay is the median 95% CL_s upper limit with the $\pm 1\sigma$ and $\pm 2\sigma$ bands in the background only model. By generating a large number of background only pseudo-data, the CLs and $\mu^{95\%}$ of each toy are calculated. An example of $\mu^{95\%}$ distributions is shown in Figure. 7.3. As shown in the cumulative distribution of $\mu^{95\%}$, the median corresponds to 50%, while $\pm 1\sigma$, $\pm 2\sigma$ correspond to range 16% to 84% and 2.5% to 97.5% respectively.

The estimator p value and significance are used to check if the data is compatible with background only model. The test statistics in the checking of background

only model is expressed as

$$\tilde{q}_\mu = -2\ln \frac{\mathcal{L}(data|0, \tilde{\theta}_\mu)}{\mathcal{L}(data|\hat{\mu}, \hat{\theta})}$$

Similar procedure as mentioned above can be used to get the PDF of background ground only model $f(q_0|0, \hat{\theta}_0^{obs})$ and q_0^{obs} . The p-value corresponding to the experimental observable is calculated as

$$p_0 = P(q_0 \geq q_0^{obs}) = \int_{q_0^{obs}}^{\infty} f(q_0|0, \hat{\theta}_0^{obs}) dq_0$$

Significance Z of the observable with respect to the background only model test can be derived from p value [3].

$$p = \int_Z^{\infty} \frac{1}{\sqrt{2\pi}} \exp(-x^2/2) dx$$

The term used in the discovery as 5σ correspond to $Z=5$ and $p=2.8 \times 10^{-7}$. The distribution of test statistics tends to be chi-squared distribution in large statistics according to the Wilk's theorem, which gives a quick way of estimating of PDFs in test statistics [46]. In the case when the expected number of events is large, expected limit with this asymptotic approximation gives a fairly well performance and saves the computing time for toy samples. The asymptotic approximation can be used in the estimation of p value as

$$p^{estimate} = \frac{1}{2} \left[1 - \text{erf} \left(\sqrt{q_0^{obs}/2} \right) \right]$$

7.3 Systematics

Systematic uncertainties originated from different sources that experimentally or theoretically affect the physics results. These uncertainties are considered by the effects on the normalization and the shapes of the distribution from different processes.

7.3.1 Systematics used in $H \rightarrow \mu\tau_h$

The systematic uncertainties considered in this analysis are summarized in Table. 7.1 and Table. 7.2. The uncertainty on muon trigger, identification and isolation together amounts to 2% and the hadronic tau lepton efficiency amounts to 5%. The uncertainties on lepton selections that include trigger, ID, isolation efficiencies are estimated with tag and probe method with Z boson data sets [33, 39, 67, 68, 70]. The systematic uncertainty of b tagging veto is taken from the uncertainty of b tagging veto efficiency measurement, which adjusts b tagging veto performance in the simulation to match data sample. The exact values used in each category of $t\bar{t}$ and single top samples are summarized in Table. 7.3. The uncertainties on $Z \rightarrow \tau\tau$, WW, WZ, ZZ, $t\bar{t}$, single top backgrounds mainly originate from the uncertainties on the cross section measurements. The normalization uncertainty of μ misidentifying τ scale factor measurement and the uncertainty on $Z \rightarrow \mu\mu$ process together amounts to 25%. An additional shape uncertainty on muon misidentifying tau is extracted from the measurement of the scale factor and treats independently of different hadronic tau decay modes. The uncertainty of the misidentified lepton background is estimated from the matching of the same sign control region which is defined as region II in Table. 6.1. The 30% on normalization uncertainty correlated between each category and additional

10% uncorrelated between each category are taken as a conservative estimation. Only the tau shape uncertainties are considered, which are taken from the variations of the misidentified tau parameters in the fitting. The muon misidentified shape uncertainty is omitted as it would be negligible compared with the bin-by-bin uncertainty applied. The shape uncertainties of jet energy scale is estimated by varying the fitting parameters of different sources that affect this scale by one σ . The tau energy scale is treated as shape uncertainties and each of the tau decay modes is considered independently. The unclustered energy refers to the energy deficiency from the jets $p_T < 10$ GeV and the PF candidates that are not included in the jet reconstruction. The unclustered energy uncertainty is considered independently for charged particles, photons, neutral hadrons and very forward particles. The uncertainties on Higgs boson cross section is affected by the renormalization scales, factorization, parton distribution functions(PDF) and the strong coupling constant(α_s). These uncertainties contribution in normalization scale and are taken from the latest recommendation [49]. The uncertainties on Higgs cross section also affect the acceptance and result in the migration of events between categories. The bin-by-bin uncertainty is applied to account for the statistics uncertainties within each bin. These uncertainties are uncorrected between different bins and categories. The uncertainty of integrated luminosity [7] amounts to 2.5%.

7.3.2 Systematic uncertainties in $H \rightarrow e\tau_h$

The systematic uncertainties affect the $H \rightarrow e\tau_h$ analysis are summarized in Table. 7.4, 7.6 and 7.5, which include the ones affect the normalization scale and

TABLE 7.1

Part one of the systematic uncertainties considered in $H \rightarrow \mu\tau_h$ analysis.

All of the uncertainties listed in the systematic tables are correlated between categories besides the ones after the sign \oplus . These are the uncertainties correlated within each category but independent between categories. The theoretical uncertainties related to the acceptance and migration of events are listed in a range. The negative or positive values indicate anticorrelated or correlated between categories

Systematic uncertainty	$H \rightarrow \mu\tau_h$
Muon trigger/identification/isolation	2%
Hadronic tau lepton efficiency	5%
b tagging veto	2.0–4.5%
$Z \rightarrow \tau\tau + \text{jets}$ background	10% \oplus 5%
WW, ZZ background	5% \oplus 5%
t <bar>t background</bar>	10% \oplus 5%
Single top quark background	5% \oplus 5%
$\mu \rightarrow \tau_h$ background	25%
Jet $\rightarrow \tau_h, \mu$ background	30% \oplus 10%
Jet energy scale	3–20%
τ_h energy scale	1.2%

TABLE 7.2

Part two of the systematic uncertainties considered in $H \rightarrow \mu\tau_h$ analysis

Systematic uncertainty	$H \rightarrow \mu\tau_h$
$\mu \rightarrow \tau_h$ energy scale	1.5%
μ energy scale	0.2%
Unclustered energy scale	$\pm 1\sigma$
Renorm./fact. scales (g gH) [49]	3.9%
Renorm./fact. scales (VBF and VH) [49]	0.4%
PDF + α_s (g gH) [49]	3.2%
PDF + α_s (VBF and VH) [49]	2.1%
Renorm./fact. acceptance (g gH)	-3.0% – +2.0%
Renorm./fact. acceptance (VBF and VH)	-0.3% – +1.0%
PDF + α_s acceptance (g gH)	-1.5% – +0.5%
PDF + α_s acceptance (VBF and VH)	-1.5% – +1.0%
Integrated luminosity	2.5%

TABLE 7.3

b tagging veto systematic uncertainty in each category

	0 jet	1 jet	2 jets gg-enriched	2 jets VBF-enriched
$t\bar{t}$	–	2.45%	4.37%	2.59%
t	–	2.11%	3.07%	1.98%

the ones affect the shape of M_{col} distribution. The uncertainties on the electron measurements, which include the trigger, ID and isolation are estimated with the tag and probe measurement with Z boson datasets [32, 70]. The uncertainties on the $Z \rightarrow \tau\tau$ process is mainly from the uncertainty on the cross section measurement [36] and the τ identification in the embedded technique. The normalization uncertainty on $Z \rightarrow ee$ amounts to 30% which is the from the measurement of cross section and statistics uncertainty in the yields. An extra 5% shape uncertainty is added due to the mismeasured energy of the electron reconstructed as τ in $Z \rightarrow ee$ background. The shift in M_{col} distribution is measured by the comparison between data and MC simulation. A 30% normalization uncertainty is applied to the misidentified lepton background. The extra shape uncertainties to this background are obtained by varying the parameters from fitting the misidentified ratio in ± 1 standard deviation. The uncertainty from the pileup process is estimated by varying the total inelastic cross section by $\pm 5\%$ [35]. The uncertainty from the Diboson, single top quark background is taken from the measurement of the cross section. In $t\bar{t}$ background, the uncertainty in 0 jet, 1 jet category are taken from the cross section measurement, in 2 jets category, an extra 33% uncertainty uncorrelated between categories is added due to the statistical uncertainty. The luminosity uncertainty amounts to 2.6%. The jet energy scale(JES) and resolution are measured with $\gamma/Z + jets$ and dijet samples [31]. The uncertainty from JES is applied as a function of p_T and η . The jet energy resolution(JER) uncertainty is obtained by smearing jets energy as a function of p_T and η . Both JES and JER affect the shape of M_{col} distribution and are taken as shape uncertainties. The energy of the jets below 10 GeV and PF objets that are not clustered are accounted as the unclustered energy scale, which is also taken as shape uncer-

tainties. The uncertainty of τ_h energy scale is obtained by comparing $Z \rightarrow \tau\tau$ distribution between data and MC samples and is applied as a shape uncertainty. The theoretical uncertainties considered in the $H \rightarrow e\tau_h$ analysis are listed in Table. 7.6. There are several sources that contribute to the theoretical uncertainties and are considered fully correlated between LFV Higgs and SM Higgs production. The uncertainty in Parton distribution function is obtained by counting the yields with different PDFs, CT10 [75], MSTW [74], NNPDF [19] from the recommendation in PDF4LHC [22]. The uncertainty in renormalization and factorization scales are from scaling up and down by a factor of two to their normal values($\mu_R = \mu_F = M_H/2$). The uncertainty in underlying events and parton shower is estimated by checking with different PYTHIA tunes. The theoretical uncertainties are all correlated or anticorrelated. The anticorrelated ones have a minus superscript and are the result of the event migration.

TABLE 7.4: The normalization systematic uncertainties considered in $H \rightarrow e\tau_h$ analysis. The uncertainties are correlated between categories besides the ones after \oplus . These uncertainties are uncorrelated between categories.

Systematic uncertainty	$H \rightarrow e\tau_h$		
	0-jet	1-jet	2-jet
Electron trigger/ID/isolation	1%	1%	2%
Efficiency of τ_h	6.7%	6.7%	6.7%
$Z \rightarrow \tau\tau$ background	3% \oplus 5%	3% \oplus 5%	3% \oplus 10%
$Z \rightarrow ee$ background	30%	30%	30%
Misidentified leptons background	30%	30%	30%
Pileup	4%	4%	2%
WW, WZ, ZZ+jets background	15%	15%	15%
$t\bar{t}$ background	10%	10%	10% \oplus 33%
Single top quark background	25%	25%	25%
Luminosity	2.6%	2.6%	2.6%

TABLE 7.5

The systematic uncertainties that affect the shape of M_{col} distribution.

Systematic Uncertainty	$H \rightarrow e\tau_h$
$Z \rightarrow ee$ bias	5%
Jet energy scale	3%–7%
Jet energy resolution	1%–10%
Unclustered energy scale	10%
τ_h energy scale	3%

TABLE 7.6: Theoretical uncertainties that affects the Higgs boson production cross section. These uncertainties are correlated or anticorrelated (with minus sign superscript) between all of the categories.

Systematic uncertainty	Gluon fusion			Vector boson fusion		
	0-jet	1-jet	2-jet	0-jet	1-jet	2-jet
Parton distribution function	9.7%	9.7%	9.7%	3.6%	3.6%	3.6%
Renormalization/factorization scale	8%	10%	30 ⁻ %	4%	1.5%	2%
Underlying event/parton shower	4%	5 ⁻ %	10 ⁻ %	10%	<1%	1 ⁻ %

CHAPTER 8

LFV Higgs decay search results

The results can be extracted after applying the selection criteria and with the full consideration of the relevant systematics. In both $H \rightarrow \mu\tau_h$ and $H \rightarrow e\tau_h$ analysis, a maximum likelihood fit is performed to derive the expected and observed limits. Each category in the analysis is fitted separately and then combined. Systematic uncertainties are used as nuisance parameter in the fittings. The upper limits on signal branching fraction with CL_s criterion are set with asymptotic formula.

8.0.1 Results in $H \rightarrow \mu\tau_h$ search

In the lepton flavour violation $H \rightarrow \mu\tau_h$ search at central of mass energy of 13 TeV, the analysis is performed in two parallel searching method, the M_{col} fit analysis and BDT fit analysis. After the selection in the M_{col} fit analysis and adjusting all of distribution by the fit, the distribution of the signal and background discriminant variable M_{col} is shown in Figure. 8.3. In the BDT fit analysis, the BDT discriminator is used as the variable to distinguish signal from background. After fitting to all of the distributions, the observed data versus the expected backgrounds is shown in Figure. 8.2. No excess over the backgrounds is observed in both of the methods. The expected and observed median upper limits at 95% CL and the best fit branching fraction in the $H \rightarrow \mu\tau_h$ search with the

M_{col} fit analysis is shown in Table. 8.1 and the result of the BDT fit analysis is shown in Table. 8.2.

The search in $H \rightarrow \mu\tau$ with CMS 13 TeV, 36 fb^{-1} data is motivated by the previous CMS search on the 8 TeV dataset with 19.7 fb^{-1} $H \rightarrow \mu\tau$, in which a significance of 2.4 standard deviation excess of data with respect to the SM background-only hypothesis was observed. This thesis describes the $H \rightarrow \mu\tau_h$ search, which combined together with another search for $H \rightarrow \mu\tau_e$ [43], where the tau lepton decays electronically to an electron, instead of tau hadronically decay, provides the most sensitive search for $H \rightarrow \mu\tau$. The combined result is shown with the BDT fit analysis and M_{col} fit analysis separately in Figure. 8.3. No evidence of excess is found in this combined result. Compared with the previous 8 TeV result, the new upper limits on the signal branching fraction improved a factor of 5. The BDT fit analysis is more sensitive than the the M_{col} fit analysis. The new and tighter limit result comes from the BDT fit analysis.

The constrains on flavour violating Yukawa couplings can be derived from the limits on branching fraction of LFV Higgs decay. The exact relationship between Yukawa couplings and branching fraction of LFV Higgs decays is shown in section. 2.2.1. The 125 GeV Standard Model Higgs decay width is taken as $\Gamma_{\text{SM}} = 4.1 \text{ MeV}$ [51]. In BDT fit analysis, the 95% CL upper limit on the Yukawa coupling is $\sqrt{|Y_{\mu\tau}|^2 + |Y_{\tau\mu}|^2} < 1.43 \times 10^{-3}$ and in M_{col} fit analysis, $\sqrt{|Y_{\mu\tau}|^2 + |Y_{\tau\mu}|^2} < 2.05 \times 10^{-3}$. The upper limit on Yukawa couplings of BDT fit analysis is shown in Figure. 8.4. The comparison with the previous experimental search and theoretical naturalness results is also shown in the plot.

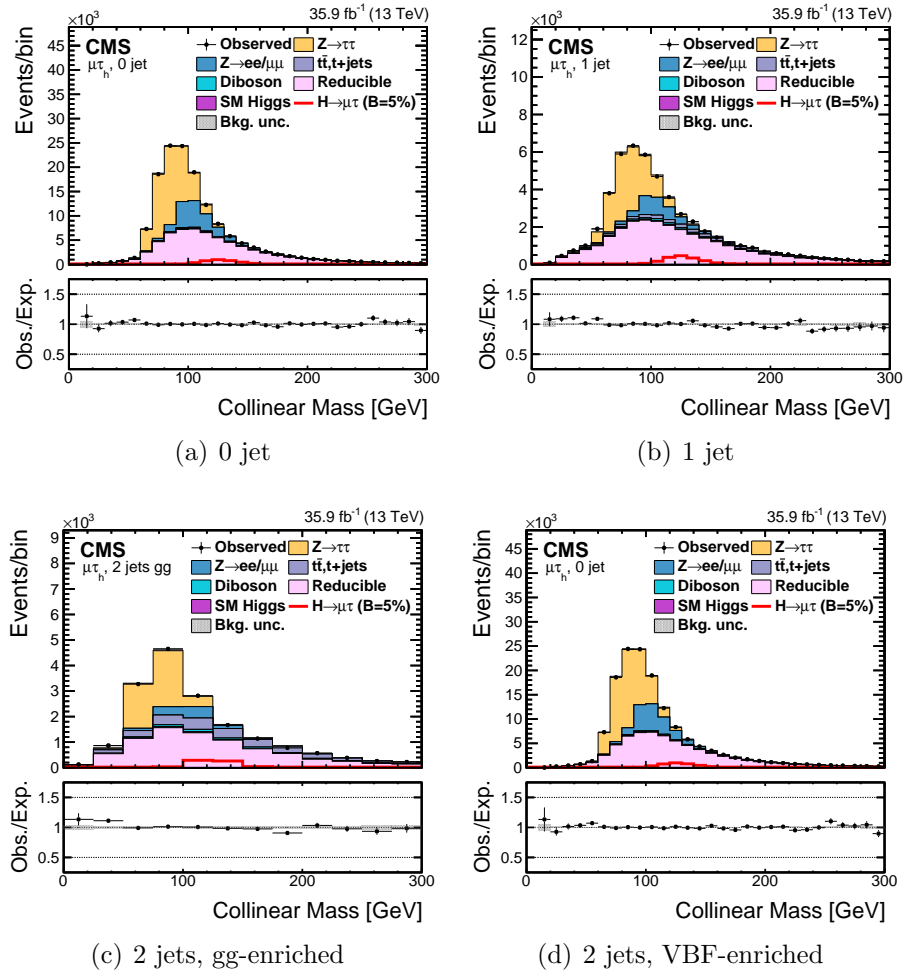


Figure 8.1. M_{col} distribution after the selection. The signal and backgrounds in the plots have been normalized to the best fit values. The gray bands shows the total uncertainties in each bin and the signal is plotted with the branching ratio of 5% of the Higgs decay branching ratio for visualization purpose.

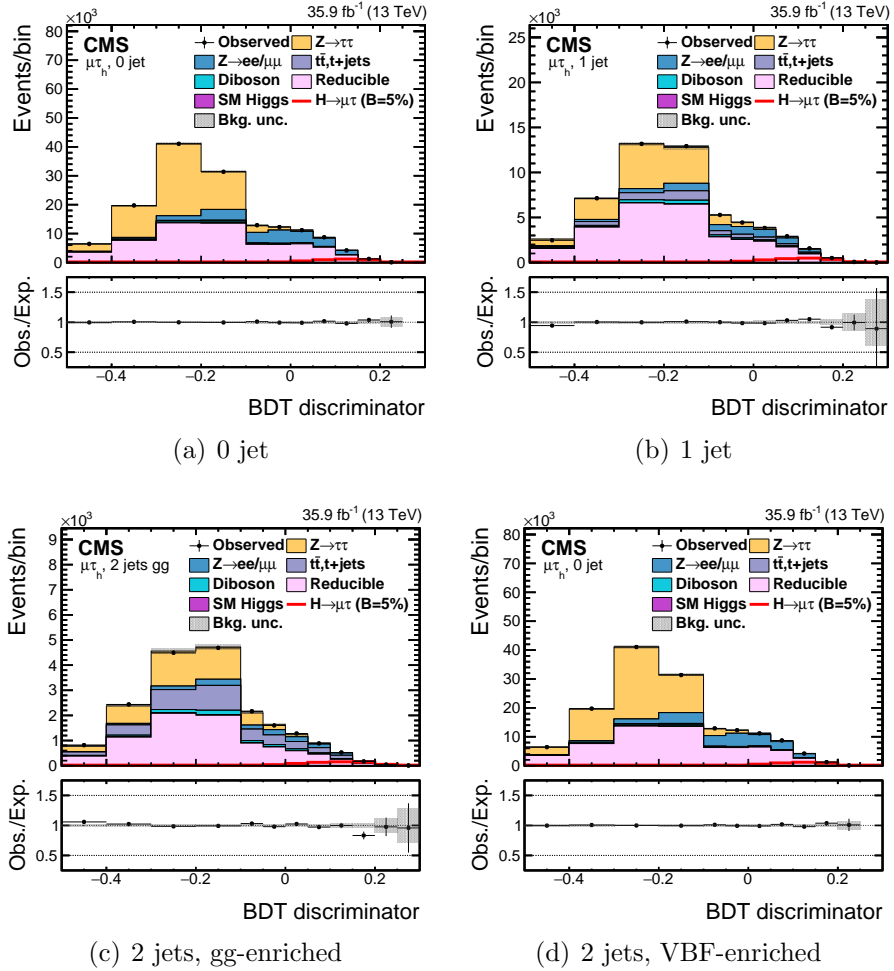


Figure 8.2. The BDT discriminator distribution after the selection. The signal and backgrounds in the plots has been normalized to the best fit values. The gray bands shows the total uncertainties in each bin and the signal is plotted with the branching ratio of 5% of the Higgs decay branching ratio for visualization purpose.

TABLE 8.1

M_{col} fit analysis expected and observed upper limits at 95% CL and the best fit branching fractions in each of the categories.

Expected limits (%)					
	0-jet	1-jet	2-jets	VBF	Combined
$\mu\tau_h$	< 1.14	< 1.26	< 2.12	< 1.41	< 0.71
Observed limits (%)					
	0-jet	1-jet	2-jets	VBF	Combined
$\mu\tau_h$	< 1.04	< 1.74	< 1.65	< 1.30	< 0.66
Best fit branching fractions (%)					
	0-jet	1-jet	2-jets	VBF	Combined
$\mu\tau_h$	-0.30 \pm 0.45	0.68 \pm 0.56	-1.23 \pm 1.04	-0.23 \pm 0.66	-0.08 \pm 0.34

TABLE 8.2

BDT fit analysis expected and observed upper limits at 95% CL and the best fit branching fractions in each of the categories.

Expected limits (%)					
	0-jet	1-jet	2-jets	VBF	Combined
$\mu\tau_h$	<0.43	<0.56	<0.94	<0.58	<0.29
Observed limits (%)					
	0-jet	1-jet	2-jets	VBF	Combined
$\mu\tau_h$	<0.51	<0.53	<0.56	<0.51	<0.27
Best fit branching fractions (%)					
	0-jet	1-jet	2-jets	VBF	Combined
$\mu\tau_h$	0.12 ± 0.20	-0.05 ± 0.25	-0.72 ± 0.43	-0.22 ± 0.31	-0.04 ± 0.14

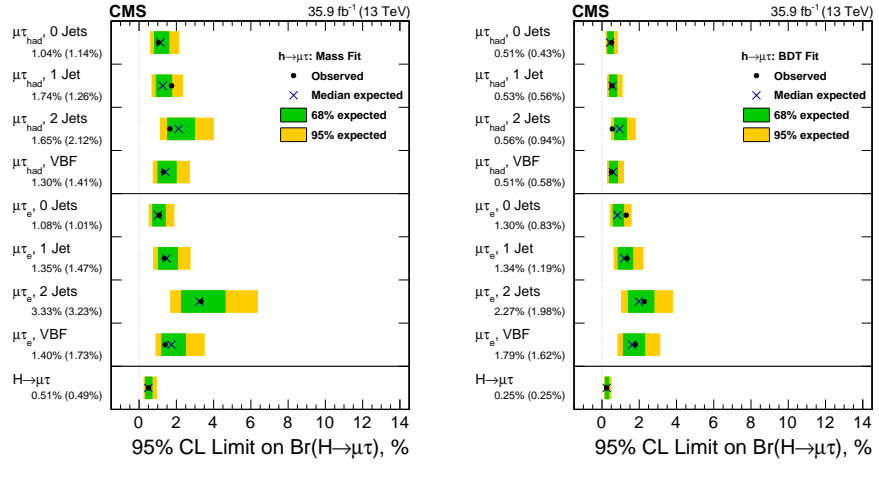


Figure 8.3. The expected and observed 95% CL limits on branching ratio of total $H \rightarrow \mu\tau$ which shows the results from both $H \rightarrow \mu\tau_h$ and $H \rightarrow \mu\tau_e$ in the M_{col} fit analysis and BDT fit analysis.

8.0.2 Results in $H \rightarrow e\tau_h$ search

The search of $H \rightarrow e\tau_h$ is performed in M_{col} fit analysis with CMS 8 TeV 19.7 fb^{-1} . The analysis is binned with 3 categories. After applying the selection cuts and adjusting the signal and background processes by the fit, the fitting variable M_{col} distribution is shown in Figure. 8.5. The number of event yields of both signal and background processes are shown in Table. 8.3. The yields are normalized to the integrated luminosity of 19.7 fb^{-1} and the signal branching ratio is assumed to be 0.69% of the SM Higgs production cross section. This thesis is focused and written on the analysis $H \rightarrow e\tau_h$ which is one part of the whole search on lepton flavour violating Higgs decay to $e\tau$. Another closely related search is $H \rightarrow e\tau_\mu$ [6]. The results of each categories and combined ones of the two analysis $H \rightarrow e\tau_h$ and $H \rightarrow e\tau_\mu$ on the expected and observed upper signal branching fraction $\mathcal{B}(H \rightarrow e\tau)$

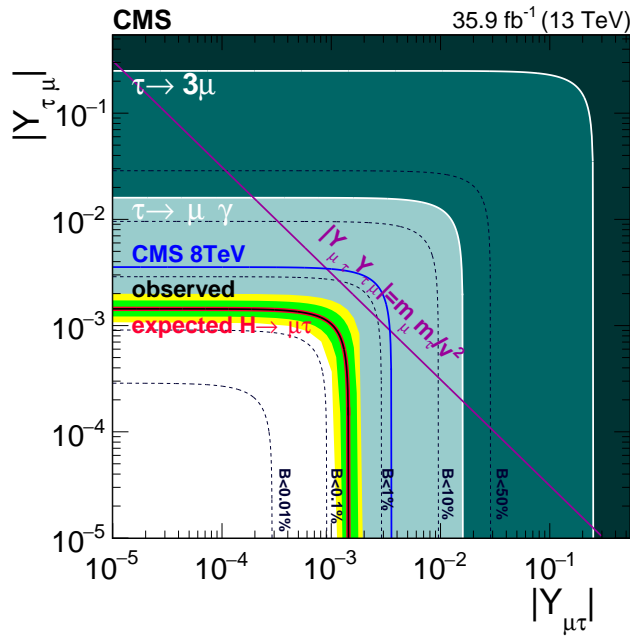


Figure 8.4. Upper limit of flavour violating Yukawa coupling $|Y_{\mu\tau}|, |Y_{\tau\mu}|$ from the BDT fit analysis. The red solid line represents the expected limit and the black solid line is the observed limit. 68% and 95% range of containing the observed limit is shown in the green and yellow band. The result from $\tau \rightarrow 3\mu$ is shown in dark green [64, 65, 78] and the one from $\tau \rightarrow \mu\gamma$ is shown in lighter green [64, 78]. The theoretical naturalness limit $Y_{ij}Y_{ji} \leq m_i m_j / v^2$ is shown by purple diagonal line [64].

limits is shown in Table. 8.4 and summarized in Figure. 8.6. The combined upper limit on $\mathcal{B}(H \rightarrow e\tau) < 0.69$ is the first direct search on this channel and the tightest limit by the time the result was published. The Yukawa coupling between electron and tau leptons is related to decay width Γ and branching fraction \mathcal{B} as shown in Equation. 2.18 and 2.19. The 95% CL upper limit on Yukawa coupling from the combined result in $H \rightarrow e\tau$ is $\sqrt{|Y_{e\tau}|^2 + |Y_{\tau e}|^2} < 2.4 \times 10^{-3}$. The limit on $e\tau$ Yukawa coupling from this search and other previous search results are shown in Figure. 8.0.2.

TABLE 8.3: Events yields of the signal and backgrounds are shown in the mass range $100 \text{ GeV} < M_{col} < 150 \text{ GeV}$. The branching ratio of $H \rightarrow e\tau_h$ is assumed to be 0.69% of the SM Higgs production cross section. The numbers in the table are normalized to the integrated luminosity of 19.7 fb^{-1} .

Jet category:	0-jet	1-jet	2-jet
Misidentified leptons	3366 ± 25	223 ± 11	8.7 ± 2.2
$Z \rightarrow ee, \mu\mu$	714 ± 30	85 ± 4	3.2 ± 0.2
$Z \rightarrow \tau\tau$	270 ± 10	32 ± 3	1.6 ± 0.3
$t\bar{t}, t, \bar{t}$	10 ± 2	13 ± 2	0.5 ± 0.2
ZZ, WZ, WW	53 ± 2	6 ± 1	0.3 ± 0.1
SM H background	12 ± 1	3 ± 1	1.0 ± 0.1
Sum of background	4425 ± 28	363 ± 11	15.3 ± 2.3
Observed	4438	375	13
LFV H signal	61 ± 4	15 ± 1	2.8 ± 0.5

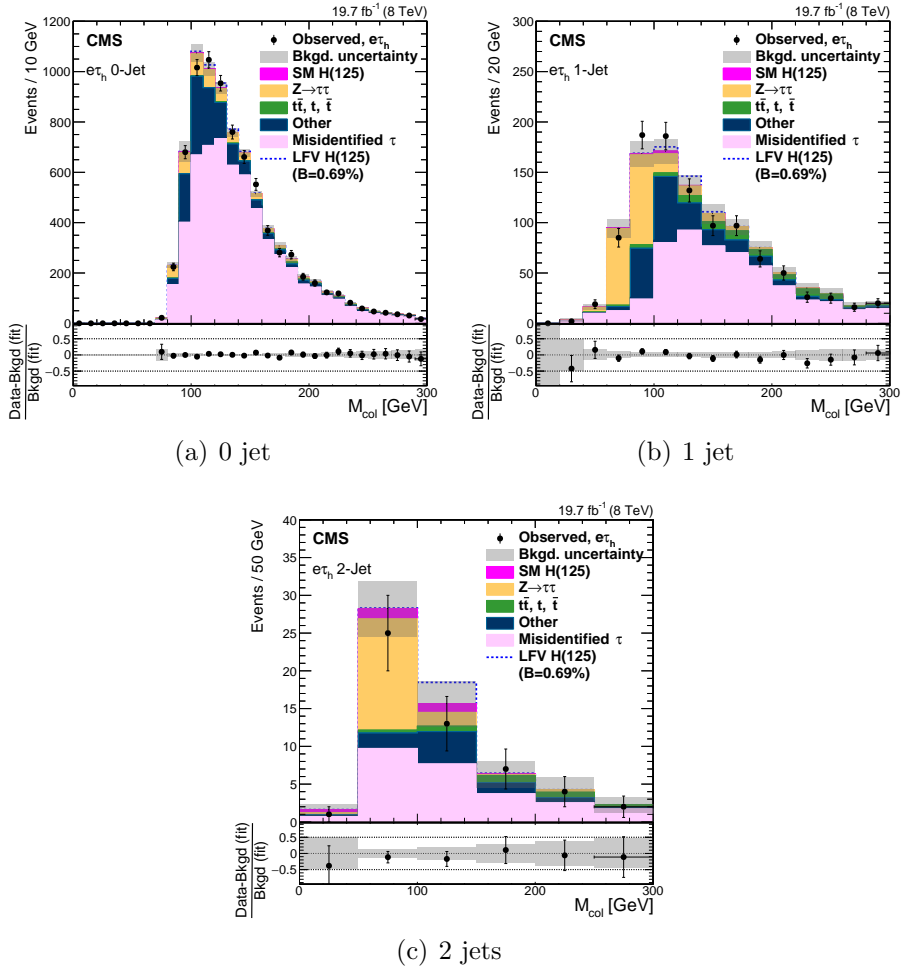


Figure 8.5. M_{col} distribution after the selection. The signal and backgrounds in the plots have been normalized to the best fit values. The gray bands shows the total uncertainties in each bin and the signal is plotted with the branching ratio of 0.69% of the Higgs decay branching ratio for visualization purpose.

TABLE 8.4

M_{col} fit analysis expected and observed upper limits at 95% CL and the best fit branching fractions in each of the categories of both $H \rightarrow e\tau_h$ and $H \rightarrow e\tau_\mu$ analyses. The asymmetric one standard-deviation uncertainties around the expected limits are shown in parentheses.

	0-jet	1-jet	2-jet
Expected limits at 95% CL (%)			
$e\tau_\mu$	$<1.63^{(+0.66)}_{(-0.44)}$	$<1.54^{(+0.71)}_{(-0.47)}$	$<1.59^{(+0.93)}_{(-0.55)}$
$e\tau_h$	$<2.71^{(+1.05)}_{(-0.75)}$	$<2.76^{(+1.07)}_{(-0.77)}$	$<3.55^{(+1.38)}_{(-0.99)}$
Observed limits at 95% CL (%)			
$e\tau_\mu$	<1.83	<0.94	<1.49
$e\tau_h$	<3.92	<3.00	<2.88
$e\tau$	<0.69		

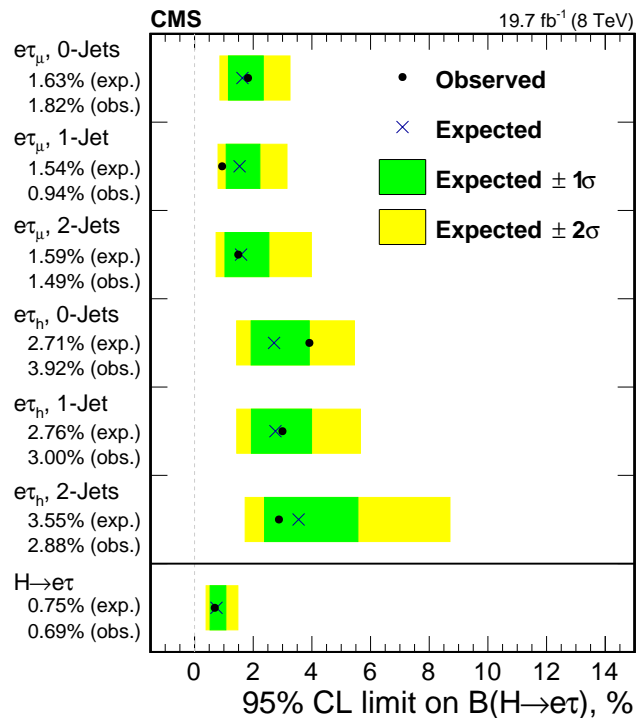


Figure 8.6. 95% CL upper limit on branching ratio on $H \rightarrow e\tau$ with both the results from $H \rightarrow e\tau_h$ and $H \rightarrow e\tau_\mu$ and the combined.

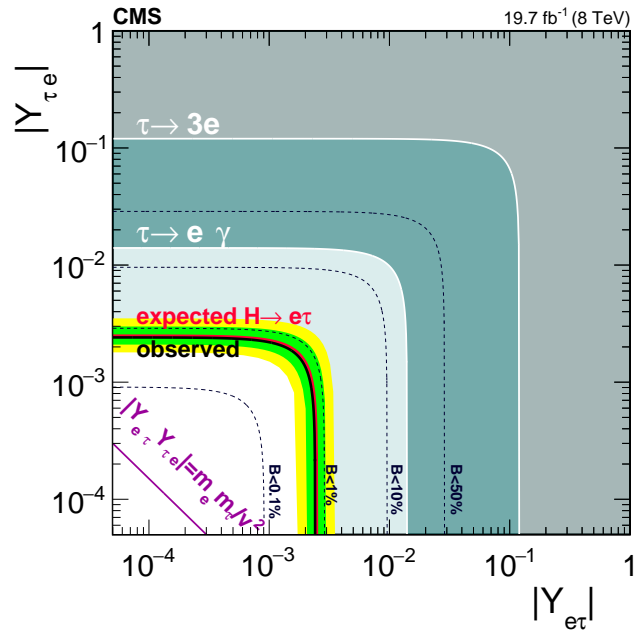


Figure 8.7. Upper limit of flavour violating Yukawa coupling $|Y_{e\tau}|, |Y_{\tau e}|$ from the combined $H \rightarrow e\tau$ result. The red solid line represents the expected limit and the black solid line is the observed limit. 68% and 95% range of containing the observed limit is shown in the green and yellow band. The result from $\tau \rightarrow 3e$ is shown in gray, the one from $\tau \rightarrow e\gamma$ is shown in dark green and presented analysis is in light blue. The theoretical naturalness limit $Y_{ij}Y_{ji} \leq m_i m_j / v^2$ is shown by purple diagonal line [64]

CHAPTER 9

Conclusion

The operation of LHC opens a new era for experimental particle physics searches with colliders. The great performance of the general purpose detector CMS provides the possibilities to fully explore new physics. Throughout this dissertation, the theory background for the search of lepton flavour violation Higgs decay, an introduction of LHC and CMS, the detailed information about the data sets used, the reconstruction methods for the events in CMS and the search in two channels of LFV Higgs decays are presented. The focus is the physics search.

The searches are performed on the standard model Higgs lepton flavour violation decay on the LHC with CMS detector. One search is on $H \rightarrow e\tau_h$ with an integrated luminosity of 19.7 fb^{-1} at center-of-mass energy 8 TeV dataset and another search is on $H \rightarrow \mu\tau_h$ with 35.9 fb^{-1} at 13 TeV. The results from both of the searches are presented, also the final results which combined with search for tau leptons decay electronically with respect to the tau hadronic decay ones. The $H \rightarrow e\tau$ search gave the upper limit from the direct measurement for the first time. The combined limit on the branching fraction in $H \rightarrow e\tau$ is $B < 0.69$ at 95% CL and on Yukawa coupling as $Y_{e\tau} < 2.4 \times 10^{-3}$. The search on $H \rightarrow \mu\tau_h$ with 35.9 fb^{-1} at 13 TeV is also presented. Even though the excess observed in 8 TeV search in $H \rightarrow \mu\tau$ channel is gone, the combined result from 13 TeV search is the most stringent limit so far. In $H \rightarrow \mu\tau_h$, a combined limit with the $H \rightarrow \mu\tau_e$

channel on the branching ratio of $H \rightarrow \mu\tau$ is $B < 0.25\%$ and the upper limit on Yukawa coupling is $Y_{\mu\tau} < 1.43 \times 10^{-3}$.

The latest search for 125 GeV Higgs LFV decay $H \rightarrow \mu\tau$ is presented in the dissertation. While for the $H \rightarrow e\tau$ search, the 13 TeV results published together with $H \rightarrow \mu\tau$ search here [44]. Though no significant excesses are observed in both $\mu\tau$ and $e\tau$ channel, compared with the $H \rightarrow e\mu$ channel, there is a large parameter space to explore in this topic. Whether or not LFV is observed, this is an important topic which has big influences on new physics searches.

BIBLIOGRAPHY

1. LHC Higgs cross section working group. URL <https://twiki.cern.ch/twiki/bin/view/LHCPhysics/LHCHXSWG>.
2. Particle-flow commissioning with muons and electrons from J/Psi and W events at 7 TeV. Technical Report CMS-PAS-PFT-10-003, CERN, Geneva, 2010. URL <http://cds.cern.ch/record/1279347>.
3. Procedure for the LHC Higgs boson search combination in Summer 2011. Technical Report CMS-NOTE-2011-005. ATL-PHYS-PUB-2011-11, CERN, Geneva, Aug 2011. URL <https://cds.cern.ch/record/1379837>.
4. Pileup Jet Identification. Technical Report CMS-PAS-JME-13-005, CERN, Geneva, 2013. URL <http://cds.cern.ch/record/1581583>.
5. Search for lepton-flavour-violating decays of the higgs boson. *Physics Letters B*, 749:337 – 362, 2015. ISSN 0370-2693. doi: <https://doi.org/10.1016/j.physletb.2015.07.053>. URL <http://www.sciencedirect.com/science/article/pii/S0370269315005638>.
6. Search for lepton flavour violating decays of the higgs boson to $e\tau$ and $e\mu$ in proton-proton collisions at $\sqrt{s} = 8$ TeV. *Phys. Lett. B*, 763:472, 2016. doi: [10.1016/j.physletb.2016.09.062](https://doi.org/10.1016/j.physletb.2016.09.062).

7. CMS luminosity measurements for the 2016 data taking period. CMS Physics Analysis Summary CMS-PAS-LUM-17-001, 2017. URL <https://cds.cern.ch/record/2257069>.
8. 06 2018. URL https://en.wikipedia.org/wiki/Standard_Model.
9. G. Aad et al. Search for lepton-flavour-violating H^- decays of the Higgs boson with the ATLAS detector. *JHEP*, 11:211, 2015. doi: 10.1007/JHEP11(2015)211.
10. D. Acosta. Cms trigger improvements towards run ii. *Nuclear and Particle Physics Proceedings*, 273-275:1008 – 1013, 2016. ISSN 2405-6014. doi: <https://doi.org/10.1016/j.nuclphysbps.2015.09.158>. URL <http://www.sciencedirect.com/science/article/pii/S2405601415006471>. 37th International Conference on High Energy Physics (ICHEP).
11. W. Adam, R. Frühwirth, A. Strandlie, and T. Todor. Reconstruction of Electrons with the Gaussian-Sum Filter in the CMS Tracker at the LHC. 2005.
12. W. Adam, B. Mangano, T. Speer, and T. Todorov. Track Reconstruction in the CMS tracker. Technical Report CMS-NOTE-2006-041, CERN, Geneva, Dec 2006. URL <https://cds.cern.ch/record/934067>.
13. P. Adzic et al. Energy resolution of the barrel of the CMS electromagnetic calorimeter. *JINST*, 2:P04004, 2007. doi: 10.1088/1748-0221/2/04/P04004.
14. J. Alwall, R. Frederix, S. Frixione, V. Hirschi, F. Maltoni, O. Mattelaer, H.-S. Shao, T. Stelzer, P. Torrielli, and M. Zaro. The automated computation of tree-level and next-to-leading order differential cross sections, and their

- matching to parton shower simulations. *JHEP*, 07:079, 2014. doi: 10.1007/JHEP07(2014)079.
15. C. Anastasiou, R. Boughezal, and F. Petriello. Mixed QCD-electroweak corrections to Higgs boson production in gluon fusion. *JHEP*, 04:003, 2009. doi: 10.1088/1126-6708/2009/04/003.
 16. D. Aristizabal Sierra and A. Vicente. Explaining the cms higgs flavor-violating decay excess. *Phys. Rev. D*, 90:115004, Dec 2014. doi: 10.1103/PhysRevD.90.115004. URL <https://link.aps.org/doi/10.1103/PhysRevD.90.115004>.
 17. M. Baber, M. Blake, J. Brooke, M. C. Hermida, S. Dasu, T. Durkin, S. Fayer, E. K. Friis, T. Gorski, G. Hall, K. Harder, G. Iles, S. Ives, J. Jones, P. R. Klabbers, A. G. Levine, C. Lucas, R. Lucas, D. Newbold, J. Marrouche, S. Paramesvaran, T. M. Perry, A. Rose, D. Sankey, W. Smith, A. Tapper, A. Thea, and T. Williams. Development and testing of an upgrade to the cms level-1 calorimeter trigger. *Journal of Instrumentation*, 9(01):C01006, 2014. URL <http://stacks.iop.org/1748-0221/9/i=01/a=C01006>.
 18. A. M. Baldini et al. Search for the lepton flavour violating decay $\mu^+ \rightarrow e^+ \gamma$ with the full dataset of the MEG experiment. *Eur. Phys. J. C*, 76:434, 2016. doi: 10.1140/epjc/s10052-016-4271-x.
 19. R. D. Ball, L. Del Debbio, S. Forte, A. Guffanti, J. I. Latorre, J. Rojo, and M. Ubiali. A first unbiased global NLO determination of parton distributions and their uncertainties. *Nucl. Phys. B*, 838:136, 2010. doi: 10.1016/j.nuclphysb.2010.05.008.
 20. G. Blankenburg, J. Ellis, and G. Isidori. Flavour-changing decays of a 125

- GeV Higgs-like particle. *Phys. Lett. B*, 712:386, 2012. doi: 10.1016/j.physletb. 2012.05.007.
21. P. Bolzoni, F. Maltoni, S.-O. Moch, and M. Zaro. Higgs production via vector-boson fusion at NNLO in QCD. *Phys. Rev. Lett.*, 105:011801, 2010. doi: 10.1103/PhysRevLett.105.011801.
 22. M. Botje, J. Butterworth, A. Cooper-Sarkar, A. de Roeck, J. Feltesse, S. Forte, A. Glazov, J. Huston, R. McNulty, T. Sjöstrand, and R. S. Thorne. The PDF4LHC Working Group Interim Recommendations. 2011.
 23. G. Branco, P. Ferreira, L. Lavoura, M. Rebelo, M. Sher, and J. P. Silva. Theory and phenomenology of two-higgs-doublet models. *Physics Reports*, 516(1):1 – 102, 2012. ISSN 0370-1573. doi: <https://doi.org/10.1016/j.physrep.2012.02.002>. URL <http://www.sciencedirect.com/science/article/pii/S0370157312000695>. Theory and phenomenology of two-Higgs-doublet models.
 24. M. Cacciari, G. P. Salam, and G. Soyez. The anti- k_t jet clustering algorithm. *JHEP*, 04:063, 2008. doi: 10.1088/1126-6708/2008/04/063.
 25. M. Cacciari, G. P. Salam, and G. Soyez. FastJet user manual. *Eur. Phys. J. C*, 72:1896, 2012. doi: 10.1140/epjc/s10052-012-1896-2.
 26. R. N. Cahn, S. D. Ellis, R. Kleiss, and W. J. Stirling. Transverse-momentum signatures for heavy Higgs bosons. *Phys. Rev. D*, 35:1626, 1987. doi: 10.1103/PhysRevD.35.1626.
 27. S. Catani, D. de Florian, M. Grazzini, and P. Nason. Soft gluon resummation

- for Higgs boson production at hadron colliders. *JHEP*, 07:028, 2003. doi: 10.1088/1126-6708/2003/07/028.
28. A. Celis, V. Cirigliano, and E. Passemar. Lepton flavor violation in the Higgs sector and the role of hadronic tau-lepton decays. *Phys. Rev. D*, 89:013008, 2014. doi: 10.1103/PhysRevD.89.013008.
29. S. Chatrchyan et al. The CMS Experiment at the CERN LHC. *JINST*, 3:S08004, 2008. doi: 10.1088/1748-0221/3/08/S08004.
30. S. Chatrchyan et al. Aligning the CMS Muon Chambers with the Muon Alignment System during an Extended Cosmic Ray Run. *JINST*, 5:T03019, 2010. doi: 10.1088/1748-0221/5/03/T03019.
31. S. Chatrchyan et al. Determination of jet energy calibration and transverse momentum resolution in CMS. *JINST*, 6:11002, 2011. doi: 10.1088/1748-0221/6/11/P11002.
32. S. Chatrchyan et al. Measurement of the inclusive W and Z production cross sections in pp collisions at $\sqrt{s} = 7$ TeV with the CMS experiment. *JHEP*, 10:132, 2011. doi: 10.1007/JHEP10(2011)132.
33. S. Chatrchyan et al. Performance of CMS muon reconstruction in pp collision events at $\sqrt{s} = 7$ TeV. *JINST*, 7:P10002, 2012. doi: 10.1088/1748-0221/7/10/P10002.
34. S. Chatrchyan et al. Performance of CMS muon reconstruction in *pp* collision events at $\sqrt{s} = 7$ TeV. *JINST*, 7:P10002, 2012. doi: 10.1088/1748-0221/7/10/P10002.

35. S. Chatrchyan et al. Measurement of the inelastic proton-proton cross section at $\sqrt{s} = 7\text{TeV}$. *Phys. Lett. B*, 722:5, 2013. doi: 10.1016/j.physletb.2013.03.024.
36. S. Chatrchyan et al. Measurement of inclusive W and Z boson production cross sections in pp collisions at $\sqrt{s} = 8$ TeV. *Phys. Rev. Lett.*, 112:191802, 2014. doi: 10.1103/PhysRevLett.112.191802.
37. S. Chatrchyan et al. Evidence for the 125 GeV Higgs boson decaying to a pair of τ leptons. 2014.
38. C. Collaboration". Performance of τ -lepton reconstruction and identification in CMS. *JINST*, 7(arXiv:1109.6034. CMS-TAU-11-001. CERN-PH-EP-2011-137):P01001. 33 p, Sep 2011. URL <http://cds.cern.ch/record/1385560>.
39. C. Collaboration. Performance of reconstruction and identification of tau leptons in their decays to hadrons and tau neutrino in LHC Run-2. CMS Physics Analysis Summary CMS-PAS-TAU-16-002, 2016. URL <https://cds.cern.ch/record/2196972>.
40. C. Collaboration. Performance of reconstruction and identification of tau leptons in their decays to hadrons and tau neutrino in LHC Run-2. 2016.
41. C. Collaboration. Reconstruction and identification of tau lepton decays to hadrons and tau neutrino at CMS. *JINST 11 (2016) P01019*, 11, 2016. doi: 10.1088/1748-0221/11/01/P01019.
42. C. Collaboration. Identification of b quark jets at the CMS Experiment in the LHC Run 2. Technical Report CMS-PAS-BTV-15-001, CERN, Geneva, 2016. URL <https://cds.cern.ch/record/2138504>.

43. C. Collaboration. Search for lepton flavour violating decays of the Higgs boson to τ and e in proton-proton collisions at $\sqrt{s}= 13$ TeV. *JHEP*, 2017.
44. C. collaboration. Search for lepton flavour violating decays of the higgs boson to $\mu\tau$ and $e\tau$ in proton-proton collisions at $\sqrt{s}=13$ tev. *Journal of High Energy Physics*, 2018(6):1, Jun 2018. ISSN 1029-8479. doi: 10.1007/JHEP06(2018)001. URL [https://doi.org/10.1007/JHEP06\(2018\)001](https://doi.org/10.1007/JHEP06(2018)001).
45. G. Collaboration. Geant4—a simulation toolkit. *Nuclear Instruments and Methods in Physics Research Section A: Accelerators, Spectrometers, Detectors and Associated Equipment*, 506(3):250 – 303, 2003. ISSN 0168-9002. doi: [https://doi.org/10.1016/S0168-9002\(03\)01368-8](https://doi.org/10.1016/S0168-9002(03)01368-8). URL <http://www.sciencedirect.com/science/article/pii/S0168900203013688>.
46. K. Cranmer. Practical Statistics for the LHC. *CERN-2014-003*, pp. 267 - 308, 2015. doi: 10.5170/CERN-2015-004.301.
47. S. Dasu et al. CMS. The TriDAS project. Technical design report, vol. 1: The trigger systems. 2000.
48. D. de Florian, C. Grojean, F. Maltoni, C. Mariotti, A. Nikitenko, M. Pieri, P. Savard, M. Schumacher, R. Tanaka, R. Aggleton, M. Ahmad, B. Allanach, C. Anastasiou, W. Astill, S. Badger, M. Badziak, J. Baglio, E. Bagnaschi, A. Ballestrero, A. Banfi, D. Barducci, M. Beckingham, C. Becot, G. Blanger, J. Bellm, N. Belyaev, F. Bernlochner, C. Beskidt, A. Biektter, F. Bishara, W. Bizon, N. Bomark, M. Bonvini, S. Borowka, V. Bortolotto, S. Boselli, F. Botella, R. Boughezal, G. Branco, J. Brehmer, L. Brenner, S. Bressler, I. Brivio, A. Broggio, H. Brun, G. Buchalla, C. Burgard,

A. Calandri, L. Caminada, R. Caminal Armadans, F. Campanario, J. Campbell, F. Caola, C. Carloni Calame, S. Carrazza, A. Carvalho, M. Casolino, O. Cata, A. Celis, F. Cerutti, N. Chanon, M. Chen, X. Chen, B. Chokouf Nejad, N. Christensen, M. Ciuchini, R. Contino, T. Corbett, R. Costa, D. Curtin, M. Dall'Osso, A. David, S. Dawson, J. de Blas, W. de Boer, P. de Castro Manzano, C. Degrande, R. Delgado, F. Demartin, A. Denner, B. Di Micco, R. Di Nardo, S. Dittmaier, A. Dobado, T. Dorigo, F. Dreyer, M. Dhrssen, C. Duhr, F. Dulat, K. Ecker, K. Ellis, U. Ellwanger, C. Englert, D. Espriu, A. Falkowski, L. Fayard, R. Feger, G. Ferrera, A. Ferroglio, N. Fidanza, T. Figy, M. Flechl, D. Fontes, S. Forte, P. Francavilla, E. Franco, R. Frederix, A. Freitas, F. Freitas, F. Frensch, S. Frixione, B. Fuks, E. Furlan, S. Gadatsch, J. Gao, Y. Gao, M. Garzelli, T. Gehrmann, R. Gerosa, M. Ghezzi, D. Ghosh, S. Gieseke, D. Gillberg, G. Giudice, E. Glover, F. Goertz, D. Goncalves, J. Gonzalez-Fraile, M. Gorbahn, S. Gori, C. Gottardo, M. Gouzevitch, P. Govoni, D. Gray, M. Grazzini, N. Greiner, A. Greljo, J. Grigo, A. Gritsan, R. Grber, S. Guindon, H. Haber, C. Han, T. Han, R. Harlander, M. Harrendorf, H. Hartanto, C. Hays, S. Heinemeyer, G. Heinrich, M. Herrero, F. Herzog, B. Hespel, V. Hirschi, S. Hoeche, S. Honeywell, S. Huber, C. Hugonie, J. Huston, A. Ilnicka, G. Isidori, B. Jger, M. Jaquier, S. Jones, A. Juste, S. Kallweit, A. Kaluza, A. Kardos, A. Karlberg, Z. Kassabov, N. Kauer, D. Kazakov, M. Kerner, W. Kilian, F. Kling, K. Kneke, R. Kogler, R. Konoplich, S. Kortner, S. Kräml, C. Krause, F. Krauss, M. Krawczyk, A. Kulesza, S. Kuttmalai, R. Lane, A. Lazopoulos, G. Lee, P. Lenzi, I. Lewis, Y. Li, S. Liebler, J. Lindert, X. Liu, Z. Liu, F. Llanes-Estrada, H. Logan, D. Lopez-Val, I. Low, G. Luisoni, P. Maierhfer, E. Maina,

B. Mansouli, H. Mantler, M. Mantoani, A. Marini, V. Martinez Outschoorn, S. Marzani, D. Marzocca, A. Massironi, K. Mawatari, J. Mazzitelli, A. McCarn, B. Mellado, K. Melnikov, S. Menari, L. Merlo, C. Meyer, P. Milenovic, K. Mimasu, S. Mishima, B. Mistlberger, S.-O. Moch, A. Mohammadi, P. Monni, G. Montagna, M. Moreno Llcer, N. Moretti, S. Moretti, L. Motyka, A. Mck, M. Mhlleitner, S. Munir, P. Musella, P. Nadolsky, D. Napoletano, M. Nebot, C. Neu, M. Neubert, R. Nevzorov, O. Nicrosini, J. Nielsen, K. Nikolopoulos, J. No, C. O'Brien, T. Ohl, C. Oleari, T. Orimoto, D. Pagani, C. Pandini, A. Papaefstathiou, A. Papanastasiou, G. Passarino, B. Pecjak, M. Pelliccioni, G. Perez, L. Perrozzi, F. Petriello, G. Petrucciani, E. Pianori, F. Piccinini, M. Pierini, A. Pilkington, S. Pltzer, T. Plehn, R. Podskubka, C. Potter, S. Pozzorini, K. Prokofiev, A. Pukhov, I. Puljak, M. Queitsch-Maitland, J. Quevillon, D. Rathlev, M. Rauch, E. Re, M. Rebelo, D. Rebuzzi, L. Reina, C. Reuschle, J. Reuter, M. Riembau, F. Riva, A. Rizzi, T. Robens, R. Rntsch, J. Rojo, J. Romo, N. Rompotis, J. Roskes, R. Roth, G. Salam, R. Salerno, M. Sampaio, R. Santos, V. Sanz, J. Sanz-Cillero, H. Sargsyan, U. Sarica, P. Schichtel, J. Schlenk, T. Schmidt, C. Schmitt, M. Schnherr, U. Schubert, M. Schulze, S. Sekula, M. Sekulla, E. Shabalina, H. Shao, J. Shelton, C. Shepherd-Themistocleous, S. Shim, F. Siegert, A. Signer, J. Silva, L. Silvestrini, M. Sjodahl, P. Slavich, M. Slawinska, L. Soffi, M. Spannowsky, C. Speckner, D. Sperka, M. Spira, O. Stl, F. Staub, T. Stebel, T. Stefaniak, M. Steinhauser, I. Stewart, M. Strassler, J. Streicher, D. Strom, S. Su, X. Sun, F. Tackmann, K. Tackmann, A. Teixeira, R. Teixeira de Lima, V. Theeuwes, R. Thorne, D. Tommasini, P. Torrielli, M. Tosi, F. Tramontano, Z. Trcsnyi, M. Trott, I. Tsinkos, M. Ubiali, P. Vanlaer, W. Verkerke, A. Vicini, L. Viliani,

- E. Vryonidou, D. Wackerlo, C. Wagner, J. Wang, S. Wayand, G. Weiglein, C. Weiss, M. Wiesemann, C. Williams, J. Winter, D. Winterbottom, R. Wolf, M. Xiao, L. Yang, R. Yohay, S. Yuen, G. Zanderighi, M. Zaro, D. Zeppenfeld, R. Ziegler, T. Zirke, and J. Zupan. Handbook of LHC Higgs Cross Sections: 4. Deciphering the Nature of the Higgs Sector. Technical Report FERMILAB-FN-1025-T, Oct 2016. URL <https://cds.cern.ch/record/2227475>. 869 pages, 295 figures, 248 tables and 1645 citations. Working Group web page: <https://twiki.cern.ch/twiki/bin/view/LHCPhysics/LHCHXSWG>.
49. D. de Florian et al. Handbook of LHC Higgs cross sections: 4. deciphering the nature of the Higgs sector. CERN Report CERN-2017-002-M, 2016.
 50. L. de Lima, C. S. Machado, R. D. Matheus, and L. A. F. do Prado. Higgs flavor violation as a signal to discriminate models. *Journal of High Energy Physics*, 2015(11):74, Nov 2015.
 51. A. Denner, S. Heinemeyer, I. Puljak, D. Rebuzzi, and M. Spira. Standard model Higgs-boson branching ratios with uncertainties. *Eur. Phys. J. C*, 71:1753, 2011. doi: 10.1140/epjc/s10052-011-1753-8.
 52. J. L. Diaz-Cruz and J. J. Toscano. Lepton flavor violating decays of higgs bosons beyond the standard model. *Phys. Rev. D*, 62:116005, Nov 2000. doi: 10.1103/PhysRevD.62.116005. URL <https://link.aps.org/doi/10.1103/PhysRevD.62.116005>.
 53. S. Dittmaier, C. Mariotti, G. Passarino, R. Tanaka, J. Baglio, P. Bolzoni, R. Boughezal, O. Brein, C. Collins-Tooth, S. Dawson, S. Dean, A. Denner, S. Farrington, M. Felcini, M. Flechl, D. de Florian, S. Forte, M. Grazzini,

- C. Hackstein, T. Hahn, R. Harlander, T. Hartonen, S. Heinemeyer, J. Huston, A. Kalinowski, M. Krmer, F. Krauss, J. S. Lee, S. Lehti, F. Maltoni, K. Mazumdar, S. O. Moch, A. Mck, M. Mhlleitner, P. Nason, C. Neu, C. Oleari, J. Olsen, S. Palmer, F. Petriello, G. Piacquadio, A. Pilaftsis, C. T. Potter, I. Puljak, J. Qian, D. Rebuzzi, L. Reina, H. Rzechak, M. Schumacher, P. Slavich, M. Spira, F. Stckli, R. S. Thorne, M. V. Acosta, T. Vickey, A. Vicini, D. Wackeroth, M. Warsinsky, M. Weber, G. Weiglein, C. Weydert, J. Yu, M. Zaro, and T. Zirke. *Handbook of LHC Higgs Cross Sections: 1. Inclusive Observables*. CERN Yellow Reports: Monographs. CERN, Geneva, 2011. URL <https://cds.cern.ch/record/1318996>. Comments: 153 pages, 43 figures, to be submitted to CERN Report. Working Group web page: <https://twiki.cern.ch/twiki/bin/view/LHCPysics/CrossSections>.
54. S. Dittmaier, C. Mariotti, G. Passarino, R. Tanaka, S. Alekhin, J. Alwall, E. A. Bagnaschi, A. Banfi, J. Blumlein, S. Bolognesi, N. Chanon, T. Cheng, L. Cieri, A. M. Cooper-Sarkar, M. Cutajar, S. Dawson, G. Davies, N. De Filippis, G. Degrassi, A. Denner, D. D'Enterria, S. Diglio, B. Di Micco, R. Di Nardo, R. K. Ellis, A. Farilla, S. Farrington, M. Felcini, G. Ferrera, M. Flechl, D. de Florian, S. Forte, S. Ganjour, M. V. Garzelli, S. Gascon-Shotkin, S. Glazov, S. Goria, M. Grazzini, J. P. Guillet, C. Hackstein, K. Hamilton, R. Harlander, M. Hauru, S. Heinemeyer, S. Hoche, J. Huston, C. Jackson, P. Jimenez-Delgado, M. D. Jorgensen, M. Kado, S. Kallweit, A. Kardos, N. Kauer, H. Kim, M. Kovac, M. Kramer, F. Krauss, C. M. Kuo, S. Lehti, Q. Li, N. Lorenzo, F. Maltoni, B. Mellado, S. O. Moch, A. Muck, M. Muhlleitner, P. Nadolsky, P. Nason, C. Neu, A. Nikitenko, C. Oleari, J. Olsen, S. Palmer, S. Paganis, C. G. Papadopoulos, T. C.

- Petersen, F. Petriello, F. Petrucci, G. Piacquadio, E. Pilon, C. T. Potter, J. Price, I. Puljak, W. Quayle, V. Radescu, D. Rebuzzi, L. Reina, J. Rojo, D. Rosco, G. P. Salam, A. Sapronov, J. Schaarschmidt, M. Schonherr, M. Schumacher, F. Siegert, P. Slavich, M. Spira, I. W. Stewart, W. J. Stirling, F. Stockli, C. Sturm, F. J. Tackmann, R. S. Thorne, D. Tommasini, P. Torrielli, F. Tramontano, Z. Trocsanyi, M. Ubiali, S. Uccirati, M. V. Acosta, T. Vickey, A. Vicini, W. J. Waalewijn, D. Wackeroth, M. Warsinsky, M. Weber, M. Wiesemann, G. Weiglein, J. Yu, and G. Zanderighi. Handbook of LHC Higgs Cross Sections: 2. Differential Distributions. Technical Report arXiv:1201.3084. CERN-2012-002, Geneva, 2012. URL <https://cds.cern.ch/record/1416519>. Comments: 275 pages, 136 figures, to be submitted to CERN Report. Working Group web page: <https://twiki.cern.ch/twiki/bin/view/LHCPhysics/CrossSections>.
55. A. Djouadi. The anatomy of electroweak symmetry breaking: Tome i: The higgs boson in the standard model. *Physics Reports*, 457(1):1 – 216, 2008. ISSN 0370-1573. doi: <https://doi.org/10.1016/j.physrep.2007.10.004>. URL <http://www.sciencedirect.com/science/article/pii/S0370157307004334>.
56. A. Djouadi, M. Spira, and P. M. Zerwas. Production of Higgs bosons in proton colliders: QCD corrections. *Phys. Lett.*, B264:440–446, 1991. doi: 10.1016/0370-2693(91)90375-Z.
57. S. D. Ellis and D. E. Soper. Successive combination jet algorithm for hadron collisions. *Phys. Rev.*, D48:3160–3166, 1993. doi: 10.1103/PhysRevD.48.3160.

58. L. Evans and P. Bryant. Lhc machine. *Journal of Instrumentation*, 3(08):S08001, 2008. URL <http://stacks.iop.org/1748-0221/3/i=08/a=S08001>.
59. R. Fruhwirth. Application of Kalman filtering to track and vertex fitting. *Nucl. Instrum. Meth.*, A262:444–450, 1987. doi: 10.1016/0168-9002(87)90887-4.
60. H. M. Georgi, S. L. Glashow, M. E. Machacek, and D. V. Nanopoulos. Higgs bosons from two gluon annihilation in proton proton collisions. *Phys. Rev. Lett.*, 40:692, 1978. doi: 10.1103/PhysRevLett.40.692.
61. V. Gori. The CMS High Level Trigger. *Int. J. Mod. Phys. Conf. Ser.*, 31:1460297, 2014. doi: 10.1142/S201019451460297X.
62. D. J. Griffiths. *Introduction to elementary particles; 2nd rev. version*. Physics textbook. Wiley, New York, NY, 2008. URL <https://cds.cern.ch/record/111880>.
63. R. Harnik, J. Kopp, and J. Zupan. Flavor violating higgs decays. *JHEP*, 03:26, 2013. doi: 10.1007/JHEP03(2013)026.
64. R. Harnik, J. Kopp, and J. Zupan. Flavor violating higgs decays. *JHEP*, 03:26, 2013. doi: 10.1007/JHEP03(2013)026.
65. K. Hayasaka et al. Search for lepton flavor violating τ decays into three leptons with 719 million produced $\tau^+\tau^-$ pairs. *Phys. Lett. B*, 687:139, 2010. doi: 10.1016/j.physletb.2010.03.037.
66. A. Hoecker, P. Speckmayer, J. Stelzer, J. Therhaag, E. von Toerne, H. Voss, M. Backes, T. Carli, O. Cohen, A. Christov, D. Dannheim, K. Danielowski, S. Henrot-Versille, M. Jachowski, K. Kraszewski, A. Krasznahorkay, Jr.,

- M. Kruk, Y. Mahalalel, R. Ospanov, X. Prudent, A. Robert, D. Schouten, F. Tegenfeldt, A. Voigt, K. Voss, M. Wolter, and A. Zemla. TMVA - Toolkit for Multivariate Data Analysis. *ArXiv Physics e-prints*, Mar. 2007.
67. V. Khachatryan et al. Measurements of inclusive W and Z cross sections in pp collisions at $\sqrt{s} = 7$ TeV. *J. High Energy Phys.*, 01:080, 2011. doi: 10.1007/JHEP01(2011)080.
 68. V. Khachatryan et al. Performance of electron reconstruction and selection with the CMS detector in proton-proton collisions at $\sqrt{s} = 8$ TeV. *JINST*, 10:P06005, 2015. doi: 10.1088/1748-0221/10/06/P06005.
 69. V. Khachatryan et al. Performance of electron reconstruction and selection with the CMS detector in proton-proton collisions at $\sqrt{s} = 8$ TeV. *JINST*, 10:P06005, 2015. doi: 10.1088/1748-0221/10/06/P06005.
 70. V. Khachatryan et al. Reconstruction and identification of tau lepton decays to hadrons and ν_τ at CMS. *JINST*, 11:P01019, 2016. doi: 10.1088/1748-0221/11/01/P01019.
 71. V. Khachatryan et al. Jet energy scale and resolution in the CMS experiment in pp collisions at 8 TeV. *JINST*, 12:P02014, 2017. doi: 10.1088/1748-0221/12/02/P02014.
 72. C. Lefèvre. The CERN accelerator complex. Complexe des accélérateurs du CERN. Dec 2008. URL <https://cds.cern.ch/record/1260465>.
 73. L. Lista. Practical Statistics for Particle Physicists. 2016.

74. A. D. Martin, W. J. Stirling, R. S. Thorne, and G. Watt. Parton distributions for the LHC. *Eur. Phys. J. C*, 63:189, 2009. doi: 10.1140/epjc/s10052-009-1072-5.
75. P. M. Nadolsky, H.-L. Lai, Q.-H. Cao, J. Huston, J. Pumplin, D. Stump, W.-K. Tung, and C.-P. Yuan. Implications of CTEQ global analysis for collider observables. *Phys. Rev. D*, 78:013004, 2008. doi: 10.1103/PhysRevD.78.013004.
76. G. N. Davidson et al. Universal interface of tauola technical and physics documentation. doi: 10.1016/j.cpc.2011.12.009.
77. C. Olari. The POWHEG-BOX. *Nucl.Phys.Proc.Suppl.205-206:36-41,2010*, 2010. doi: 10.1016/j.nuclphysbps.2010.08.016.
78. Particle Data Group, C. Patrignani, et al. Review of Particle Physics. *Chin. Phys. C*, 40:100001, 2016. doi: 10.1088/1674-1137/40/10/100001.
79. M. E. Peskin and D. V. Schroeder. *An Introduction to quantum field theory*. Addison-Wesley, Reading, USA, 1995. ISBN 9780201503975, 0201503972. URL <http://www.slac.stanford.edu/~mpeskin/QFT.html>.
80. B. P. Roe et al. Boosted Decision Trees as an Alternative to Artificial Neural Networks for Particle Identification. 2005.
81. D. Rabady, J. Ero, G. Flouris, J. Fulcher, N. Loukas, E. Paradas, T. Reis, H. Sakulin, and C.-E. Wulz. Upgrade of the CMS muon trigger system in the barrel region. *Nucl. Instrum. Meth.*, A845:616–620, 2017. doi: 10.1016/j.nima.2016.05.071.

82. A. M. Sirunyan et al. Particle-flow reconstruction and global event description with the cms detector. *JINST*, 12:P10003, 2017. doi: 10.1088/1748-0221/12/10/P10003.
83. A. M. Sirunyan et al. Particle-flow reconstruction and global event description with the cms detector. *JINST*, 12:P10003, 2017. doi: 10.1088/1748-0221/12/10/P10003.
84. A. M. Sirunyan et al. Identification of heavy-flavour jets with the CMS detector in pp collisions at 13 TeV. *JINST*, 13:P05011, 2018. doi: 10.1088/1748-0221/13/05/P05011.
85. T. Sjöstrand, S. Ask, J. R. Christiansen, R. Corke, N. Desai, P. Ilten, S. Mrenna, S. Prestel, C. O. Rasmussen, and P. Z. Skands. An introduction to PYTHIA 8.2. *Comput. Phys. Commun.*, 191:159, 2015. doi: 10.1016/j.cpc.2015.01.024.
86. E. Yazgan and the CMS ECAL/HCAL Collaborations. The cms barrel calorimeter response to particle beams from 2 to 350 gev/c. *Journal of Physics: Conference Series*, 160(1):012056, 2009. URL <http://stacks.iop.org/1742-6596/160/i=1/a=012056>.
87. S. Yu.L.Dokshitzer, G.D.Leder and B.R.Webber. Better Jet Clustering Algorithms. *JHEP* 9708:001, 1997, 1997. doi: 10.1088/1126-6708/1997/08/001.
88. A. Zabi, F. Beaudette, L. Cadamuro, L. Mastrolorenzo, T. Romanteau, J. Sauvan, T. Strebler, J. Marrouche, N. Wardle, R. Aggleton, F. Ball, J. Brooke, D. Newbold, S. Paramesvaran, D. Smith, M. Baber, A. Bundred, M. Citron, A. Elwood, G. Hall, G. Iles, C. Laner, B. Penning, A. Rose, A. Tap-

per, T. Durkin, K. Harder, S. Harper, C. Shepherd-Themistocleous, A. Thea, and T. Williams. Triggering on electrons, jets and tau leptons with the cms upgraded calorimeter trigger for the lhc run ii. *Journal of Instrumentation*, 11(02):C02008, 2016. URL <http://stacks.iop.org/1748-0221/11/i=02/a=C02008>.

This document was prepared & typeset with pdfL^AT_EX, and formatted with NDDiss2_E classfile (v3.0[2005/07/27]) provided by Sameer Vijay.